Electron-induced reaction dynamics studied by velocity-map and covariance-map imaging



Alexander Butler

Exeter College

A thesis submitted for the DPhil in Physical Chemistry

2025

Acknowledgements

Firstly, Prof. Claire Vallance has been an inspirational supervisor. Always forthcoming with sage advice to surmount scientific challenges or offering exciting ideas for new projects to pursue, this DPhil would not have been possible without her guidance.

There are many others who have made working in the Vallance Group such a pleasure. Although by no means exhaustive, I would like to mention several individuals in particular. David and Patrick were excellent sources of wisdom and were always willing to discuss science. David's ability to solve any coding difficulty and Patrick's formidable knowledge of the latest developments in the field were invaluable.

I will always remember the Vallance Group lunches fondly. In particular, Annabel and David were constant lunch companions throughout. Our constitutional lunchtime walks in Summer, during which conversation spanned any topic under the (hopefully bright) sun, were a particular highlight. After work, Dennis could always be relied upon to go for a run; perhaps my knee will always bear the scar from trying to climb over a builder's fence after we took a wrong turning down a closed footpath.

The Part II students with whom I have worked over course of my DPhil deserve a great deal of thanks. Megan, Daria, Olivia and Eugenie were all a pleasure to work with and made the moments when the experiment wasn't working as we thought it should easier to bear. It was always far better to have two brains and sets of hands working on any problem.

Beyond the Vallance Group, the workshops in the department were essential to the research presented in this thesis. In particular, I would like to thank Pete and Johan from the mechanical workshop, and Phil, John and Tim from the electronics workshop. Whether it be mending a breakage, or designing and building a new contraption, they were always willing to help.

Finally, I would like to put on record my profound gratitude to my parents, Shelly and Tony. They have been right behind me, not just throughout my DPhil, but for the entirety of my education. Without their unwavering support, none of this would have been possible.

Summary

Electron ionisation is a fundamental physical process that is relevant in many natural and industrial settings, from the interstellar medium to plasma etching. After a molecule has been ionised by an electron, it may dissociate; this thesis investigates the dissociative electron ionisation of a variety of molecules of different complexity at a range of electron energies. Throughout, time-of-flight mass spectrometry and velocity-map imaging are used to identify dissociation pathways and characterise the associated dissociation dynamics.

Since electron ionisation is not governed by optical selection rules, it is often difficult to determine which electronic state a nascent ion is formed in. By restricting the electron energy to values close to a molecule's ionisation threshold, changes in dissociation dynamics can be correlated with the population of specific electronic states of the parent cation. This approach was adopted to study the dissociative electron ionisation of trifluoroiodomethane (CF_3I), methyl fluoride (CH_3F) and methyl chloride (CH_3Cl). All three compounds exhibit distinct dissociation dynamics, depending on the initial electronic state of the parent cation. Notably, anisotropic ion scattering distributions were observed for CH_3^+ formation from both CH_3F and CH_3Cl, demonstrating that the probability of ionising these molecules depends on their orientation relative to the incoming electron.

In order to enable the study of larger, non-volatile compounds, a laser-induced desorption source was implemented and optimised for use on the electron–molecule crossed beam apparatus. As a result of this development, the dissociative electron

ionisation of the polycyclic aromatic hydrocarbon triphenylene could be investigated. This work revealed a fragmentation pathway for triphenylene dications involving initial dissociation yielding two daughter ions, followed by sequential loss of neutral acetylene units, resembling the reverse of the hydrogen abstraction–acetylene addition mechanism proposed for PAH growth in the interstellar medium.

Contents

List of Figures **ix**

List of Tables **xiii**

List of Abbreviations **xiv**

1 Introduction **1**
- 1.1 Electron-Molecule Collisions . . . 3
  - 1.1.1 Electron ionisation . . . 4
  - 1.1.2 Electron ionisation cross-section . . . 6
- 1.2 Potential energy surfaces . . . 8
- 1.3 Scattering distributions . . . 11
- 1.4 Velocity-map imaging . . . 14
- 1.5 Molecular sample preparation . . . 16
  - 1.5.1 Gaseous samples . . . 16
  - 1.5.2 Solid samples . . . 18
- 1.6 Outline of this thesis . . . 20

2 Experimental Methods **21**
- 2.1 Molecular beam . . . 22
- 2.2 Laser-induced desorption source . . . 24
- 2.3 Electron gun . . . 27
- 2.4 Ion Optics . . . 31
- 2.5 Detector and Camera . . . 34
- 2.6 Summary . . . 35

3 Data processing and analysis **36**
- 3.1 Centroiding . . . 36
- 3.2 Time-of-Flight spectra and ion images . . . 38
- 3.3 Image Inversion . . . 41
  - 3.3.1 Basis function fitting methods . . . 44
- 3.4 Energy Calibration . . . 46
- 3.5 Covariance analysis . . . 47

3.5.1 Recoil-frame covariance 50
3.5.2 Partial and contingent covariance 54
3.6 Summary 55

4 Electron ionisation of trifluoroiodomethane at low electron energies 56
4.1 Data processing and image denoising 59
4.2 Computational methods 63
4.3 Time-of-flight mass spectra 66
4.4 Velocity-Map Images 70
4.4.1 Carbon-iodine bond breaking 72
4.4.2 Carbon-fluorine bond dissociation 78
4.5 Summary 80

5 Electron ionisation of methyl fluoride and methyl chloride at low electron energies 81
5.1 Mass Spectra 84
5.2 Velocity-Map Images 87
5.2.1 CH_3F dissociation: product kinetic energy distributions . . . 88
5.2.2 CH_3Cl dissociation: product kinetic energy distributions . . 94
5.3 Dependence on molecular orientation 97
5.4 Summary 102

6 Characterisation of a laser-induced desorption source 104
6.1 Introduction 104
6.2 Effect of sample thickness on ion signals 105
6.3 Generation of intact molecules in the gas phase 108
6.4 Optimising velocity-mapping conditions 109
6.5 Summary 112

7 Dissociative electron ionisation of triphenylene 114
7.1 Introduction 114
7.2 Methods 115
7.3 Mass spectra 116
7.4 Velocity-map images 121
7.5 Recoil-frame covariance analysis 124
7.6 Summary 133

8 Conclusion and outlook **135**
8.1 Conclusion 135
8.2 Outlook 138
8.2.1 New electron source 138
8.2.2 Measuring the kinetic energy of outgoing electrons 139
8.2.3 Orienting molecules in the molecular beam 140

Bibliography **142**

Appendices

A Appendix: Electron ionisation of trifluoroiodomethane at low electron energies **152**

B Appendix: Electron ionisation of methyl fluoride and methyl chloride at low electron energies **155**

List of Figures

1.1 Exemplar potential energy surfaces for the diatomic molecule A-B. . 9
1.2 Product scattering distributions of the molecule A-B. 11
1.3 Diagram of ion lens assemblies 15
1.4 Schematic of the shock regions formed around the nozzle of a supersonic molecular beam source. 18

2.1 Schematic of the electron-molecule crossed beam experiment. 21
2.2 Schematic diagram of a pulsed solenoid valve 23
2.3 Schematic diagram of the laser-induced desorption (LID) source. . . 25
2.4 Schematic diagram of the LID source diode laser beamline. 26
2.5 Plot showing diode laser power immediately after the diode laser and at the LID source tip as a function of diode current. 26
2.6 Schematic diagram of the electron source installed on the electron-molecule crossed beam experiment. 27
2.7 Spatial profile of the electron beam at 20 eV, obtained from the spatial-map image of background H_2O^+. 28
2.8 Schematic diagram of the electron beam kinetic energy detection assembly. 29
2.9 Electron beam kinetic energy distribution measurement. 30
2.10 Diagram of the ion lens in the electron-molecule crossed beam apparatus. 32
2.11 Ion image of the CH_3F^+ parent ion recorded under velocity-mapping conditions. 33
2.12 Schematic of a position-sensitive ion detector consisting of MCPs and a scintillator screen. 34

3.1 Schematic diagram showing how an ion hit is processed by the centroiding algorithm. 37
3.2 Schematic diagrams of (a) a 3D scattering distribution with an axis of cylindrical symmetry, (b) its 2D projection, and (c) the central slice of the 3D distribution. 41
3.3 A vector diagram for electron-molecule collisions. 42

3.4 (a) A simulated 2D velocity-map image and its corresponding radial distribution. (b) The inverted image with its corresponding radial distribution. 45
3.5 Time-of-flight covariance map for the fragment ions produced by the electron ionisation of CF_3I at 100 eV. 49
3.6 An illustration of the process to calculate a recoil-frame covariance for the signal ion X^+ and reference ion Y^+. 51
3.7 Simulated velocity-map and recoil-frame covariance-map images for (a) a two-body and (b) a three-body dissociation. 53

4.1 Partial correlation diagram for the dissociation of different electronic states of CF_3I^+. 58
4.2 Schematic of the process used to generate a set of images to train an artificial neural network (ANN) to denoise velocity-map images. . . 61
4.3 Demonstration of an autoencoder artificial neural network denoising a velocity-map image. 62
4.4 Schematic diagram of the active space used to calculate PESs for CF_3I^+. 65
4.5 Potential energy curves along the carbon-iodine coordinate in CF_3I^+ 67
4.6 Background-subtracted time-of-flight mass spectra of CF_3I. 68
4.7 Partial cross-sections for the formation of CF_3I^+ fragment ions. . . 69
4.8 Symmetrised velocity-map images, Abel-inverted images and TKER distributions for the $CF_3{}^+$ fragment from the dissociative ionisation of CF_3I. 71
4.9 Symmetrised velocity-map images, Abel-inverted images and TKER distributions for the I^+ fragment from the dissociative ionisation of CF_3I. 74
4.10 Symmetrised and inverted velocity-map images and corresponding TKER distributions for the CF_2I^+ fragment from the dissociative ionisation of CF_3I. 79

5.1 Background-subtracted mass spectra of (a) CH_3F and (b) CH_3Cl at electron energies of 15 eV and 20 eV. 83
5.2 Partial ionisation cross-sections of the fragments produced by the electron ionisation of CF_3I, plotted as a function of electron energy. 87
5.3 Potential energy curves for the low-lying electronic states of (a) CH_3F^+ along the C-F bond and (b) CH_3Cl^+ along the C-Cl bond. . 88
5.4 Velocity-map images of $CH_3{}^+$ produced from CH_3F at electron energies of 15, 17, 20 and 500 eV, with associated TKER distributions. 89

5.5 Velocity-map images of CH_2^+ produced from CH_3F at electron energies of 16, 20, 25 and 500 eV, with corresponding TKER distributions. 93
5.6 Velocity-map images for CH_3^+ produced from CH_3Cl at 14, 16, 18 and 100 eV, with corresponding TKER distributions. 95
5.7 The β_1 anisotropy parameter of the CH_3^+ scattering distribution, plotted as a function of TKER for (a) CH_3F and (b) CH_3Cl at an electron energy of 20 eV. 98
5.8 The radial distribution and corresponding values for the $beta_1$ anisotropy parameter of CH_3^+ produced from CH_3Cl, plotted as a function of distance travelled perpendicular to the molecular beam axis in the experimental configuration of Aitken *et al.* 100
5.9 The highest-lying C-F sigma bonding orbital in CH_3F. 101

6.1 Parent ion signal plotted as a function of aqcuisition time for three sample thicknesses. 107
6.2 Ratio of the intensities of the most abundant fragment ion and parent ion of triphenylene at different diode laser powers. 109
6.3 Sample desorption from the LID source tip with and without a barrier between the source and scattering chambers. 110
6.4 Schematic demonstrating the effect of varying the distance between the LID source foil and repeller plate on the size of the electron-molecule interaction region. 111
6.5 Triphenylene$^+$ velocity-map images at four foil-repeller plate distances 112

7.1 Structure of triphenylene. 115
7.2 Triphenylene mass spectra at various electron energies. 118
7.3 Branching ratios for selected product ions of triphenylene, plotted at electron energy. 119
7.4 Mechanism for acetylene loss from phenanthrene, as proposed by West *et al.*[161] 120
7.5 Velocity-map images and corresponding kinetic energy distributions for fragment ions of triphenylene at 100 eV. 122
7.6 Matrix of recoil-frame covariance maps for all possible combinations of signal and reference ions following the electron ionisation of triphenylene at 100 eV. 125
7.7 The final projected momenta of different product ion pairs, plotted as a function of the initial separation between the two point charges. 128
7.8 Recoil-frame and native-frame covariance maps for a series of signal ions correlated with reference ion C_4^+. 131

A.1 The mean denoised radial distributions for the (a) CF_3^+, (b) I^+ and (c) CF_2I^+ products, with 2σ error bands. 153
A.2 The sum of squared residuals associated with fitting I^+ TKER distributions. 154

B.1 Spatial map images for (a) CH_2^+ and (b) CHF^+ produced from CH_3F. 156
B.2 Spatial map image for H^+ produced from CH_3Cl. 156

List of Tables

1.1 Inelastic electron-molecule scattering processes. 3

4.1 CF_3I fragment ion appearance potentials. 70
4.2 Fitting parameters obtained from the TKER distributions of the I^+ produced from CF_3I. 75
4.3 The mean TKER obtained for the CF_2I^+ ion produced from CF_3I. . 79

5.1 The mass peaks arising from the electron ionisation of CH_3F and CH_3Cl. 82
5.2 Parameters obtained from fitting TKER distributions of CH_3^+ produced from CH_3F. 91
5.3 Parameters obtained from fitting TKER distributions of CH_3^+ produced from CH_3Cl. 96
5.4 Mean β_1 values of CH_3^+ velocity-map images for CH_3F and CH_3Cl. 102

6.1 Details of samples characterised for use on the LID source. 106

7.1 Parameters obtained from fitting the projected momentum distributions of various two-body recoil-frame covariance maps with Gaussian functions. 127
7.2 Parameters obtained from fitting the projected velocity distributions of two-body recoil-frame covariance maps in which C_4^+ is the reference ion. 130

A.1 Vertical ionisation energies of the seven lowest electronic states of the CF_3I^+ cation. 154

List of Abbreviations

2D, 3D	Two- or three- dimensional
BASEX	Basis set expansion
CASPT2	Complete active space second-order perturbation theory
CASSCF	Complete active space self-consistent field
CW	Continuous wave
DNA	Deoxyribonucleic acid
EOM-IP-CCSD	Equation-of-motion coupled cluster with singles and doubles for ionization potentials
FWHM	Full width at half maximum
HACA	Hydrogen abstraction C_2H_2 addition
ISM	Interstellar medium
LID	Laser-induced desorption
MCP	Microchannel plate
m/z	Mass-to-charge ratio
PAH	Polycyclic aromatic hydrocarbon
PES	Potential energy surface
PImMS	Pixel Imaging Mass Spectrometry
SMI	Spatial-map imaging
TEM	Trochoidal electron monochromator
TKER	Total kinetic energy release
TNI	Transient negative ion
ToF	Time-of-flight
UV	Ultraviolet
VMI	Velocity-map imaging
XMS-CASPT2	Extended multi-state complete active space second-order perturbation theory
XUV	Extreme ultraviolet

1 Introduction

Electron–molecule collisions are fundamental processes that underpin a wide range of phenomena across the physical sciences. Plasmas, ionised gases composed of free electrons, ions and neutral molecules, are present in environments such as the Earth's atmosphere and the interstellar medium, and have applications in a range of industrial processes. In this environment, collisions between electrons and molecules are ubiquitous.

Electrons originating from the solar wind can become trapped by the Earth's magnetic field in the Van Allen radiation belts. Very low frequency (VLF) radiation (0.3-30 kHz), often generated by lightning, can scatter these electrons into the atmosphere, where they ionise neutral molecules in a process known as electron precipitation.[1–3] Solar photons in the extreme ultraviolet (EUV) range (with wavelengths less than 100 nm) can also ionise species such as N_2, O_2, N and O, producing photoelectrons with kinetic energies between 0 and 100 eV.[4] These electrons may then initiate dissociation, excitation, or further ionisation of neutral molecules.

Further afield, electron-molecule interactions play a key role in the interstellar medium. High-energy cosmic radiation can penetrate deep into interstellar clouds,

ionising matter and generating cascades of secondary electrons.[5,6] For instance, it is thought that a single high-energy cosmic ray is able to release 10^4 electrons when it collides with an ice covered dust grain. These secondary electrons may then induce chemical reactions on the surface of dust grains, including the synthesis of important prebiotic precursor molecules.[6]

Electron-molecule interactions also have important biological consequences. Secondary photoelectrons, produced when UV photons irradiate biological matter, cause damage to large biomolecules. Low-energy electrons (with energies below 15 eV) may attach to biomolecules, causing fragmentation,[7,8] whilst higher-energy electrons (up to 100 eV) can cause ionisation, dissociation and structural change.[9] Therefore, understanding how electrons interact with biologically relevant molecules is essential for a complete understanding of how ionising radiation affects living organisms.

When mass spectrometry, one of the cornerstone techniques of analytical chemistry, was first introduced by Dempster,[10] electron impact was used as the ionization method. Electron beams, typically with energies around 70 eV, are still widely used in mass spectrometry to this day, due to their ability to universally ionise sample molecules and generate reproducible spectra.[11]

Industrially, fluorocarbon-containing plasmas are commonly used to etch silicon dioxide during the manufacture of integrated circuits.[12] Electron-molecule collisions play a vital role in generating ions and radicals that serve as the reactive species that etch the surface.[13,14] An important benefit of plasma etching is that it is able to modify the surface of microelectronics without subjecting it to the damaging effects of high temperatures.

The various mechanisms by which electrons can interact with molecules, and how molecules react as a consequence, will now be discussed in more detail.

1.1 Electron-Molecule Collisions

Scattering events between electrons and molecules can be divided into two categories: elastic and inelastic scattering. In elastic scattering, the electron's trajectory is altered but its kinetic energy remains unchanged. In contrast, kinetic energy is transferred between the electron and molecule in inelastic scattering. The following discussion focusses on inelastic scattering processes, since these can change a molecule's state and initiate a chemical process.

The main inelastic scattering processes are summarised in Table 1.1 and discussed in turn.

Process	Mechanism
Excitation	$AB + e^- \longrightarrow AB^* + e^-$
Dissociative excitation	$AB + e^- \longrightarrow AB^* + e^- \longrightarrow A + B + e^-$
Ion pair formation	$AB + e^- \longrightarrow A^+ + B^- + e^-$
Electron attachment	$AB + e^- \longrightarrow AB^-$
Dissociative electron attachment	$AB + e^- \longrightarrow A + B^-$
Electron ionisation	$AB + e^- \longrightarrow AB^{n+} + (n+1)e^-$
Dissociative electron ionisation	$AB + e^- \longrightarrow A^+ + B + 2e^-$

Table 1.1: Inelastic electron-molecule scattering processes.

A molecule experiences a Coulomb potential as an incoming electron approaches,[15] which may be sufficient to promote the molecule to an excited rotational,[16] vibrational[17] and/or electronic[18] state. The excited molecule may break apart as a consequence[19,20] to form two neutral fragments. Alternatively, the excited molecule can dissociate into a positive ion and a negative ion.[21] For example, HCl can dissociate into H^+ and Cl^- following electron impact. However, the cross-section for this process has been found to be very small compared to the cross-section for ionisation at an electron energy of 15.5 eV.[22]

Low-energy electrons, with energies between 0 eV and 20 eV, can attach to a molecule to form a transient negative ion (TNI).[23,24] Typically, the TNI has a

lifetime between 10^{-14} s and 10^{-12} s. Possible decay pathways include decomposition into fragments (dissociative electron attachment), or loss of the extra electron (autodetachment). It is possible for thermal electrons, with energies close to 0 eV, to attach to form metastable parent anions with significantly longer lifetimes. This requires any excess energy to be dissipated upon attachment, for example by redistribution among the vibrational modes of the nascent anion.[25]

1.1.1 Electron ionisation

Electron ionisation occurs when an incoming electron with kinetic energy greater than the molecule's ionisation threshold collides with and ejects an electron from the molecule, resulting in a cation and two outgoing electrons. This thesis concentrates on dissociative electron ionisation events, in which the parent cation dissociates into fragments.

It takes 50 as (5×10^{-17} s) for an electron with 50 eV of kinetic energy to travel 2 Å, which is typical of the length of a chemical bond.[26] Given that a molecule's rotational and vibrational periods are of the order of hundreds of picoseconds (10^{-10} s) and hundreds of femtoseconds (10^{-13} s), respectively,[27] the nuclear framework of the molecule can be considered to be essentially static on the timescale of ionisation. Therefore, the Franck-Condon principle[28] applies and the transition of the system from the neutral state to the ionic state can be treated as vertical.

Consider the ionisation of a molecule, AB, by an incident electron:

$$\mathrm{AB} + \mathrm{e}^-(E_\mathrm{i}) \longrightarrow \mathrm{AB}^+ + \mathrm{e}^-(E_\mathrm{f}) + \mathrm{e}^-(E_\mathrm{e}), \tag{1.1}$$

where E_i is the initial kinetic energy of the incident electron, E_f is its final kinetic energy and E_e is the kinetic energy of the ejected electron. In essence, the electronic state in which AB^+ is formed depends on which orbital an electron is ejected from.

The energy, ΔE, transferred in the collision is given by $\Delta E = E_\mathrm{f} - E_\mathrm{i}$. Any portion of the incident electron's initial kinetic energy can be transferred, so the magnitude of ΔE is only restricted by E_i. Since electron ionisation is a collisional process, it is not governed by optical selection rules. As a consequence, a large number of initial electronic states of the cation may be accessible.[29] By contrast, when a molecule is photoionised, a known quantity of energy is deposited into the system. Furthermore, photoionisation is governed by optical selection rules, so there are tight constraints on the final electronic states that are accessible.[30,31]

After subtracting the vertical ionisation energy of the ejected electron from ΔE, the remaining energy is distributed between AB^+ and the ejected electron.[29] By comparing the kinetic energy of ionic fragments produced by electron ionisation with E_i, it is evident that most of this remaining energy is carried away by the ejected electron,[32] and electron ionisation transfers very little energy directly to the nuclear framework. This is unsurprising given the disparity in mass between the nuclei and the electron.

If the incident electron energy surpasses the double or triple ionisation threshold, a doubly- or triply-charged ion can be formed. Multiple ionisation can occur via Auger-Meitner decay.[28] If an inner electron is ionised, a vacancy is left in a core orbital. A second electron can then fall into the vacancy, releasing a photon of sufficient energy to eject a valence electron.

Alternatively, outgoing electrons can interact with outer electrons as they depart from the molecule. In conjunction with the sudden change in effective nuclear charge as the molecule is ionised, this can be sufficient to excite a valence electron to the extent that it is ejected from the molecule, forming a doubly-charged ion. This mechanism is known as shake-off.[33,34]

1.1.2 Electron ionisation cross-section

The probability of a particular scattering event occuring can be quantified by a cross-section, with dimensions of area. In the context of electron ionisation, there are two cross-sections to consider: the total and partial electron ionisation cross-sections.

The *total ionisation cross-section* expresses the probability that an incident electron ionises the target molecule, and is a function of electron kinetic energy. This quantity can be crudely interpreted as the cross-sectional area of the molecule that the electron must strike in order to eject electrons; the larger the area, the higher the probability of ionising the molecule. As the electron energy increases from threshold, the total ionisation cross-section increases, which can be understood as follows. When the electron's energy is close to the molecule's ionisation energy, essentially all of the electron's kinetic energy must be transferred to ionise the molecule. Roughly speaking, this necessitates a head-on collision at the centre of the molecule. As the electron's energy increases, a smaller portion of the total is required to ionise the molecule. Glancing collisions will transfer the requisite energy, so the cross-section increases.[35] Typically, the total ionisation cross-section peaks at around 70 eV. Hagstrum rationalised this by considering the molecule as a resonant system, which experiences a pulse disturbance by the passage of the incident electron.[36] Under this model, the probability that the molecule absorbs enough energy to be ionised depends on the magnitude of the Fourier component in the pulse that is resonant with the energy change required in the molecule. As the electon's velocity increases, the lower frequency components necessary for ionisation decrease, thus decreasing the total ionisation cross-section.

Several experimental techniques have been used to measure the total ionisation cross-section, $\sigma_{\mathrm{T}}(E)$, of a molecule at a particular electron energy, E.[15,37,38] For

instance, in a beam-gas scattering experiment, $\sigma_{\mathrm{T}}(E)$ can be determined from accurate measurements of four quantities: the current, I_- of the ionising electron beam; the ion current, I_+, produced when the electron beam interacts with the target gas; the number density, n, of the gas; and the path length, l, over which the electron beam interacts with the target gas. Using the Beer-Lambert law, and assuming that the sample number density is sufficiently low, it can be shown that:[39]

$$\frac{I_+}{I_-} = n\sigma_{\mathrm{T}}(E)l. \tag{1.2}$$

A number of semi-classical and semi-empirical models exist to calculate the total ionisation cross-section theoretically,[15] including the Deutch-Märk (DM) method[40–42] and the Binary-Encounter-Bethe (BEB) model.[43] Both approaches are based on determining a cross-section for each molecular orbital, using the incident electron's kinetic energy and orbital parameters such as the binding energy, occupation, mean-square radius (in the case of the DM method) and kinetic energy (for the BEB model). The molecule's total ionisation cross-section can then be found by summing the cross-section for each orbital.[15]

A *partial ionisation cross-section* quantifies the probability of forming a specific product ion at a particular electron energy.[44] It follows that the sum of the partial ionisation cross-sections for all possible fragment ions of a molecule equals its total ionisation cross-section:

$$\sigma_{\mathrm{T}}(E) = \sum_i \sigma_{\mathrm{P},i}(E), \tag{1.3}$$

where $\sigma_{\mathrm{P},i}(E)$ is the partial ionisation cross-section for ion, i, at an electron energy, E. Experimentally, partial ionisation cross-sections can be determined by measuring the relative branching ratios for product ions and normalising the total to the

total ionisation cross-section.

Now that the mechanisms by which an electron-molecule collision can form an ion have been established, the forces driving molecular ions to dissociate will now be discussed.

1.2 Potential energy surfaces

A chemical reaction can be understood by considering the potential energy surface(s) involved in the process. A potential energy surface (PES) quantifies the potential energy of a molecular system in a given electronic state as a function of the nuclear coordinates,[45] with the topography of the PES governing how the system evolves over time. Consider the dissociation of a molecule with N atoms. The force, $\mathbf{F}(\mathbf{R})$, acting on the nuclei with coordinates $\mathbf{R} = \{\mathbf{R_1}, \mathbf{R_2}, ..., \mathbf{R_N}\}$, is related to the potential energy, $V(\mathbf{R})$ by:

$$\mathbf{F}(\mathbf{R}) = -\boldsymbol{\nabla} V(\mathbf{R}). \tag{1.4}$$

From this equation, the gradient of the potential energy surface determines the forces experienced by the nuclei at a particular geometry. Much progress has been made in calculating potential energy surfaces,[46] using a multitude of electronic structure methods. With knowledge of the potential energy surface for a reaction, the dynamics can be predicted by conducting either a quasi-classical trajectory calculation, or a full quantum mechanical wavepacket simulation.[45]

A non-linear molecular system can be fully characterised by a set of $3N - 5$ internal coordinates, where N is the number of atoms in the system. As the system becomes more complex and N increases, potential energy surfaces fully describing a reaction can become difficult to visualise and expensive to compute. Therefore,

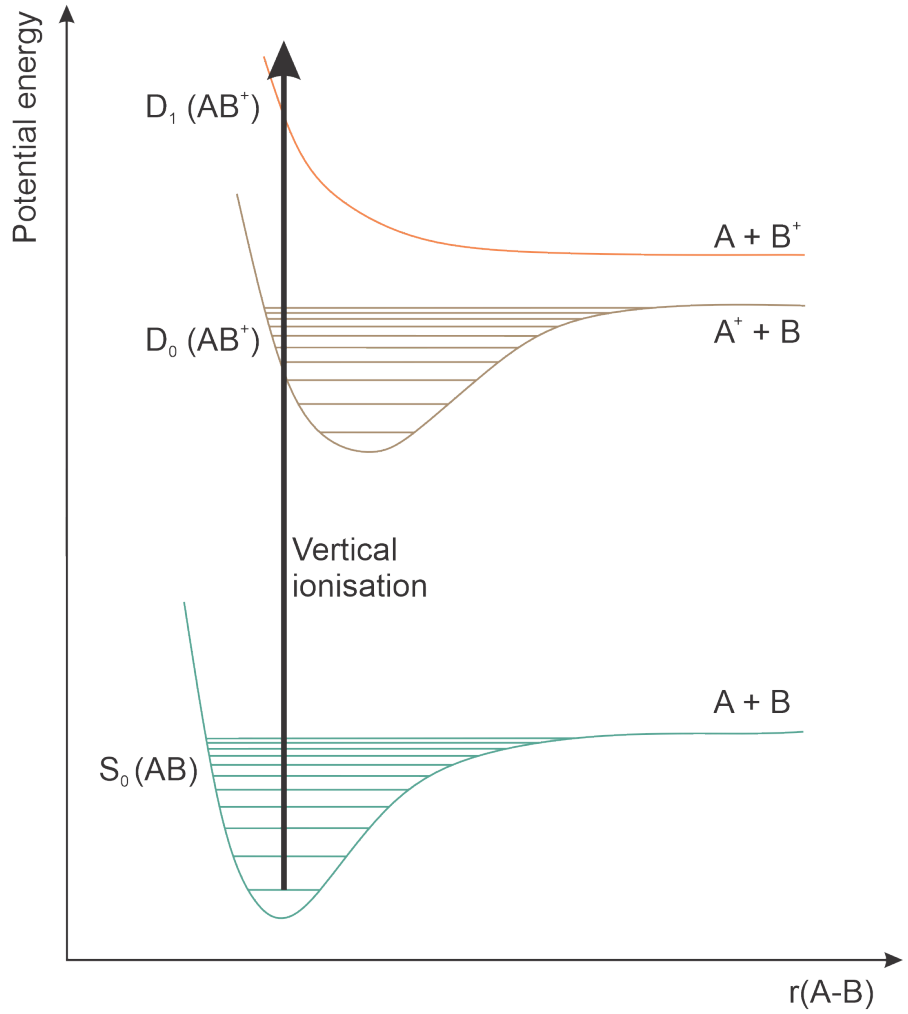


Figure 1.1: A schematic diagram of potential energy surfaces relevant to the dissociative electron ionisation of a simple diatomic molecule, AB, plotted as a function of A-B separation, r(A-B). States are labelled according to their electronic spin (S for singlet, D for doublet, etc.) and the species they correspond to.

it is often necessary to plot a PES as a function of one or two coordinates. For instance, when considering a reaction in which one chemical bond is broken, the PES is often plotted as a function of the length of the bond being broken. This simplification will be used extensively when considering potential energy surfaces for the dissociation processes presented in Chapters 4 and 5.

For illustration, consider the dissociative electron ionisation of a simple diatomic molecule, AB. Figure 1.1 shows some relevant potential energy surfaces, including

the ground state of the neutral molecule, $S_0(AB)$, and the ground and first excited states of the cation, $D_0(AB^+)$ and $D_1(AB^+)$.

The arrow indicates how electron ionisation populates electronic states of the parent cation, AB^+, by vertical ionisation. As previously discussed, electron ionisation is an ultrafast process; thus, the nuclei are considered to be stationary during the ionisation event, and the neutral molecule's ground-state geometry is initially preserved. Consequently, the transition follows the Franck–Condon principle.[28] The transition probability, P_{fi}, depends on the overlap between the vibrational wavefunctions of the initial state, $\chi_i(\mathbf{R})$, and the final state, $\chi_f(\mathbf{R})$:

$$P_{fi} \propto |\langle \chi_f(\mathbf{R}) | \chi_i(\mathbf{R}) \rangle|^2. \tag{1.5}$$

Often, the ground state of a cationic molecule has a larger equilibrium bond length than the corresponding neutral: in Figure 1.1 the minimum of the $D_0(AB^+)$ state is offset to a larger A-B separation than that for the $S_0(AB)$ state.

Both the $S_0(AB)$ neutral ground state and $D_0(AB^+)$ ionic ground state are bound, and have defined vibrational and rotational levels. If the $D_0(AB^+)$ state is populated with an energy below the ion's dissociation threshold, the ion is formed intact in a series of vibrational states according to the Franck-Condon overlap. If, however, the $D_0(AB^+)$ state is populated above the dissociation threshold, the ion dissociates.

The first excited electronic state of the ion, $D_1(AB^+)$, is a repulsive state. The system is able to minimise its potential energy by increasing the A-B separation. By Equation 1.4, the force acting on the nuclei as a result of the potential energy gradient drives the nuclei apart and promptly breaks the bond between the two atoms.

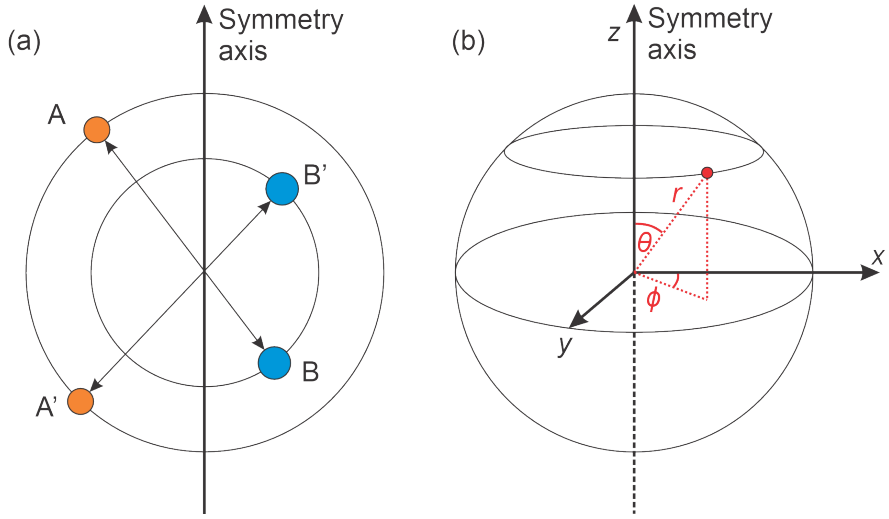


Figure 1.2: (a) Two dissociation events of an AB molecule forming A and B fragments with equal and opposite momenta. (b) A diagram of a Newton sphere, where the z axis is the axis of cylindrical symmetry. The radius, r, polar angle from the symmetry axis, θ, and azimuthal angle ϕ are the coordinates that define an ion's location on the Newton sphere surface.

1.3 Scattering distributions

When a molecule dissociates, product formation is typically accompanied by the release of translational kinetic energy. Consequently, product fragments recoil away from each other. Consider the dissociation of an excited molecule, AB*, to form A and B fragments in a two-body process:

$$\mathrm{AB}^* \longrightarrow \mathrm{A} + \mathrm{B} + \mathrm{TKER}. \tag{1.6}$$

In the simple two-body case illustrated in Figure 1.2 (a), fragments A and B recoil from one another with equal and opposite momenta. If many randomly-oriented AB molecules dissociate, the fragments will form a series of expanding concentric spheres, known as Newton spheres.[47] These spheres are cylindrically symmetric about the relative velocity vector of the scattering partners; in the case of an electron-molecule scattering event, the electron's velocity is typically orders of magnitude larger than the molecule's velocity, so the relative velocity

vector, and thus the symmetry axis, can be taken as the electron propagation vector to a good approximation (see Section 3.3 for more details). The radial and angular distributions of fragments on the surface of a sphere are characteristic of the dissociation process; they are defined by their radius, r, polar angle from the symmetry axis, θ, and azimuthal angle, ϕ (as illustrated in Figure 1.2 (b)).

A sphere's radius depends on fragment velocity, so fragment momentum and kinetic energy can be inferred from the radial distribution. The total energy of AB* is partitioned between the internal energies of the products and the total kinetic energy release (TKER). The TKER, in turn, is divided between K_{A} and K_{B}, the kinetic energies of fragments A and B, respectively. By invoking the conservation of linear momentum, the following equations can be obtained for K_{A} and K_{B}:

$$K_{\mathrm{A}} = \frac{m_{\mathrm{B}}}{M_{\mathrm{AB}}}\mathrm{TKER} \tag{1.7}$$

$$K_{\mathrm{B}} = \frac{m_{\mathrm{A}}}{M_{\mathrm{AB}}}\mathrm{TKER}. \tag{1.8}$$

Here, m_{A} and m_{B} are the masses of A and B, respectively, and M_{AB} is the combined mass of A and B. In this way, even if only one of the fragments can be detected, the total kinetic energy released in the fragmentation can be determined. If the initial energy of AB* is known, the internal energy of the products can also be inferred by conservation of energy.

Since the scattering distribution is cylindrically symmetric, it is invariant with respect to ϕ. However, scattering distributions very often display a dependence on θ. The angular distribution can be expanded as a sum of Legendre polynomials, such that the overall scattering distribution, $I(r, \theta)$ can be written as:

$$I(r,\theta) = I(r)\left(1 + \sum_{n>0} \beta_n P_n(\cos\theta)\right), \tag{1.9}$$

where $I(r)$ is the radial distribution, P_n is the n^{th} Legendre polynomial and β_n is the n^{th} anisotropy parameter.

Anisotropy parameters quantify the distribution's dependence on θ. If all anisotropy parameters are zero, the scattering distribution is said to be isotropic. In the case of a photoinduced process, in which AB is excited by a laser pulse, the product distributions often exhibit a dependence on θ due to the interaction of the polarisation vector of the excitation light with the transition dipole moment for the electronic transition occurring.[48]

Dissociative electron attachment reactions often yield anisotropic scattering distributions, depending on the initial electronic state of the molecule and the final electronic state of the transient negative ion.[49] In contrast, scattering distributions resulting from non-resonant electron ionisation are often isotropic.[26,29,50] However, the ionisation cross-sections of some molecules, often with large dipole moments, depend on the orientation relative to the incident electron.[51,52] If the subsequent bond cleavage is prompt relative to the molecule's rotational period, this anisotropy would be expected to be preserved in product scattering distributions.

It has been established that product scattering distributions contain a wealth of information on the dynamics of molecular dissociation. The next section discusses the experimental techniques used to measure these scattering distributions in the gas phase.

1.4 Velocity-map imaging

Scattering distributions for the ionic products of molecular dissociation can be measured by ion imaging. The first experiment to implement this technique was reported in 1987 by Chandler and Houston,[53] who imaged the photodissociation products of methyl iodide (CH_3I). Briefly, a pulsed beam of CH_3I was intersected by an unfocussed 266 nm pump laser beam, which initiated C-I bond cleavage. Dissociation products then expanded as a series of Newton spheres, with radii dependent on the fragment's recoil velocity and the time after the fragment was formed. Shortly after the pump laser pulse, a focussed 366 nm probe beam ionised the CH_3 fragment by multi-photon ionisation. All interactions between the molecular beam and laser beams occurred between two electrodes: a repeller plate, to which a positive potential was applied; and a grounded mesh. The grounded mesh allowed ions to travel through, whilst ensuring that the electric field between the two electrodes remained homogeneous (see Figure 1.3(a)). Ions formed during the probe pulse were accelerated by the electric field along a flight tube to a position-sensitive detector.

The spatial and therefore velocity resolution of the measured image was limited by the fact that the interaction volume between the molecular beam and the laser beams has a finite size, so ions do not originate from a single point within the electric field. In 1997, Eppink and Parker introduced the velocity-map imaging (VMI) technique, which overcame this limitation.[55] The key difference was in the design of the ion lens. Whilst Chandler and Houston relied on a homogeneous field to accelerate ions to the detector, Eppink and Parker used an inhomogeneous field. This was achieved by removing the mesh covering the second plate and adding a third plate that was held at ground potential. The resulting assembly,

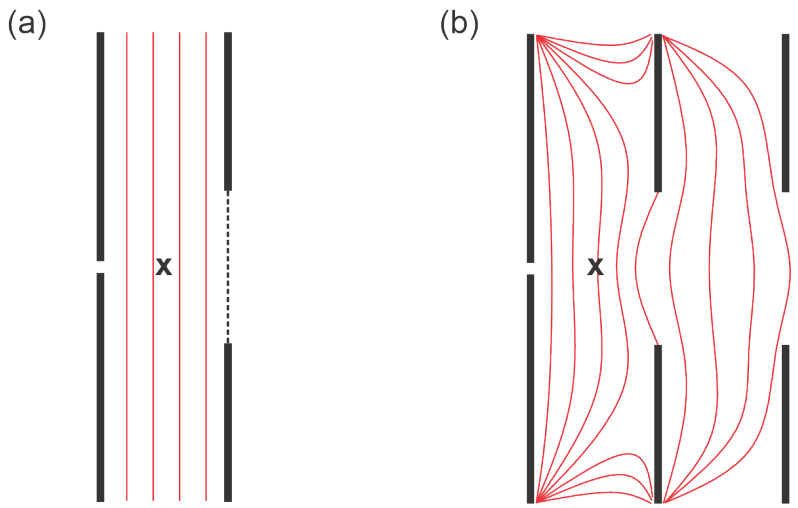


Figure 1.3: Schematic diagrams of (a) a spatial-mapping ion lens of the sort employed in Chandler and Houston's 1987 demonstration of ion imaging,[54] where the dotted line indicates a wire mesh, and (b) a three electrode VMI ion lens, of the sort first used by Eppink and Parker.[55] Red lines indicate electric field contours and the interaction region between the molecular beam and ionising beam is indicated with a black cross.

which consisted of the repeller, extractor and ground electrodes is illustrated in Figure 1.3(b). Using this design, all ions with the same velocity and mass-to-charge ratio are mapped to the same point on the detector, such that an ion's radius from the image centre is proportional to its velocity in the plane of the detector. Consequently, detailed information on ion velocity and angular distributions can be extracted from the images.

VMI experiments using the simple three-electrode ion lens, of the sort introduced by Eppink and Parker, crush the 3D Newton spheres along the time-of-flight axis, so that the experiment records 2D projections of the full 3D scattering distribution. Therefore, velocity information along the time-of-flight axis is lost. In order to properly obtain product velocity and angular distributions, the 3D scattering distribution must be reconstructed by recovering the central slice, in a process known as image inversion.[56,57] A number of inversion methods exist and will be discussed in more detail in Section 3.3.

Eppink and Parker also demonstrated spatial-map imaging, in which the position

an ion strikes the detector depends on the position at which it was formed in the interaction region. Whilst information on ion velocities is lost, this technique is useful when optimising an experiment, enabling the user to visualise the path of the ionising beam and ensure it is spatially overlapped with the molecular beam.

Several experiments have also sought to record the 3D scattering distribution directly by implementing 'slice imaging', which involves adding additional electrodes to the ion lens to stretch the Newton spheres along the time-of-flight axis. The detector is then gated to capture only the central slice of the stretched scattering distribution. Examples of this approach include the work of Gebhardt *et al.*[58] and Townsend *et al.*[59] Improvements in the time resolution of imaging sensors have raised the prospect of recording multiple slices through the 3D scattering distribution, which can then be reconstructed by stacking adjacent time slices. In this way, velocity information along the time-of-flight axis can be obtained. An example of this approach is the work of Lee and co-workers, in which the Coulomb explosion products of CF_3I were imaged, using a PImMS sensor with a time resolution of 12.5 ns to record multiple slices through the scattering distribution of each fragment ion.[60] For more information on the PImMS sensor, please refer to Section 2.5.

1.5 Molecular sample preparation

1.5.1 Gaseous samples

Typically, gas phase samples are introduced into a high-vacuum experiment by expansion through a small orifice to form a molecular beam. Two types of molecular beam source exist: effusive and supersonic, depending on the orifice diameter, ϕ, and mean free path, λ, of gas in the source. Which type of beam is generated depends upon the Knudsen number, K_n.

$$K_n = \frac{\lambda}{\phi}. \tag{1.10}$$

When $K_n > 1$, an effusive beam is formed. Molecules only exit through the orifice when they encounter it. The result is a beam with a relatively broad distribution of velocities and a $\cos^2\theta$ angular distribution, where θ is the angle between a molecule's trajectory and the beam axis.

A supersonic beam is formed when $K_n < 1$, i.e. when a gas molecule's mean free path is significantly smaller then the orifice diameter. Under these conditions, many collisions between gas molecules take place at the orifice, with those collisions that impart velocity along the beam axis being most successful in ejecting a molecule through the orifice. Molecules in the beam have had almost all of their random translational energy and internal energy converted into translational kinetic energy directed along the beam axis by collisions. The result is a beam with a narrow, supersonic velocity distribution, within which the molecular trajectories lie almost entirely along the beam axis. Beam molecules have almost no internal energy, so occupy only very low rotational and vibrational quantum states. The number density of gas is also significantly larger than in an effusive beam, making a supersonic molecular beam more suitable for experiments in which the number of interactions between the ionising beam and molecular beam needs to be maximised. Further details on a pulsed solenoid valve, which is commonly used to form a supersonic molecular beam, are provided in Section 2.1.

After exiting the valve, shock zones develop due to the supersonic beam velocity.[61,62] A barrel shock forms around the the centreline of the expanding beam, followed by a Mach disk perpendicular to the gas flow. In order to ensure that a collimated, internally cold beam is formed, these shock regions must be excluded. A

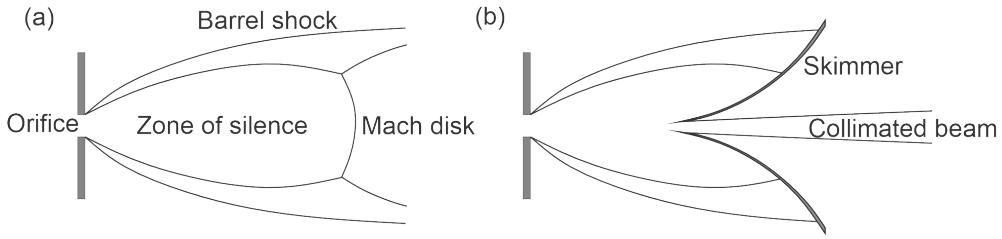


Figure 1.4: (a) A schematic diagram of the shock regions formed around the nozzle of a supersonic molecular beam source. A skimmer is used to exclude the shock regions from the scattering chamber, as illustrated in (b). Figure adapted from Reference [61].

skimmer (Figure 1.4(a)) is positioned 2 to 3 cm after the orifice, before the Mack disk forms, so that only molecules from the internally cold zone of silence pass through.

1.5.2 Solid samples

Advances in gas-phase ion imaging experiments in recent years, for instance the introduction of multi-mass imaging experiments,[56] allow the dissociation dynamics of larger, more complex systems to be measured and understood. However, preparing large, complex molecules in the gas phase can be challenging, as they typically have low vapour pressures and may even be solid at room temperature. Different approaches have been adopted to circumvent this, many of which involve heating the sample to increase its vapour pressure, allowing it to be seeded in a carrier gas.

One such example is the Even-Lavie valve, which is capable of heating a sample to temperatures of up to 550 K within the body of the valve[63] and has been employed to prepare various compounds, including small PAHs.[64–66] However, whilst the Even-Lavie valve is able to entrain a solid sample into a supersonic molecular beam, its purchase cost is prohibitive for most laboratories. Furthermore, prolonged sample heating could cause the sample compound to thermally decompose if it is thermally labile.

Electrospray ionisation (ESI) and matrix-assisted laser desorption/ionisation (MALDI) are both widespread techniques for preparing ionic biomolecules in the

gas phase;[67,68] for instance, electrospray ionisation has been employed to prepare β-galactosidase, an enzyme with a mass of 465 kDa, in the gas phase, so that it could be deposited an a surface for high-resolution cryo-electron microscopy.[69] However, these techniques cannot be used to prepare neutral molecules.

Laser-induced desorption is a technique that can bring neutral molecules into the gas phase intact. The solid sample is coated on the front of a thin foil, and a laser irradiates the rear of the foil, causing sample molecules to desorb into the gas phase. If a pulsed desorption laser is used, the technique is often termed laser-induced acoustic desorption (LIAD).[70–72] There is some debate about the precise mechanism for desorption in this case, but it seems that acoustic waves spawned by laser pulses propagate through the foil and cause molecular desorption.[70] Pulsed laser sources have been successfully applied to prepare systems as large as individual red blood cells in the gas phase.[73]

Alternatively, a continuous wave (CW) laser can be used, which has the benefit of simplifying the experimental setup. In this case, the technique is simply termed laser-induced desorption (LID). Thermal desorption of substrate is the dominant desorption mechanism in this case, caused by the localised heating of the foil at the laser focus.[74] DNA nucleosides,[74] uracil,[75] phenylalanine,[76] among other biomolecules have all been prepared in the gas phase by this technique. Despite the thermal desorption mechanism, this approach is less likely to cause thermal decomposition of the sample. Heating of the foil is localised at the laser focus; each area of the substrate is only heated and desorbed when the foil directly behind it is irradiated by the focussed laser. Therefore, the substrate compound is not heated for a prolonged period prior to desorption. Recently, a LID source has been developed by Milsevic *et al.* and has been employed to study polycyclic aromatic hydrocarbons in the gas phase.[77,78] This design is described in more detail in Section

2.2 and is characterised for use on the electron-molecule crossed beam experiment in Chapter 6. It is then applied to study the dissociative electron ionisation of a polycyclic aromatic hydrocarbon in Chapter 7.

1.6 Outline of this thesis

This chapter has introduced the key concepts underlying the study of electron-induced molecular fragmentation. Chapter 2 outlines the experimental methods employed to investigate these processes, while Chapter 3 details the procedures for processing and analysing the resulting data sets. These techniques are then applied to the study of the dissociative electron ionisation of CF_3I in Chapter 4, and of CH_3F and CH_3Cl in Chapter 5. This work concentrates on electron energies just above the molecule's ionisation threshold, aiming to resolve the contributions of low-lying electronic states of the parent cation to the dissociation pathways. Subsequently, a laser-induced desorption source is characterised for use on an electron-molecule crossed beam experiment in Chapter 6, enabling the study of larger and more complex molecules. This new source is finally applied to explore the dissociative electron ionisation dynamics of the polycyclic aromatic hydrocarbon triphenylene.

2
Experimental Methods

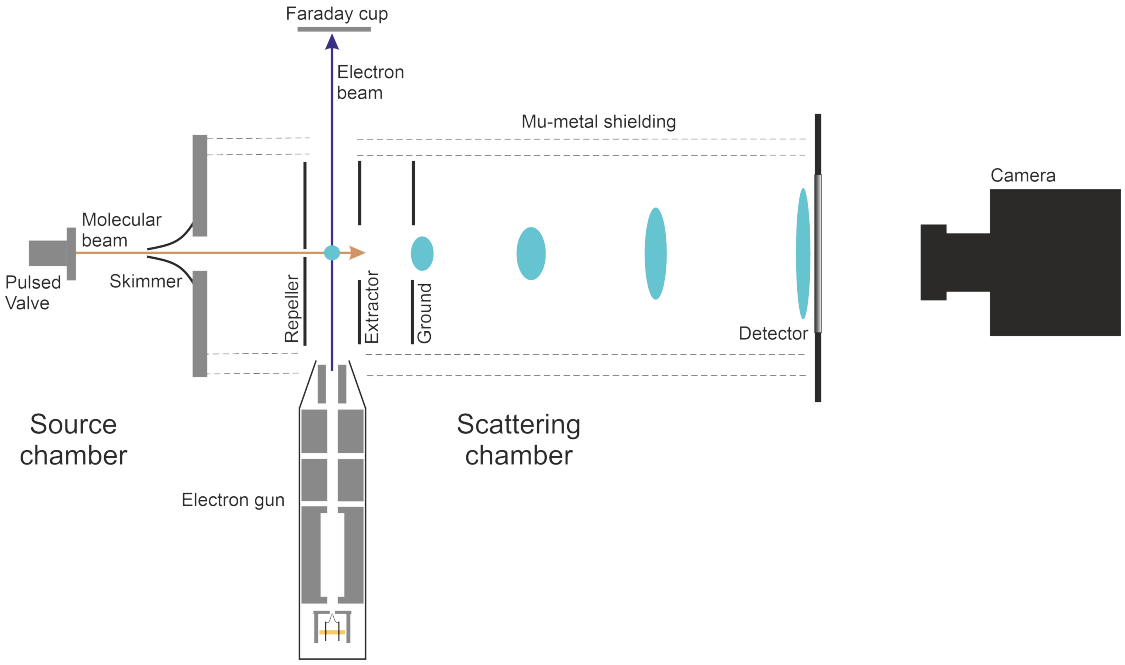


Figure 2.1: Schematic illustration of the electron-molecule crossed beam experiment, with the key components labelled.

All of the experimental data presented in this thesis were acquired using the electron-molecule crossed-beam experiment, illustrated in Figure 2.1. The experiment consists of two chambers: the source chamber, where the molecular source is located, and the scattering chamber, where molecules are ionised by

the electron beam and detected.

Each chamber is maintained at a pressure of approximately 10^{-7} mbar by a turbomolecular pump (Pfeiffer Vacuum, HiPace1800 and HiPace700 for the source chamber and scattering chamber, respectively), each of which is backed by a scroll pump. High vacuum conditions are required so that ion trajectories are not affected by collisions with background gas molecules in the chamber.

Care must be taken to eliminate stray electric and magnetic fields from the scattering chamber to prevent electrons or ions from being deflected. Electrons are especially sensitive to such fields due to their low mass, meaning that even weak magnetic fields can significantly alter their trajectories within the electron beam. To minimize these effects, the experimental region containing charged particles, including the ion optics, time-of-flight tube, and electron gun tip, is enclosed in mu-metal shielding.

Each aspect of the experiment, from introducing molecules into the source chamber to recording ions, will now be discussed in more detail.

2.1 Molecular beam

Gaseous compounds, such as CF_3I (discussed in Chapter 4), CH_3F and CH_3Cl (both discussed in Chapter 5), are introduced into the source chamber by supersonic expansion via a pulsed solenoid valve (Parker Hannifin, Series 9). The sample gas is first seeded in Helium, a chemically inert carrier gas. Seeding the sample gas in a light carrier gas, in this case helium, reduces the average mass of molecules in the beam, thereby increasing their terminal velocity.[45] An additional advantage of using helium is that its ionisation energy (24.6 eV[79]) lies above most of the electron energies studied in Chapters 4 and 5. Therefore, it does not appear in most of the data sets. A 20:80 gas mixture (sample gas:Helium) with a total pressure

of 2.5 bar is prepared and fed to the valve.

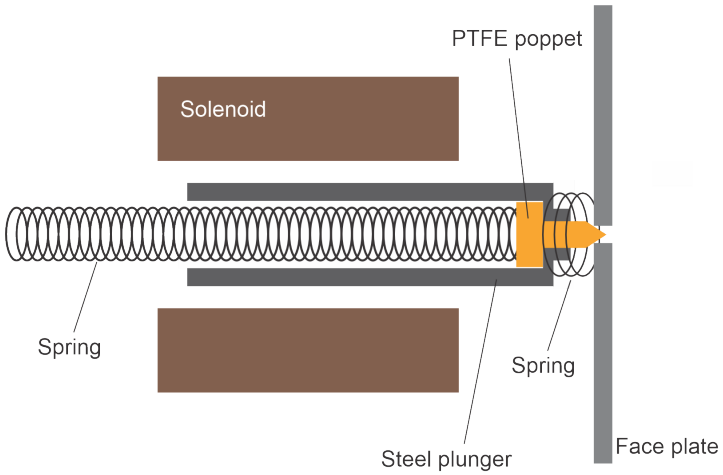


Figure 2.2: Schematic diagram of a pulsed solenoid valve, with the key components labelled.

A schematic diagram of the pulsed valve is displayed in Figure 2.2. A steel plunger houses a PTFE poppet, which seals the orifice in the faceplate when the valve is shut. In order to open the valve, current flows through the solenoid, generating a magnetic field that pulls the steel plunger, and thus the poppet, away from the faceplate. The gas mixture can then expand supersonically into vacuum through the orifice. At the end of the molecular beam pulse, the current is switched off and the plunger springs back, so that the poppet seals the orifice once again.

Several parameters can be adjusted in order to optimise the molecular beam for the experiment. Firstly, the valve opening duration is controlled by varying the length of time the current flows through the solenoid. Increasing the duration too much increases the background gas in the chamber and consumes the gas mix more quickly. However, if the opening duration is too short, the valve is not able to open fully and the resulting beam quality is poor. For the experiments in Chapter 4 and 5, the valve was opened for 200 μs for each cycle.

Varying the magnitude of the solenoid current affects the force pulling the steel plunger back. If this current is too small, the valve is not opened properly,

whereas if the current is too large, the plunger may bounce when it closes, causing the valve to temporarily reopen.

Adjusting how tightly the faceplate is screwed onto the body of the valve has a similar effect to varying the current. Loosening the faceplate reduces the tension in the springs that return the plunger to the closed position, and vice-versa when the faceplate is tightened. Therefore, if the faceplate is too tight, the valve cannot open properly; whereas if the faceplate is too loose, the poppet does not seal properly when the valve is closed.

2.2 Laser-induced desorption source

A laser-induced desorption (LID) source, based on the design reported by Milesevic *et al.*,[77] is used to prepare solid, non-volatile compounds in the gas phase. A plume of molecules is generated by localised heating of a thin layer of solid sample deposited on tantalum foil by a heating laser. In contrast to the beam generated by a pulsed solenoid valve, the molecular plume is continuous.

The LID source assembly, schematically illustrated in Figure 2.3, is mounted on the source chamber of the experiment in place of the molecular beam assembly. The skimmer is removed, allowing the foil to be positioned directly behind the repeller plate in the scattering chamber. A linear translator (MDC Precision MTM-12) allows the assembly to be extended and retracted between the source and scattering chambers, enabling straightforward sample replacement. The foil is aligned correctly behind the repeller plate by an X/Y translator.

A continuous wave 450 nm beam, produced by a diode laser (Thorlabs L450P1600MM) is coupled into an optical fibre (Newport F-MBC-C-1SMA) and brought into vacuum via an optical feedthrough (Avantes FC-VFT-UVIR400). A vacuum-compatible optical fibre (Thorlabs MV41L1) guides the light to a lens assembly, which first

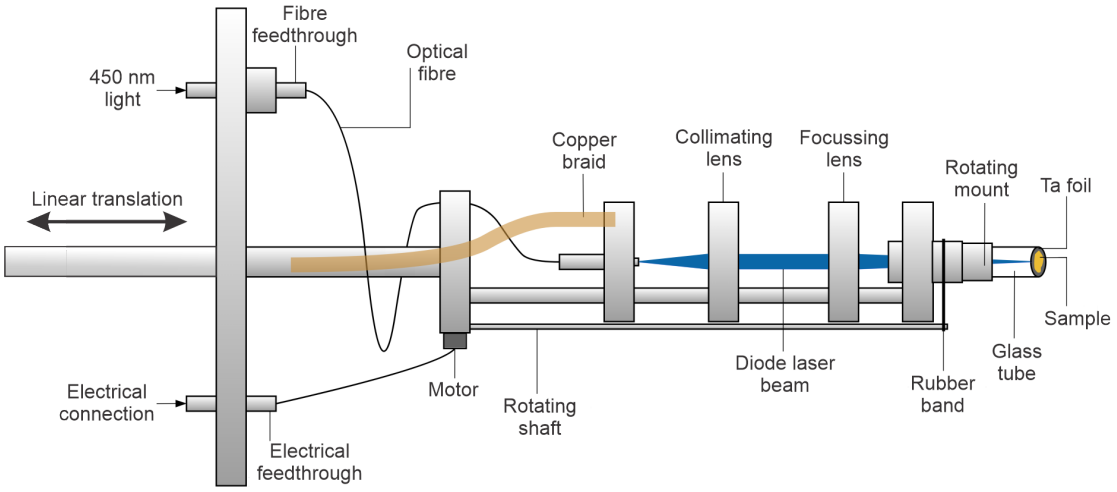


Figure 2.3: Schematic diagram of the laser-induced desorption source, with key components labelled. Figure adapted from Reference [80].

collimates the divergent fibre output and then focuses it onto the rear surface of a thin tantalum foil disc (GoodFellow TA000300/13, 12.5 μm thickness) coated with the sample compound.

Tantalum is selected for its high melting point and low thermal conductivity. Together with the low foil thickness, this ensures that heat on the foil surface is effectively localised at the laser focus, while lateral heat transfer across the foil is minimised. As a result, sample desorption occurs locally from a small region of the foil surface at the position of the laser focus.

The foil disc is adhered to the end of a glass cylinder mounted on a rotatable stage driven by a vacuum-compatible motor (Faulhaber, 0816P003SR K179, 3 V winding voltage). The laser beam is focussed off-centre on the foil, so that foil rotation replenishes the sample available for desorption.

The cooling of components is suppressed in vacuum, so measures are required to prevent overheating of the optical fibre. A copper braid is attached to the fibre mount, in order to transfer excess heat away from the fibre to the metal shaft of the assembly.

The beamline that directs light from the diode laser to the LID source foil is

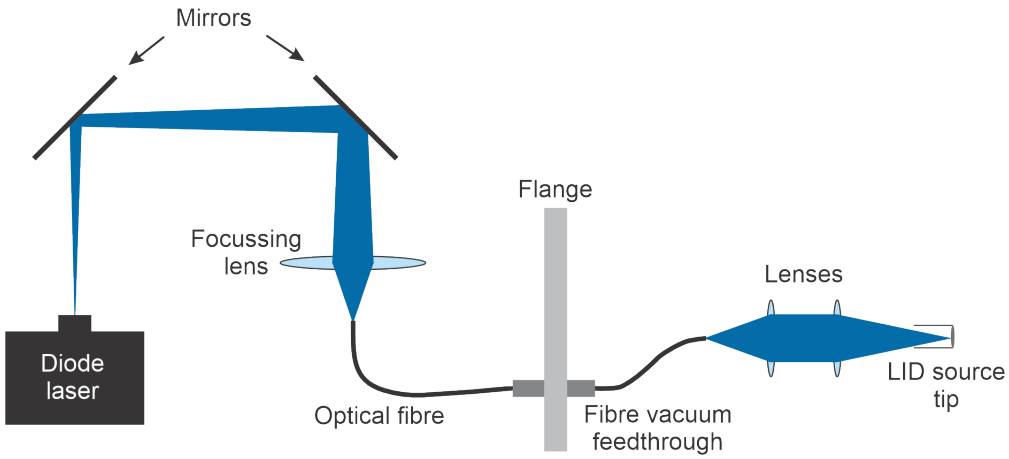


Figure 2.4: Schematic diagram of the beamline directing light from the diode laser to the LID source foil.

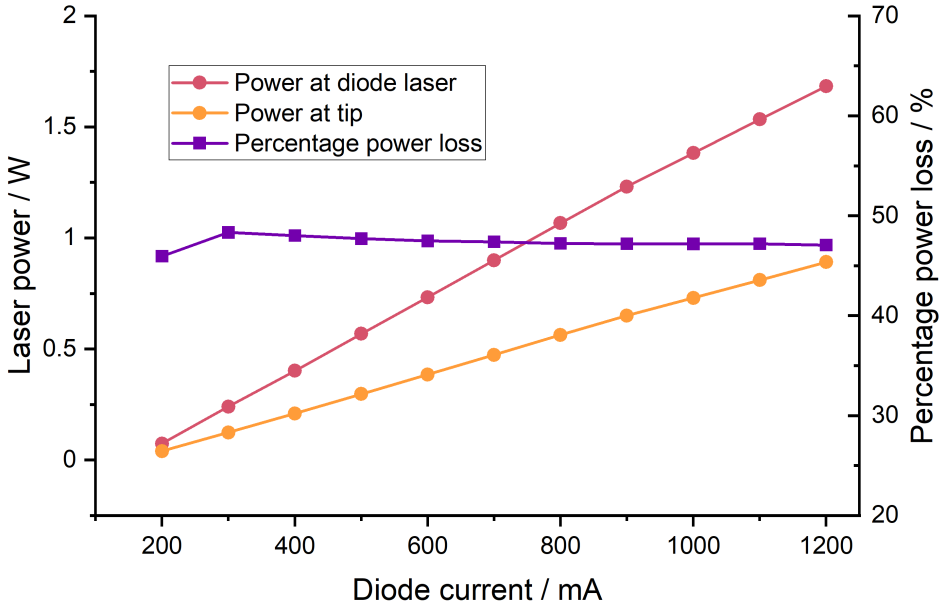


Figure 2.5: Plot showing diode laser power immediately after the diode laser and at the LID source tip as a function of diode current. At each current, the percentage loss in power is also plotted.

shown schematically in Figure 2.4. In order to evaluate beamline performance, power measurements were taken for a series of diode currents, both directly at the laser output and at the LID source foil. The results are plotted in Figure 2.5.

At the maximum routine operating current of 1200 mA, the power delivered

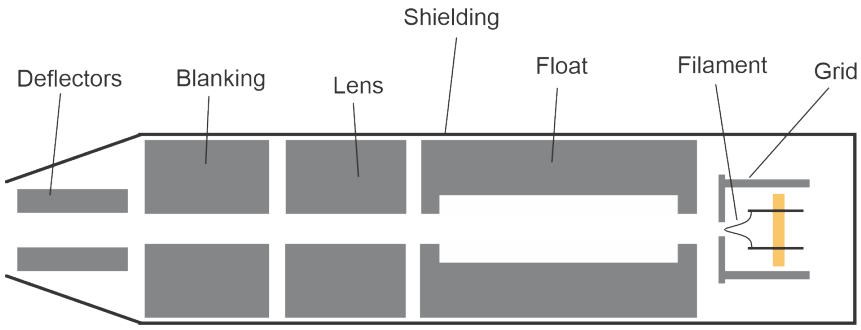


Figure 2.6: Schematic illustration of the Ionoptika IOE 10 electron source installed on the electron-molecule crossed-beam apparatus.

to the foil is 0.891 W. Power loss along the beamline, from the diode aperture to the foil, remains stable at approximately 47 % across the operating range. The majority of this loss occurs during coupling into the optical fibre and at the fibre connections of the vacuum feedthrough.

2.3 Electron gun

A commercial electron gun (Ionoptika IOE 10), which is schematically displayed in Figure 2.6, is mounted on the scattering chamber such that the electron beam it produces intersects the molecular beam at right-angles. Electrons are thermionically emitted from a Tungsten filament (Agar Scientific AGA054) as a result of passing a heating current of between 2.3 A and 2.35 A through the filament. A compromise is made between increasing the current to increase the intensity of the electron beam and limiting the current to extend the lifetime of the filament wire.

Electrons emitted from the filament then pass through an aperture in the grid electrode, which helps to collimate the beam. The float electrode, sometimes known as the anode, is a hollow cylindrical electrode that collimates the beam further before it is focussed by the lens electrode.

Whilst it is not possible to measure the spatial profile of the beam directly at the intersection with the molecular beam, an indirect measurement can be obtained

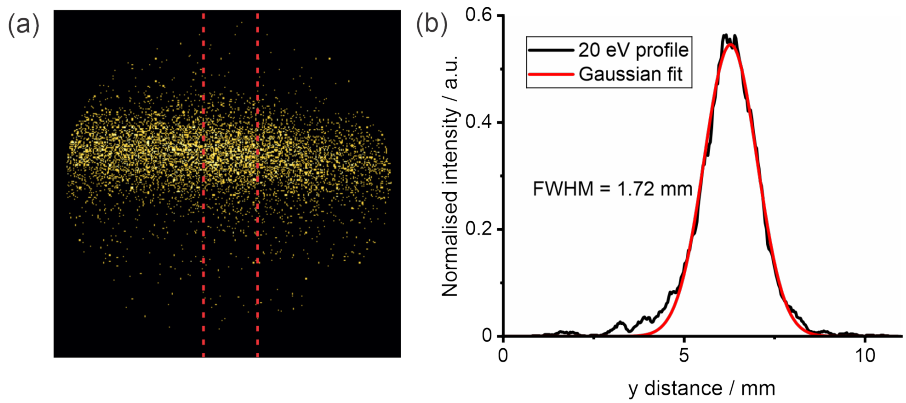


Figure 2.7: (a) Spatial-map image of H_2O^+ at an electron energy of 20 eV. Panel (b) plots the intensity of the image as a function of y coordinate, averaged over the central 50 pixels of the image in the x direction (between the two dotted red lined in panel (a)). Units have been converted from pixels in the image to distance in the interaction region, in mm, by means of SIMION ion trajectory simulations. A moving average of 7 pixels has been applied to the raw intensity plot, which has also been fitted with a Gaussian function.

by imaging the ions produced from the ionisation of background gas in the electron beam path under spatial-mapping conditions (see Section 1.4). For example, Figure 2.7 (a) shows the spatial-map image of background H_2O^+ at an electron energy of 20 eV. The spatial profile of the beam is obtained by plotting the intensity of the image in the y axis of the image, displayed in Figure 2.7(b). By employing the results of an ion trajectory simulation using the SIMION software package, the scale of image pixels can be converted to a scale of distance in the interaction region. The Gaussian function fitted to this intensity profile has a FWHM of 1.72 mm, which is indicative of the diameter of the electron beam as it passes through the interaction region. Generally, achieving a focussed and collimated electron beam becomes more difficult as the electron energy decreases, since space-charge repulsion between electrons has a more significant effect on their trajectories.

The beam can be pulsed on and off by an appropriate potential to the blanking electrode. When the beam is off, the electrode is held at a positive potential to deflect the beam away from the exit of the gun. In order to pulse the beam on, the

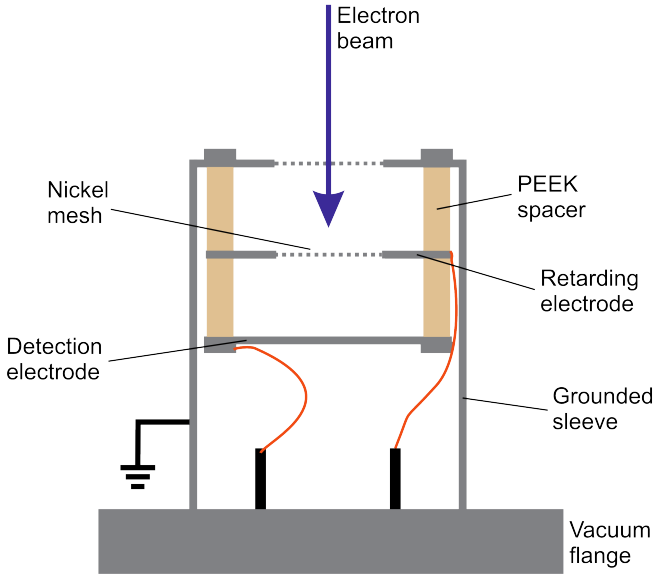


Figure 2.8: Schematic diagram of the assembly used to measure the kinetic energy distribution of the electron beam.

blanking electrode potential is switched to ground. A 'signal' data set, in which both the molecule under study and background gas present in the chamber are ionised, is acquired by triggering the electron beam pulse such that it intersects the molecular beam pulse. 'Background' data is obtained by triggering the electron beam to transit the interaction region before the molecular beam pulse arrives, so that only background gas is ionised.

Electrons emitted from the filament are accelerated through the potential difference between the filament, which is biased with a negative potential, and the interaction region, which is held at ground when the electron beam passes through. Therefore, by adjusting the bias voltage of the filament, the kinetic energy of the electron beam can be varied from 10 eV to 1000 eV. However, electrons are generated by thermionic emission with a range of kinetic energies, according to the temperature of the filament, which is reflected in the kinetic energy distribution of the electron beam. In order to measure this distribution, a detection assembly, illustrated in Figure 2.8, was constructed.

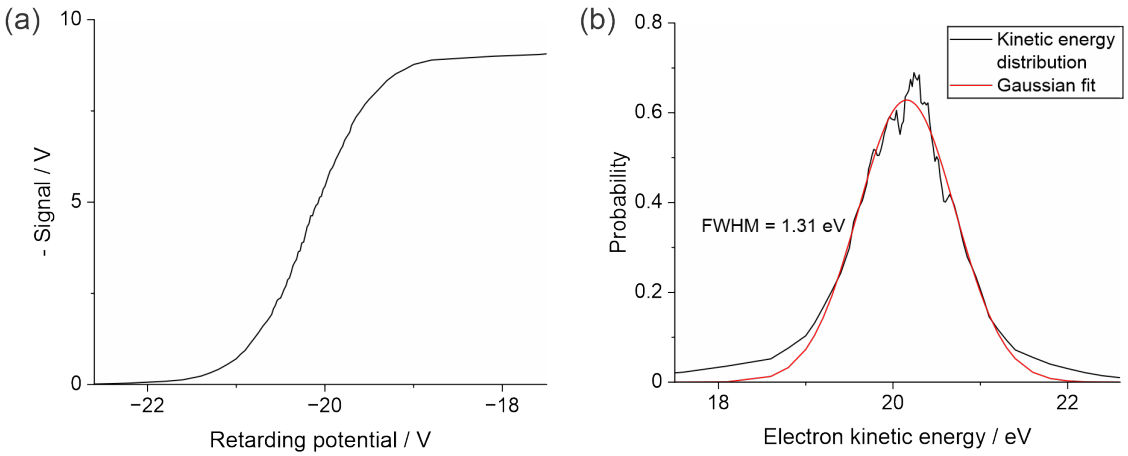


Figure 2.9: (a) The transmitted signal of a 20 eV electron beam plotted as a function of retarding potential. By taking the derivative of this plot, the kinetic energy distribution of the beam, displayed in (b), can be found.

The detection assembly consists of a series of circular steel electrodes housed within a grounded cylinder, which shields the surrounding vacuum chamber from internal electric fields. The incident pulsed electron beam enters through an aperture covered with a fine nickel mesh (Goodfellow NI008711/11, open area = 80 %). Behind this, a second circular electrode, also with a nickel mesh aperture, is biased with a negative retarding potential. Electrons with kinetic energies greater in magnitude than the applied potential pass through the aperture, whilst electrons with a lower kinetic energy are blocked. Transmitted electrons are recorded as a current at the detection electrode. The current pulses are amplified by a fast current amplifier (FEMTO DHPCA-100) and subsequently integrated by a boxcar averager (Stanford Research Systems SR250).

Figure 2.9 (a) plots the transmitted signal for a 20 eV electron beam, with 200 ns pulse duration and a 24 V blanking voltage. At each retarding voltage, data are collected for 250 electron beam pulses and an average transmitted signal is calculated.

At retarding potentials that are much less negative than −20 V, a large signal is observed, as all electrons in the nominally 20 eV beam have sufficient kinetic

energy to reach the current detection electrode. At potentials much more negative than −20 V, the electrons are unable to surmount the resulting potential barrier, and the signal falls to zero. The fact that the signal does not fall immediately to zero at -20 V, but rather decreases over a range of potentials, results from the spread of kinetic energies in the beam.

The distribution of kinetic energies in the beam, exhibited in Figure 2.9 can be found by calculating the first derivative of the transmitted signal with respect to the retarding voltage. Under these conditions at 20 eV, the distribution has a FWHM of 1.31 eV. Whilst pulse duration and electron energy have little effect on the distribution width, the blanking voltage employed to pulse the electron beam can have a significant effect. For example, with all other parameters identical, a blanking voltage of 100 V produces a distribution with a FWHM of 4.4 eV. Therefore, for all experiments conducted as part of this thesis, the minimum blanking voltage necessary to pulse the beam was selected.

2.4 Ion Optics

Ions formed in collisions between the electron beam and molecular beam/plume are extracted from the interaction region by the ion lens, which is displayed schematically in Figure 2.10, together with dimensions of the key components. The assembly is based on the design of Eppink and Parker[55] (see Section 1.4) and consists of three circular electrodes (the 'repeller', 'extractor' and 'ground' electrodes), which are separated by insulating PEEK spacers.

As the electron beam pulse travels through the ion lens, all electrodes are grounded so that the electron beam is not deflected from its path. Once the beam has passed through, fast switches bring the repeller and extractor electrodes to their set positive potentials in order to accelerate the cations formed. All ions with

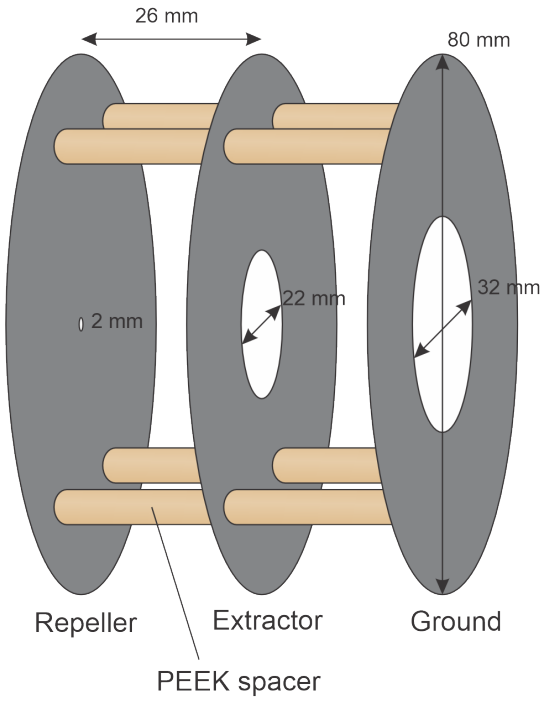


Figure 2.10: The ion lens with measurements of ion lens diameter, spacing and aperture diameters.

the same charge are accelerated towards the detector (along the time-of-flight axis) with the same kinetic energy. Consequently, ions with different mass-to-charge (m/z) ratios are accelerated to different velocities, so are separated in time at the detector. The electric field crushes the 3D spherical scattering distributions along the time-of-flight axis, so a 2D projection of the 3D scattering distribution is recorded at the detector.

Ion lens electrode potentials are set according to the experiment being undertaken. Under spatial-map imaging (SMI) conditions, ions are mapped onto the detector according to the position at which they were formed in the interaction region. Typically, this is acieved when the extractor voltage to repeller voltage (E:R) ratio is approximately 0.9. Experiments to acquire only mass spectra are normally conducted under these conditions, since all cations are recorded with the same spatial distribution on the detector, regardless of their velocity. Consequently,

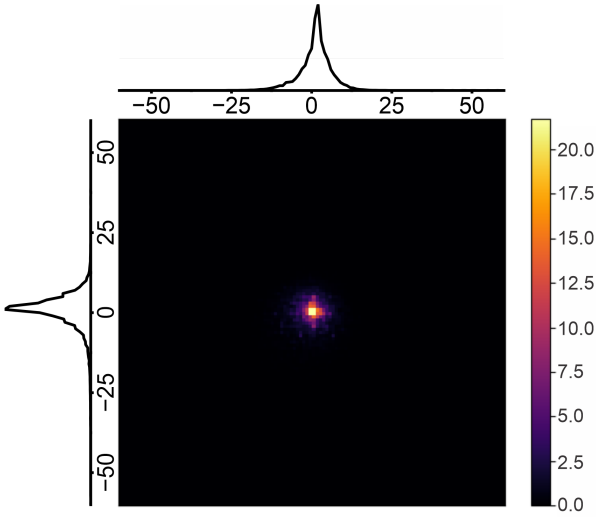


Figure 2.11: The ion image of CH_3F^+, recorded under velocity-mapping conditions at an electron energy of 20 eV. The x and y intensities of the image are projected onto the x and y axes in units of pixels.

each ionic product is detected with the same probability regardless of any detector inhomogeneity, making measurement of relative abundances more accurate.

For velocity-map imaging experiments, ions are mapped onto the detector according to their nascent velocity; all ions with the same velocity vector strike the detector at the same position, regardless of their point of formation in the interaction region. In order to achieve these conditions, the E:R ratio is typically set to approximately 0.7. Optimisation is carried out by minimising the area of the parent ion image on the detector. This ion is selected since its formation is not accompanied by any fragmentation that can impart a velocity component in the imaging plane (perpendicular to the ToF axis), and it therefore retains the narrow transverse velocity distribution of the molecular beam/plume. An example of an optimised CH_3F^+ parent ion image is exhibited in Figure 2.11

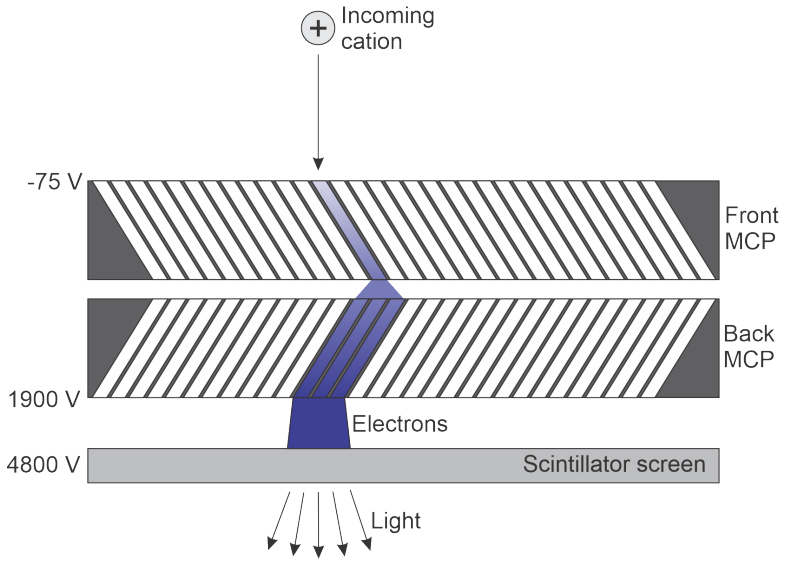


Figure 2.12: Schematic diagram showing how the MCPs amplify a single ion strike into approximately one million electrons, which are converted to a light signal by a scintillator screen.

2.5 Detector and Camera

Ions accelerated by the ion lens strike a position-sensitive detector, which constists of a pair of microchannel plates (MCPs) and a scintillator, and is displayed schematically in Figure 2.12.

An MCP is a resistive glass plate with an array of regularly arranged microchannels running through from one face to the other at a slight angle to the surface. The two plates are chevron-mounted, so that the channels in the second plate point in the opposite direction to the first. A potential of -75 V is applied to the front MCP to prevent low-energy scattered electrons from reaching the detector. Positive voltages of approximately 1800 V and 4800 V are applied to the back MCP and scintillator screen, respectively. When an incident ion strikes the inside of a channel of the front MCP, electrons are released from the wall. These are accelerated down the channel by the large positive potential difference, colliding with the channel walls and emitting more electrons. This process continues through

both MCPs, so that the signal from one ion strike is amplified into 10^4 to 10^7 electrons after the back MCP.[81] The electrons are then accelerated and strike the scintillator screen directly behind the channels they were emitted from, causing an optical signal to be emitted from the screen.

Light signals resulting from ion strikes on the detector are recorded by a Second-generation Pixel Imaging Mass Spectrometry (PImMS2) camera.[82–84] This is a multi-mass imaging sensor, which means that every ion produced, regardless of its identity, can be recorded in every experimental cycle, making data acquisition time-efficient. For each ion strike, a 324 × 324 array of pixels records the position (x, y) and arrival time, t, which is stored as a time code in the corresponding pixel of the camera. Each pixel can record up to four events per cycle, which is sufficient to capture all ion hits under our experimental conditions. The sensor is event-triggered, which means that rather than collecting data from the entire pixel array continuously, data points are only stored when a pixel senses an ion strike. In this way, the data storage requirement is drastically reduced.

2.6 Summary

This chapter has described each aspect of the electron-molecule crossed beam apparatus used to acquire data. Chapter 3 outlines how the data sets that result are processed and analysed.

3
Data processing and analysis

Now that the methods by which experimental data are acquired have been established, the techniques used to process and analyse the data will now be discussed. For each acquisition cycle of the experiment, a list of (x, y, t) data points, in which each point corresponds to a detected ion strike, are stored. The spatial position of the ion hit is recorded by the (x, y) coordinates, and the t coordinate corresponds to the ion's arrival time. For each experiment, two data sets are acquired: a signal data set, in which both the molecule under study and the background gas in the chamber are ionised, and a background data set, in which only the background gas is ionised.

3.1 Centroiding

Each ion strike on the detector causes a finite area of the phosphor screen to emit light (Figure 3.1(a)), which triggers a cluster of camera pixels (Figure 3.1(b)). As a result, a single ion strike can be recorded as multiple (x, y, t) coordinates. A pixel is triggered once the signal detected crosses a predefined threshold; pixels closer to the centre of ion impact, for example pixel 1 in Figure 3.1, reach this threshold earlier than those further away, for example pixel 2.

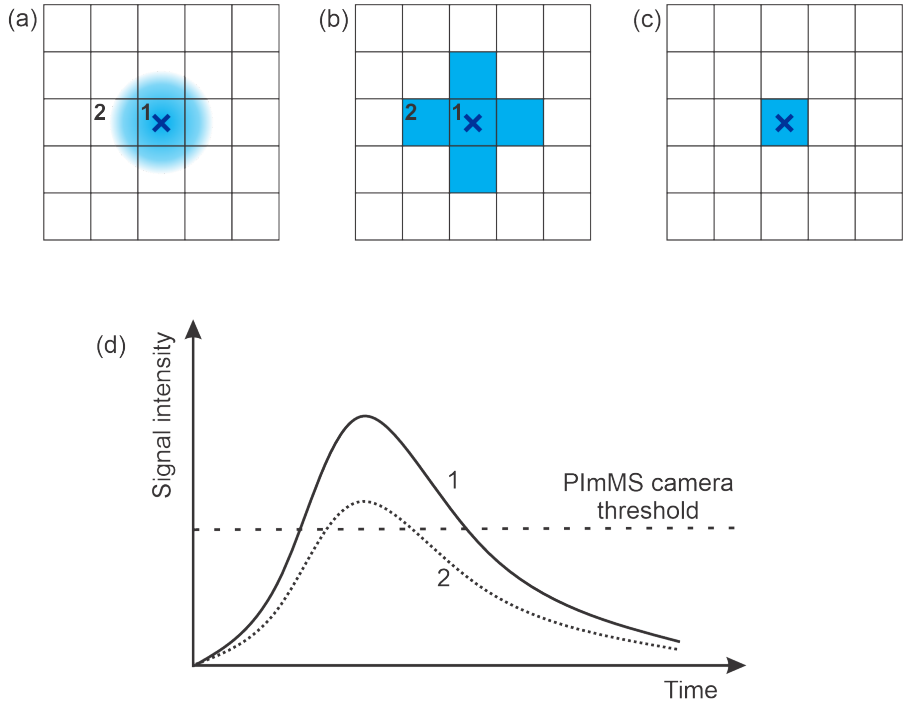


Figure 3.1: A schematic diagram showing how an ion hit is processed by the centroiding algorithm. (a) An ion strikes the detector at the cross, causing light emission from the phosphor screen that illuminates a a section of the PImMS sensor (b) This illumination triggers a cluster of pixels. (c) The centroiding algorithm reduces this cluster to a single pixel, as described in the text. (d) A comparison of the light intensities incident on two labelled pixels within the cluster. Pixels closer to the ion impact experience higher intensity and are triggered earlier.

The centroiding process was first introduced to process 2D ion images by Chang *et al.*[85] They developed an algorithm to reduce each cluster of points down to a single (x, y) coordinate. This method has since been extended to process the t coordinate, so that each cluster is also reduced to a single time code.[86] In this manner, the spatial and temporal resolution of the data set is enhanced and each ion is only counted once.

The centroiding algorithm searches over a spread of time codes when searching for pixel clusters. This time spread needs to be large enough to include all pixels triggered as a result of a single ion hit, but sufficiently narrow to distinguish between clusters resulting from different ion hits. For all of the data presented in this thesis, the time spread was set to 8 time codes. On the basis that the camera cannot be triggered before an ion strikes the detector, the time code for each ion hit is

assigned as the time at which the first pixel in the cluster is triggered.

In order to localise an ion hit to a single pixel, the algorithm calculates the cluster's centre of mass and records the position as the nearest pixel. In the calculation, each pixel is weighted by the reciprocal of the time it is triggered, relative to the first pixel, on the basis that pixels closest to the ion strike's true location will be triggered first:[86]

$$\mathbf{r_c} = \frac{\sum_{i=1}^{N} \mathbf{r_i} t_i^{-1}}{\sum_{i=1}^{N} t_i^{-1}}, \tag{3.1}$$

in which $\mathbf{r_c}$ is the position vector of the centre of mass, $\mathbf{r_i}$ is the position vector of the i^{th} pixel in a cluster. The time code, t_i, is calculated by:

$$t_i = T_i - T_0 + 1, \tag{3.2}$$

where T_i is the time code recorded for the i^{th} pixel and T_0 is the time code when the first pixel in the cluster is registered.

Camera noise, which is characterised by single pixel features in the data set, is eliminated by setting the minimum size of cluster that the algorithm considers as an ion strike to two.

This process will not work if the detector is saturated and different clusters are overlapping, so the conditions of the experiment, in particular the electron and molecular beam intensities, must be chosen appropriately in order to avoid these effects.

3.2 Time-of-Flight spectra and ion images

After centroiding, the first step of analysis is to extract a time-of-flight (ToF) spectrum from the data set, in order to identify the ions produced from their

arrival times. Signal and background spectra are generated by integrating the respective data sets over the x and y spatial coordinates, so that the signal is plotted as a function of arrival time. A background-subtracted spectrum is obtained by subtracting the background spectrum from the signal spectrum, leaving a ToF spectrum of ions produced from the molecule being studied. In order to assign individual peaks, the spectrum must be plotted as a function of ionic mass-to-charge (m/z) by conducting a mass calibration.

As explained in Section 2.4, ions are accelerated by the electric field of the ion lens to a kinetic energy, E_k, which can be expressed in terms of an ion's mass, m, and final velocity, v:

$$E_k = \frac{1}{2}mv^2. \tag{3.3}$$

E_k depends on the accelerating electric field, V, and the ion's charge, z:

$$E_k = \frac{1}{2}mv^2 = zeV. \tag{3.4}$$

By expressing the ion's velocity in terms of the distance the ions must travel to the detector, d, and the time taken to travel to the detector (the time-of-flight), t, Equation 3.4 can be rewritten as follows:

$$\frac{1}{2}m\left(\frac{d}{t}\right)^2 = zeV. \tag{3.5}$$

Rearranging 3.5 for t yields

$$t = d\sqrt{\frac{m}{2zeV}}, \tag{3.6}$$

which simplifies to

$$t = c\sqrt{\frac{m}{z}} \tag{3.7}$$

where $c = \sqrt{\frac{d}{2eV}}$.

The camera does not record an ion's time-of-flight, t, but instead records its arrival time, t_{arr}, which is measured relative to the time at which the camera is triggered, t_0, allowing Equation 3.7 to be rewritten as:

$$t = t_{\text{arr}} - t_0 = c\sqrt{\frac{m}{z}}. \tag{3.8}$$

Therefore, in order to calibrate a spectrum in practice, t_0 and c must be determined by selecting two peaks with known identities, often the parent molecular ion and background H_2O^+ ions. Their t_{arr} and m/z values can be substituted into Equation 3.8 to obtain two equations that are solved simultaneously.

Having obtained an expression for t in terms of an ion's m/z, a Jacobian must be applied to the intensity scale to ensure that the integral of the intensity before and after the unit conversion is the same.

$$\int f(t)dt = \int g\left(\frac{m}{z}\right)d\left(\frac{m}{z}\right) \tag{3.9}$$

Rearranging 3.9 for $g\left(\frac{m}{z}\right)$ yields

$$g\left(\frac{m}{z}\right) = f(t)\frac{dt}{d\left(\frac{m}{z}\right)}. \tag{3.10}$$

By differentiating 3.7, 3.10 can be rewritten as:

$$g\left(\frac{m}{z}\right) = \frac{c}{2}\sqrt{\frac{z}{m}}f(t). \tag{3.11}$$

Finally, Equation 3.7 can be used to rewrite 3.11 in terms of t:

$$g\left(\frac{m}{z}\right) = \frac{c^2}{2t^2} f\left(t\right). \tag{3.12}$$

3.3 Image Inversion

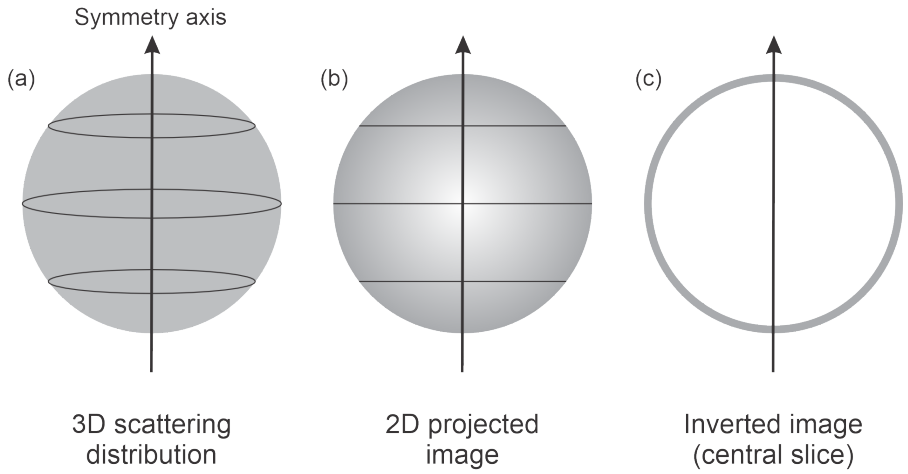


Figure 3.2: Schematic diagrams of (a) a 3D scattering distribution with an axis of cylindrical symmetry, (b) its 2D projection recorded by a crushed velocity-map imaging experiment, and (c) the central slice of the 3D distribution, obtained by Abel inversion of the recorded 2D projection.

Crushed velocity-map imaging compresses ion scattering distributions in the ToF axis, such that a 2D projection of the full 3D scattering distribution is recorded by the camera (Figure 3.2(a) and 3.2(b)). Whilst this helps to ensure that ions with different m/z values are separated in time when arriving at the detector, it means that all information on the product recoil velocity along the ToF axis is lost. As a consequence, an ion whose recoil velocity lies entirely along the ToF axis will strike the centre of the detector and appear indistinguishable from an ion with no recoil velocity.

In order to faithfully extract quantitative information on product velocity distributions, the 3D distribution must be reconstructed first by conducting an image inversion. This recovers the central slice of the full 3D distribution (Figure 3.2(c)).

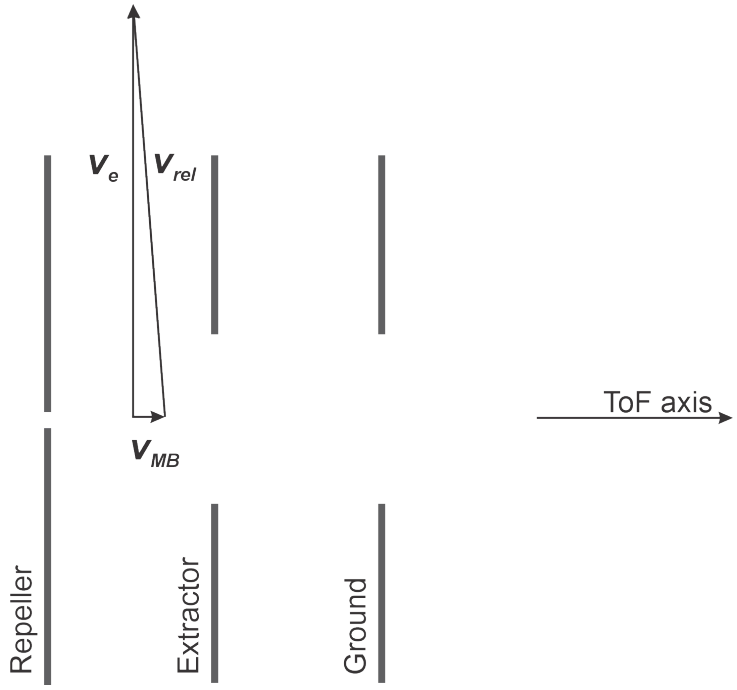


Figure 3.3: A vector diagram for electron-molecule collisions. The electron velocity, $\boldsymbol{v}_\mathbf{e}$ is significantly larger than the molecular beam velocity, $\boldsymbol{v}_\mathbf{MB}$. Therefore, the relative velocity vector can be assumed to lie along the electron beam axis.

Most common inversion methods rely on the scattering distribution possessing an axis of cylindrical symmetry that lies in the plane of the detector. For the electron-molecule crossed beam experiment, the symmetry axis lies along the relative velocity vector, $\boldsymbol{v}_\mathbf{rel}$, of the electron beam, $\boldsymbol{v}_\mathbf{e}$, and the molecular beam, $\boldsymbol{v}_\mathbf{MB}$. As is illustrated in Figure 3.3, $\boldsymbol{v}_\mathbf{e}$ is significantly larger than $\boldsymbol{v}_\mathbf{MB}$, so $\boldsymbol{v}_\mathbf{rel}$ is almost colinear with $\boldsymbol{v}_\mathbf{e}$. For instance, the terminal velocity of a molecular beam is approximately 2000 ms^{-1} and a 50 eV beam of electrons has a velocity of 4.2×10^6 ms^{-1}. In this scenario, the angle between $\boldsymbol{v}_\mathbf{e}$ and $\boldsymbol{v}_\mathbf{rel}$ is 0.03°. Therefore, the electron beam propagation vector is taken as the axis of cylindrical symmetry for all images presented in this thesis.

The most widely-used image inversion techniques are based on the inverse Abel transform.[87] A summary of the derivation of Eppink et al.[57] is provided here. Consider a 3D scattering distribution, $i(x, y, z)$, with an axis of cylindrical symmetry along y. In this scenario, the detector is positioned in the x, y plane

and the ToF axis lies along the z axis. The 2D projection, $p(x, y)$, recorded by the camera is found by integrating over the z axis:

$$p\left(x,y\right)=\int_{-\infty}^{\infty}i(x,y,z)dz. \tag{3.13}$$

Now consider one row of the 2D projected image, $f(x, y_0)$, in the x direction at $y = y_0$, it follows:

$$f\left(x\right)=p\left(x,y_0\right)=\int_{-\infty}^{\infty}s\left(x,z\right)dz=2\int_{0}^{\infty}s\left(x,z\right)dz, \tag{3.14}$$

where $s\left(x,z\right)=i\left(x,y_0,z\right)$ is a slice through the 3D distribution in the x, z plane, perpendicular to the symmetry axis, at $y = y_0$. Given that $i(x, y, z)$ is defined as cylindrically symmetric, $s\left(x,z\right)$ is also necessarily cylindrically symmetric. Therefore, the integrals of $s(x, z)$ over positive and negative z values are equal. To invert a crushed velocity-map image, it is necessary to recover $s\left(x,z\right)$ from $f(x)$.

Cylindrical symmetry allows 3.14 to be written in polar coordinates:

$$f\left(x\right)=2\int_{x}^{\infty}\frac{s\left(r\right)r}{\sqrt{r^2-x^2}}dr, \tag{3.15}$$

where $r^2 = x^2 + y^2$. This integral transform is the forward Abel transform. In order to obtain the inverse Abel transform, and thus recover $s(r)$, the Fourier transform convolution theorem is applied:

$$s\left(r\right)=\frac{1}{\pi}\int_{r}^{\infty}\frac{\frac{df}{dx}}{\sqrt{x^2-r^2}}dx. \tag{3.16}$$

By solving 3.16 for each row of the image, the 3D distribution can be reconstructed.

Analytically solving 3.16 is challenging, due to the singularity at $r^2 = x^2$. Furthermore, the derivative in the integrand amplifies noise in the image. Several methods have been developed to carry out an inverse Abel transform on images

in practice, including the onion peeling algorithm,[57] the Hansen-Law method[88] and basis set expansion methods.[57]

3.3.1 Basis function fitting methods

Basis function fitting methods expand the experimental image, P, over a set of 2D basis functions, $\{f_k\}$ $(k = 0, ..., K-1)$:

$$P = \sum_{k=0}^{K-1} w_k f_k, \tag{3.17}$$

where w_k is the weighting coefficient for the k^{th} basis function. The set of basis functions is selected such that they each have a known inverse Abel function.

In practice, weighting coefficients are determined by minimising the difference between the image, P, and the fit as defined in Equation 3.17. Regularisation techniques can be employed to prevent overfitting of the image data. For example, the Tikhonov method penalises large weighting coefficients by adding a penalty weighting factor.[89]

BASEX method

One of the most commonly-used basis function fitting methods is the Basis Set Expansion (BASEX) method, developed by Dribinski *et al.*.[90] This utilises basis functions of the form:

$$\rho_k(r) = \left(\frac{e}{k^2}\right)^{k^2} \left(\frac{r}{\sigma}\right)^{2k^2} e^{-\left(\frac{r}{\sigma}\right)^2} \tag{3.18}$$

These functions are very similar in form to Gaussian functions. A set of basis functions, $\{f_k(r)\}$, can be obtained by the Forward Abel transform and used to fit the experimental data. The functions themselves can be tailored to the specific data

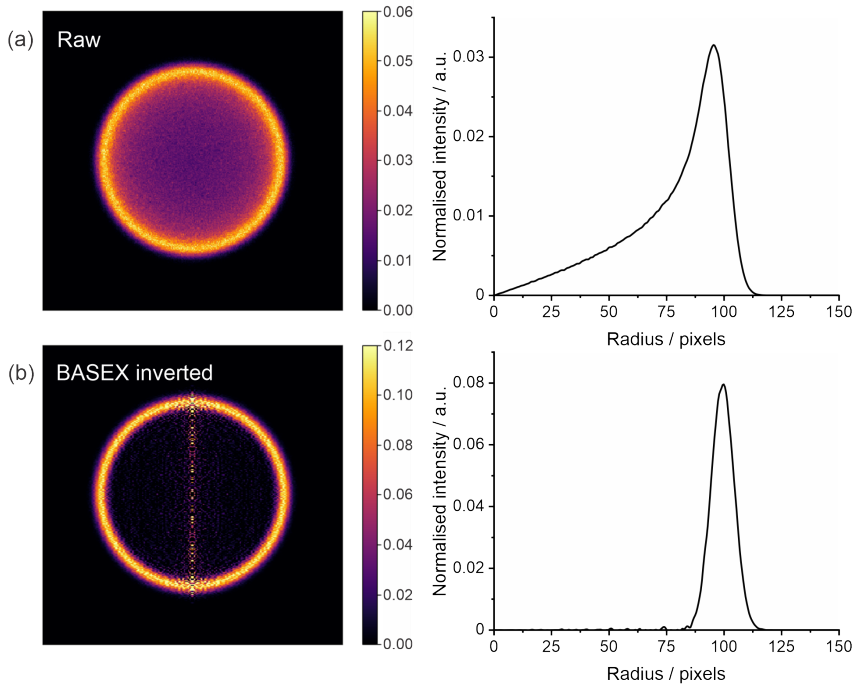


Figure 3.4: A simulated 2D velocity-map image (details in the text) and its corresponding radial distribution are displayed in (a). The inverted image, obtained using the BASEX method with a basis function width of 2 pixels, is displayed in (b) with its corresponding radial distribution.

set; for example, the function width, determined by σ, can be varied to smooth the data as appropriate. BASEX is a Cartesian method, so inverts an image row-by-row.

As an example, the BASEX algorithm is applied to a simulated data set. A scattering distribution of 3,000,000 ions, distributed isotropically on the surface of a sphere, was generated. The radii of the ions were drawn from a Gaussian distribution, with a mean of 100 pixels and a standard deviation of 5 pixels.

Figure 3.4(a) shows the 2D projected image of this scattering distribution and the corresponding radial distribution. Ions with a velocity component in the ToF axis result in the radial distribution tailing to zero. An inverted image, generated by the BASEX method with a function width of 2 pixels, is displayed in Figure 3.4(b). The image takes the form of a ring, which is consistent with taking the central slice through a hollow sphere. The original radial distribution of the simulated

3D scattering distribution is recovered in the radial distribution of the inverted image. Noise is concentrated along the axis of cylindrical symmetry in the inverted image, which is a consequence of the inversion process.

Other basis function fitting methods exist, for example the pBASEX technique,[91] which uses a basis set in polar coordinates. All of these techniques have the advantage of being versatile, since the user can select an appropriate basis set. Additionally, basis functions and their inverses can be stored in advance, so the algorithm is computationally efficient.

3.4 Energy Calibration

Having inverted a velocity-map image, a radial distribution can be obtained by integrating over the angular coordianate of the centred image. However, in order to dissect the dynamics more quantitatively, one must convert the radial distribution (in units of pixels) to a distribution that is physically related to the dissociation dynamics, such as a velocity or kinetic energy distribution. The conversion to kinetic energy scale is summarised here.

The radial coordinate, r, of an ion in the plane of the detector is given by $r = v_\perp t$, where $v_\perp$ is the ion's velocity in the detector plane (perpendicular to the ToF axis) and t is the flight time. Kinetic energy, $E_{k\perp}$, in the detector plane is given by:

$$E_{k\perp} = \frac{1}{2}mv_\perp^2 = \frac{1}{2}m\left(\frac{r}{t}\right)^2. \tag{3.19}$$

Equation 3.19 can be rewritten by substituting Equation 3.6 for the time-of-flight, t:

$$E_k = \frac{zeVr^2}{d^2} = kzr^2, \tag{3.20}$$

where $k = \frac{eV}{d^2}$ is a constant for a particular experiment. In practice, k is determined

from ion trajectory simulations. Trajectories of ions with a range of $E_{k\perp}$ values are calculated using the SIMION software package and the radii at which they strike the detector are recorded, in order to construct a calibration curve.

It is noteworthy that the relationship between the radius at which an ion strikes the detector and its recoil kinetic energy is independent of its mass, m. Assuming no difference in ionic charge, the relationship between E_k and r is determined solely by the experimental setup, for example the flight tube length, d, and the acceleration potential, V. In order to increase the kinetic energy resolution, the flight tube can be extended or the acceleration voltage applied to the ion lens can be decreased, so that the image is expanded on the detector, whilst ensuring that the product ions with the largest kinetic energy releases still strike the detector.

In a similar manner to the mass calibration, a Jacobian must be applied to the radial intensity scale, $f(r)$, to obtain the kinetic energy intensity scale, $g(E_{k\perp})$:

$$g(E_{k\perp}) = f(r) \cdot \frac{dr}{dE_{k\perp}} = \frac{f(r)}{2kzr}. \tag{3.21}$$

3.5 Covariance analysis

Covariance is a statistical measure of how two variables, X and Y are correlated and is defined as follows:

$$Cov\,(X,Y) = \langle (X - \langle X \rangle)\,(Y - \langle Y \rangle) \rangle \tag{3.22}$$

$$= \langle XY \rangle - \langle X \rangle \langle Y \rangle, \tag{3.23}$$

where $\langle ... \rangle$ denotes the mean over all individual measurements. From Equation 3.22, if when X is greater than its mean value, Y also tends to be greater than its mean, and similarly when X is less than its mean, Y also tends to be less than

its mean, $Cov\,(X,Y)$ will be positive. In this scenario, X and Y are said to show positive covariance. $Cov\,(X,Y)$ is negative when the opposite is true, i.e. when X is greater than its mean, Y tends to be less than its mean, and vice-versa. In this scenario, X and Y are said to exhibit negative covariance.

In the field of reaction dynamics, covariance analysis was first applied by Frasinski *et al.* to uncover correlations between ions formed by multiple ionisation and detected by ToF spectrometry.[92] Two product ions exhibit covariance if they are formed in the same fragmentation event, from a common parent. In the context of the electron-molecule crossed beam experiment, where no ionisation step to probe product fragments takes place, this requires the fragmentation of a multiply-charged parent ion. Covariance analysis is blind to products formed from singly-charged parent ions. Given that ions must be formed in the same dissociation event to be correlated, they must be recorded in the same experimental cycle, which requires a multi-mass imaging sensor. Fluctuations in experimental conditions can cause uncorrelated ions that are not formed in the same fragmentation event to exhibit covariance, known as false covariance. This phenomenon and the approaches taken to reduce the contribution of false covariance are explained in Subsection 3.5.2.

Covariance analysis yields information similar to coincidence detection.[93] The difference lies in how the techniques uncover correlations; covariance mapping infers correlations by statistical analysis, whereas coincidence experiments record correlated ions directly. Coincidence detection has found widespread use in studies of photoionisation phenomena. For example, PEPICO (photoelectron-photoion coincidence) detects correlated photoelectrons and photoions.[94] More complex forms include PEPIPICO (photoelectron-photoion-photoion coincidence[95] and PIPICO (photoion-photion coincidence).[96] Under coincidence conditions, experiments are conducted with signal levels that ensure fewer than one event per cycle, so it can

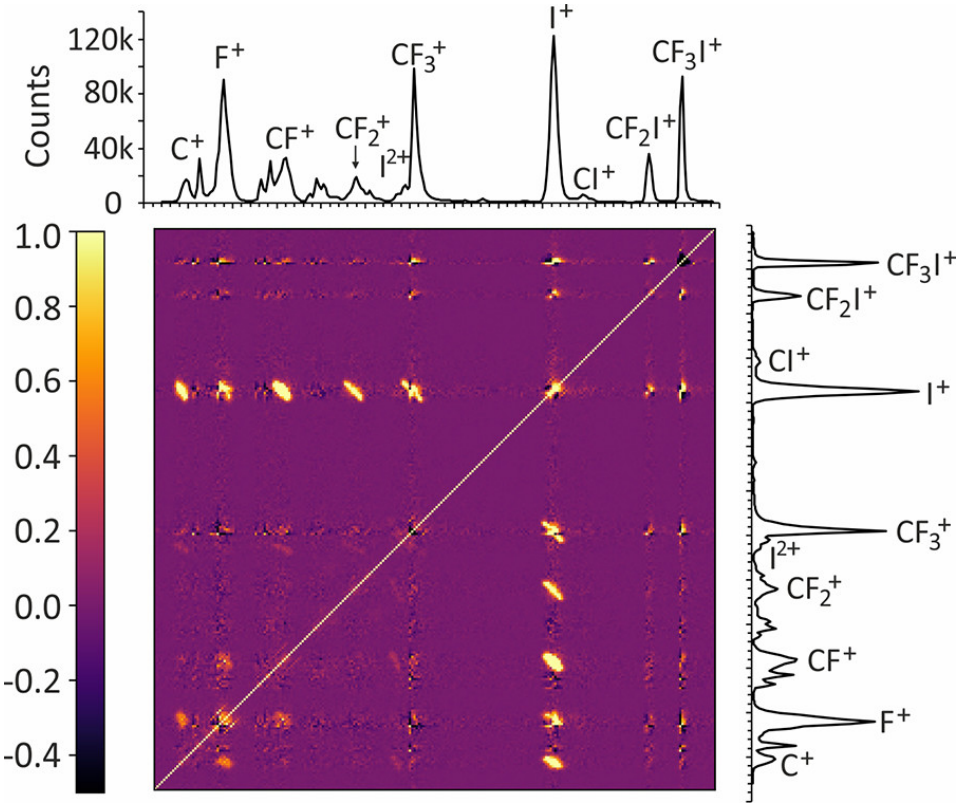


Figure 3.5: Time-of-flight covariance map for the fragment ions produced by the electron ionisation of CF_3I at 100 eV. For reference, the corresponding time-of-flight spectrum is displayed on the top and right-hand axes of the covariance map. Reproduced with permission from Reference [97]. ©American Chemical Society.

be assumed that all products recorded in a particular cycle are correlated. The experiment must be repeated over many cycles to build up a statistical distribution of the correlated observables, which is made practical by conducting experiments at high repetition rates of at least several kilohertz. In contrast, by employing a statistical approach, covariance analysis is able to elucidate correlations from data sets containing multiple events per cycle. Consequently, similar information can often be provided on a significantly shorter experimental timescale.[97]

In the current multi-mass velocity-map imaging setup, two types of covariance analysis are possible: time-of-flight (ToF-ToF covariance); and recoil-frame covariance. Originally introduced by Frasinski *et al.*,[92] the former finds correlations between the arrival times for different ions, so that pairs of correlated products

can be identified. Calculating the covariance between the 1D ToF spectrum and itself generates a 2D ToF-ToF covariance matrix, which can be plotted as a ToF-ToF covariance map. As an illustrative example, Figure 3.5 shows the ToF-ToF covariance map obtained from the electron ionisation of trifluoroiodomethane (CF_3I) at an electron energy of 100 eV, from the work of Köckert *et al.*[97,98] A line of autocovariance of each ion with itself appears along the diagonal of such a map, which is simply the variance of the ToF spectrum. Correlated ion pairs are indicated by off-diagonal areas of positive intensity, known as 'cross peaks'. Generally, cross peaks do not appear as sharp points, but rather as extended features in m/z space that often have a well-defined slope. The slopes of the cross peaks contain information on the mechanism of dissociation and the relative momentum of the correlated fragments. For a more detailed introduction to ToF-ToF covariance and its application to studying dissociative electron ionisation, the reader is directed to the original work by Frasinski *et al.* in Reference [92] and the review article by Vallance and co-workers (Reference [97]).

3.5.1 Recoil-frame covariance

More detailed information on the mechanism and dynamics of a particular dissociation pathway can be extracted from the covariance between the velocities of the two ionic products. The matrix resulting from a covariance calculation between two 2D velocity-map images would be four dimensional. In order to reduce the dimensionality of the problem, and thus make the calculation less computationally expensive and the result more intuitive to visualise, a 2D matrix, which can be plotted as a recoil-frame covariance map, is generated by a series of rotations described below and illustrated in Figure 3.6.

Consider the dissociation of XY^{2+} into X^+ and Y^+. For the purpose of calculating

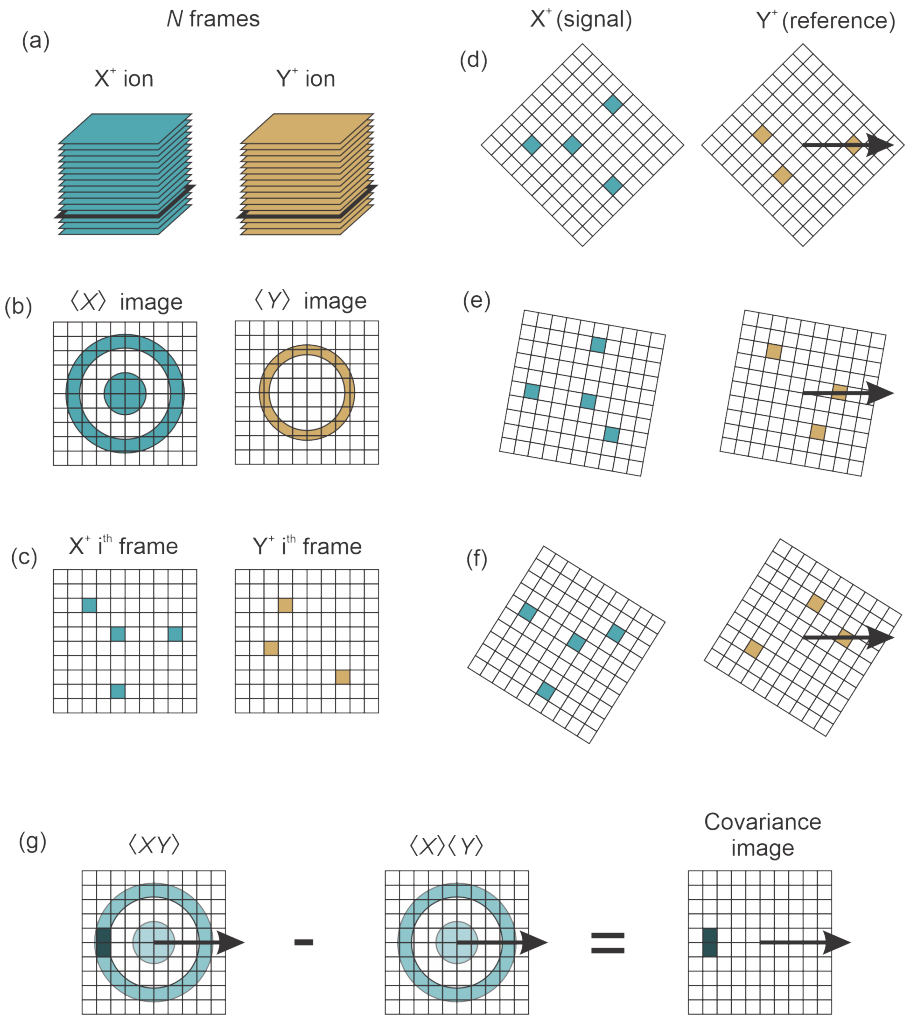


Figure 3.6: An illustration of the process to calculate a recoil-frame covariance for the signal ion X^+ and reference ion Y^+, which are formed in the process $XY^{2+} \rightarrow X^+ + Y^+$. N acquisition cycles of data are recorded (a), from which mean ion images of X^+ and Y^+ can be calculated. X^+ and Y^+ ion images can also be obtained for each acquisition cycle (c). A reference direction is defined and a series of rotations (described in the text) are conducted (d) - (f) to calculate the $\langle XY \rangle$ term. The $\langle X \rangle \langle Y \rangle$ term (described in the text) is subtracted from the $\langle XY \rangle$ term to produce the recoil-frame covariance map (g).

the covariance between two product ions, X^+ is designated as the "signal" ion, and Y^+ as the "reference" ion. The ion images of ion X^+ and ion Y^+ for a given experimental cycle are denoted by X and Y, respectively. From N cycles of experimental data mean ion images, $\langle X \rangle$ and $\langle Y \rangle$ can be obtained for ions X^+ and Y^+, respectively, by summing the X^+ and Y^+ ion hits from all experimental cycles and dividing by N. Generating a recoil-frame covariance map can be considered in two steps:

calculating the $\langle XY \rangle$ term and. the $\langle X \rangle \langle Y \rangle$ term.

Beginning with the former, the algorithm processes the data set cycle-by-cycle. Taking the i^{th} acquisition cycle, ion images are obtained for X^+ and Y^+, as shown in Figure 3.6(c). A reference direction is defined, which by convention in this thesis is to the right, and the reference ion image is rotated so that an ion hit aligns with this direction. The signal ion image is rotated by the same angle, as illustrated in Figure 3.6(d). This procedure is repeated for each reference ion hit within the acquisition cycle and the signal ion images at each orientation are summed. An identical process is followed for each acquisition cycle of data, as in Figures 3.6(e) and 3.6(f). The results are then summed together and divided by N to generate the $\langle XY \rangle$ term, which is illustrated by the left-hand image in 3.6(g). This contains all true covariances, where both the signal and reference ions were formed in the same dissociation event, and all false covariances, where the signal and reference ions originate from different events.

A similar procedure is carried out to generate the $\langle X \rangle \langle Y \rangle$ term. However, rather than iterating through the data set cycle-by-cycle, the mean ion images are processed instead to generate the second image in Figure 3.6(g). Finally, $\langle XY \rangle$ and $\langle X \rangle \langle Y \rangle$ images are subtracted for the recoil-frame, leaving only true covariance intensity.

The recoil-frame covariance image displays the velocity distribution of signal ions relative to the reference ion velocity. For a two-body dissociation, such as the one illustrated, true covariance intensity accumulates opposite the reference direction, since the two fragments recoil in opposite directions by conservation of momentum. False covariance intensity is distributed around the image.

Figure 3.7 shows recoil-frame covariance analysis applied to simulated data. In Figure 3.7(a), AB^{2+} fragments into two product ions, A^+ and B^+, in a two-body dissociation process. For recoil-frame covariance analysis, A^+ and B^+ are designated

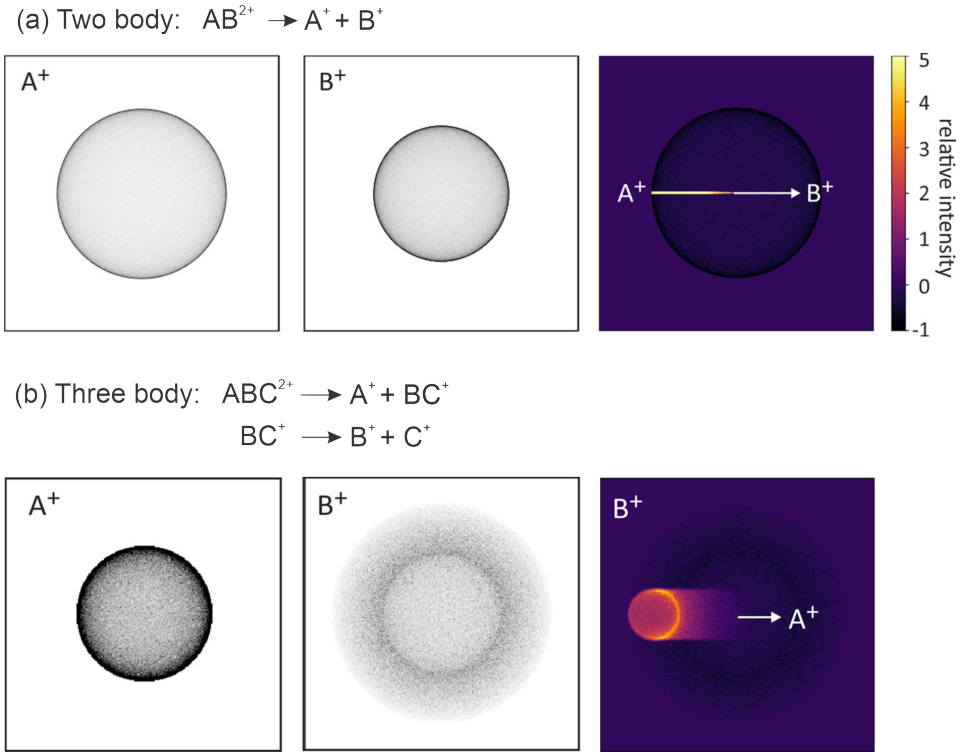


Figure 3.7: (a) Simulated velocity-map images for the two-body dissociation of AB^{2+} to form A^+ and B^+ (left and middle). The corresponding recoil-frame covariance image with B^+ as the reference ion and A^+ as the signal ion. (b) Simulated velocity-map images for A^+ and B^+ formed in a three-body initial charge separation mechanism (left and middle). The corresponding recoil-frame covariance map with A^+ as the reference ion and B^+ as the signal ion is displayed on the right. Figure adapted from Reference [97].

as the signal and reference ions, respectively. Since linear momentum must be conserved, the two fragments recoil in opposite directions. In the recoil-frame covariance map, this manifests as A^+ intensity concentrated at 180° from the reference direction. Instead of being concentrated at one radius, the A^+ intensity forms a tail towards the centre. This feature is a consequence of calculating covariance between two crushed velocity-map images. As a consequence, any velocity distribution extracted from the recoil-frame covariance map is, in fact, a distribution of velocity projected in the detector plane. Abel-inverting the two velocity-map images prior to covariance analysis does not resolve the issue, since all correlation information is lost in the inversion process. Inversion methods for

recoil-frame covariance maps are in development,[99] which will allow true velocity distributions to be faithfully extracted.

More complex, multi-step fragmentation mechanisms can also be elucidated by recoil-frame covariance analysis. Consider a scenario in which ABC^{2+} initially dissociates into A^+ and BC^+. In a second step, BC^+ fragments to form B^+ and a neutral fragment, C. Figure 3.7 (b) shows the recoil-frame covariance map where B^+ is the signal ion and A^+ is the reference ion. The velocity of B^+ is blurred by the second dissociation step, in which C is lost. These simulations were carried out by Dr David Heathcote and originally presented in Reference [97], where further details on the simulation can be found.

3.5.2 Partial and contingent covariance

Fluctuations in experimental parameters, such as the molecular beam density or the electron beam current, during the course of an experiment can cause uncorrelated ions to exhibit covariance. Consider a scenario in which the molecular beam density increases over time. The signal from every product ion would increase, and, as a consequence, correlations would be introduced between all ions. This introduces artifacts to the resulting covariance maps, making them more complicated to interpret. Monitoring these experimental parameters throughout the experiment is possible, but adds significant experimental complexity. However, the total signal level, which can be readily extracted from the data set, is an effective proxy.[100] Two approaches have been developed to reduce the contribution of false covariance: contingent covariance and partial covariance.

Contingent covariance works by ranking each acquisition cycle of data according to the total signal level (i.e. the total number of detected ion counts). The data set is then sorted into groups based on this ranking. Equation 3.23 is then used to

calculate the covariance matrix for each group. Since the experimental fluctuations within each group are smaller than those present in the entire data set, false covariance artifacts are reduced substantially. The results for each group are then summed to produce the final covariance map.[100,101]

Partial covariance, $pCov(X, Y; I)$ employs a modified equation to account for the fluctuating parameter (in this case the total signal level), I:[100–103]

$$pCov\,(X, Y; I) = Cov\,(X, Y) - \frac{Cov\,(X, I)\,Cov\,(Y, I)}{Cov\,(I, I)}. \tag{3.24}$$

Here, the second term works to subtract away the contribution of false covariance. Contingent and partial covariance are both employed in Chapter 7 to dissect the dissociation pathways of multiply-charged polycyclic-aromatic hydrocarbon ions.

3.6 Summary

This chapter has explained the various aspects of data processing and analysis required to extract information on the dissociation dynamics being studied from raw data acquired by the PImMS camera. The following chapters apply these techniques to a series of different chemical systems and different electron energies. Chapter 4 concentrates on the dynamics of dissociative electron ionisation of CF_3I.

4

Electron ionisation of trifluoroiodomethane at low electron energies

Trifluoroiodomethane, CF_3I, has often been used in the field of chemical dynamics as a benchmark system for studying the dynamics of dissociative ionisation in the gas phase.[104,105] Industrially, CF_3I has found application as an environmentally-friendly alternative to conventional fluorocarbon plasma etching gases.[106,107] The relatively weak carbon-iodine bond is chemically more labile than carbon-fluorine bonds. Consequently, the lifetime of atmospheric CF_3I is shorter than traditional fluorocarbon etching gases, so its global warming potential (GWP) is significantly lower.

The dissociative electron ionisation of CF_3I has previously been investigated at electron energies between 20 eV and 100 eV, and several key fragmentation channels of the parent monocation have been identified.[32] CF_3^+ and I fragments are formed by breaking the carbon-iodine bond via a slow, statistical dissociation mechanism, characterised by low product kinetic energy release. Conversely, a carbon-fluorine bond can cleave to form CF_2I^+ in a rapid, direct dissociation. Breaking the carbon-iodine bond to form CF_3 and I^+ was reported to occur via an intermediate mechanism, displaying dynamics between the two previous cases.

Velocity-mapping data showed little dependence on the electron kinetic energy, suggesting that any nascent highly electronically excited cations rapidly relax to low-lying electronic states prior to dissociation.

The fragmentation dynamics of multiply-charged CF_3I cations were examined in a later study by Köckert *et al.*,[98] in which covariance-mapping was used to distinguish individual dissociation mechanisms. The dication and trication were observed to dissociate either via a two-body Coulomb Explosion, or by more complex many-body dissociation channels.

As discussed in Section 1.1.1, electron ionisation is a collisional process and is not constrained by optical selection rules. Therefore, it is often difficult to determine the initial electronic states of the cations. The present work examines the dissociative electron ionisation of CF_3I at electron energies between 12.3 eV and 20 eV, with the aim of determining the contributions of low-lying electronic states of CF_3I^+ to the observed dissociation dynamics. Limiting the study to this energy range greatly reduces the number of electronic states accessible. By increasing the electron energy incrementally, changes in product abundances and scattering distributions can be monitored as each electronic state of the parent cation becomes accessible.

A number of experimental studies dissecting the photoionisation of CF_3I and the photodissociation of CF_3I^+ have been conducted.[104,105,108–110] Unlike electron ionisation, photoionisation is governed by optical selection rules, thereby limiting the transitions possible in these studies. Additionally, since a known quantity of energy is transferred to the system by photoionisation, the electronic states accessed in these studies could be assigned with a high degree of certainty. These photoionisation results provide valuable information on the low-lying electronic states of CF_3I^+ that are populated in these studies. By limiting the present work to electron energies up to 20 eV, it is possible to compare the results presented

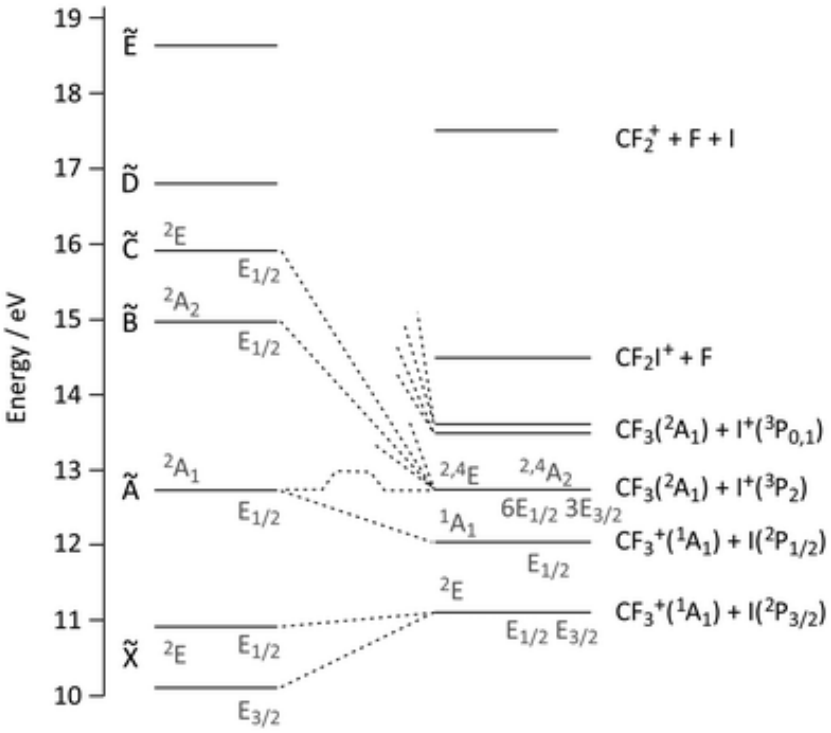


Figure 4.1: Partial correlation diagram for the dissociation of different electronic states of CF_3I^+, for the ground $\tilde{X}$ electronic state to the excited $\tilde{E}$ electronic state. The diagram was constructed based on results from photoionisation studies.[104,105,108–110] Figure reproduced with the permission from Reference [32]. ©Royal Society of Chemistry.

here with the photoionisation studies, which cover a similar range of ionisation energies. Reported results from the photoionisation studies were used by Köckert *et al.* to construct a partial correlation diagram,[32] reproduced in Figure 4.1, for the dissociation of CF_3I^+ from different initial electronic states.

All data presented here were acquired on an electron-molecule crossed beam apparatus, described in detail in Chapter 2. The sample gas mixture is prepared with CF_3I (Apollo Scientific) (20 % partial pressure) and Helium (BOC). Velocity-map imaging data were acquired for a series of electron energies between 12.3 eV and 20 eV. Time-of-flight mass spectra were recorded at each electron energy under spatial-mapping conditions, so that ions were mapped onto the detector according to the position at which they were formed in the interaction region.

In this way, each product ion is detected with the same probability, regardless of its velocity. Each data set was background-subtracted, in order to minimise the effect of background atmospheric gas present in the vacuum chamber on data analysis. To this end, a background data set was acquired at each electron energy, for which the electron beam pulse was triggered to cross the interaction region before the molecular beam pulse arrived.

4.1 Data processing and image denoising

Ion imaging data sets, consisting of an accumulation of discrete ion strikes, are inherently susceptible to Poissonian noise. For example, MCP dark counts and cosmic rays can trigger MCPs even when an ion has not struck the detector. In scenarios where the signal levels for the processes under study are high, this phenomenon does not present a significant issue, since a sufficient number of ion strikes can be recorded readily to construct a statistical distribution. However, when the signal levels are low, Poissonian noise can compromise the analysis and interpretation of scattering distributions. This is particularly the case for dissociative electron ionisation experiments at low electron energies. A molecule's ionisation cross-section is lowest at electron energies close to its ionisation threshold, so product ion count rates are low.

In order to circumvent these issues, images in this Chapter have been 'denoised' after centroiding. In collaboration with the group of Professor Dave Townsend (Heriot-Watt University), an autoencoder artificial neural network (ANN) was employed to recognise the dominant structural features of input raw images and reconstruct only these features. This technique was introduced by Sparling *et al.*,[111] and has been demonstrated in the processing of photoelectron imaging data sets.[111] The ANN is first trained by showing it a set of simulated images, consisting of

pairs of noisy and corresponding noise-free 'truth' images.

In order to generate a set of training images, a general mathematical form of velocity-map images is invoked, and a set of N images is generated; each image is constructed as a series of concentric Gaussian annular structures, each with a randomly selected radius, width and angular distribution (Figure 4.2 (a)). All raw images acquired in our experimental data set were found to have isotropic angular distributions. Therefore, only isotropic annular structures are included in the simulated images. At this point, the simulated images represent a 2D slice through the cylindrically symmetric 3D product scattering distribution. A forward Abel transform is applied to each simulated image to convert these into the 2D projections of the scattering distribution that are recorded in the experiments (Figure 4.2 (b)). Each image is then subjected to a Poisson noise filter to generate a corresponding noisy image (Figure 4.2 (c)). Since the images being processed are isotropic, all of the required information is contained within one quadrant of each image. Therefore, only one quadrant of each image needs to be presented to the neural network (Figure 4.2 (d)). Care must be taken to ensure that images are faithfully denoised by the neural network and that 'real' features are not discarded. To this end, the set of training images is tailored to the dataset that is to be denoised. In particular, the noise level applied to the noisy images of the training set is adjusted to replicate the level of noise (i.e. the average number of counts per pixel) found in the experimentally obtained images. A more complete description of the neural network and training procedure can be found in Reference [111].

As a demonstration of the ANN's use to denoise the images of this CF_3I data set, Figure 4.3 shows the symmetrised image and corresponding radial distribution of CF_2I^+, acquired at an electron energy of 16 eV, before and after denoising. It is clear that the major feature of the central disc is reconstructed, but the noise at higher

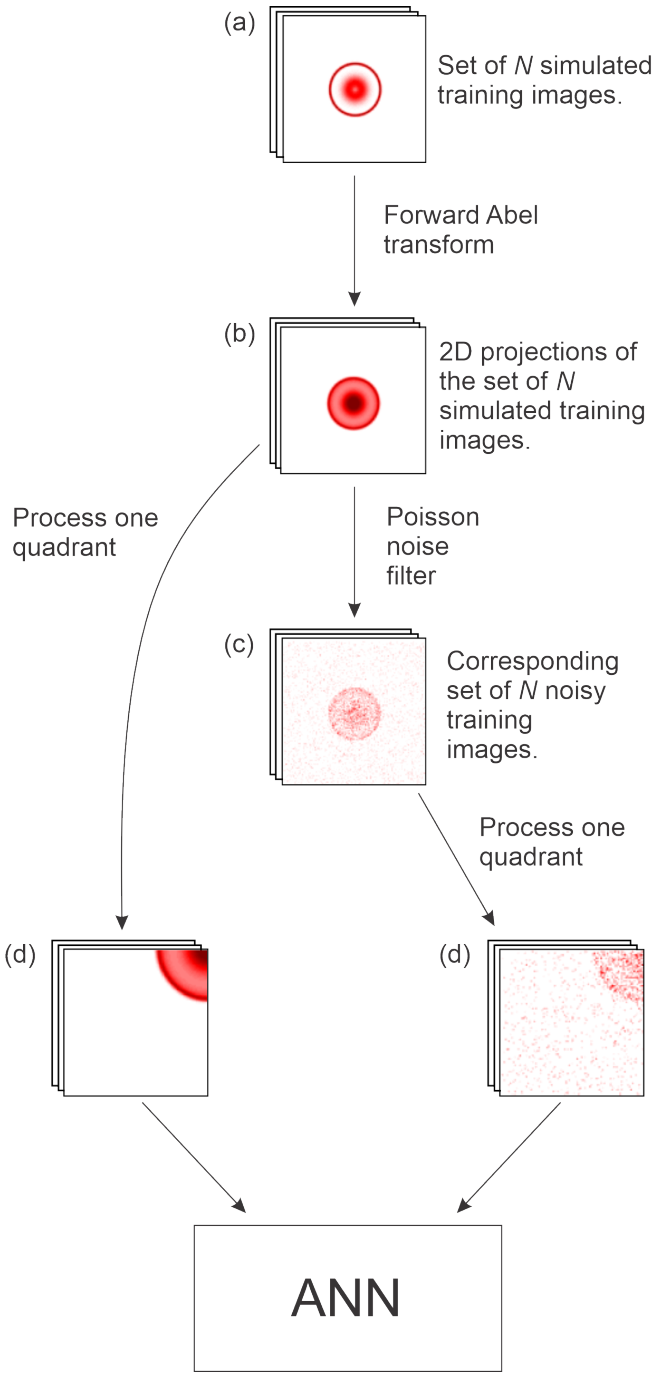


Figure 4.2: Schematic of the process used to generate a set of N images to train an artificial neural network to denoise velocity-map images. A description of each image in the schematic is contained within the text.

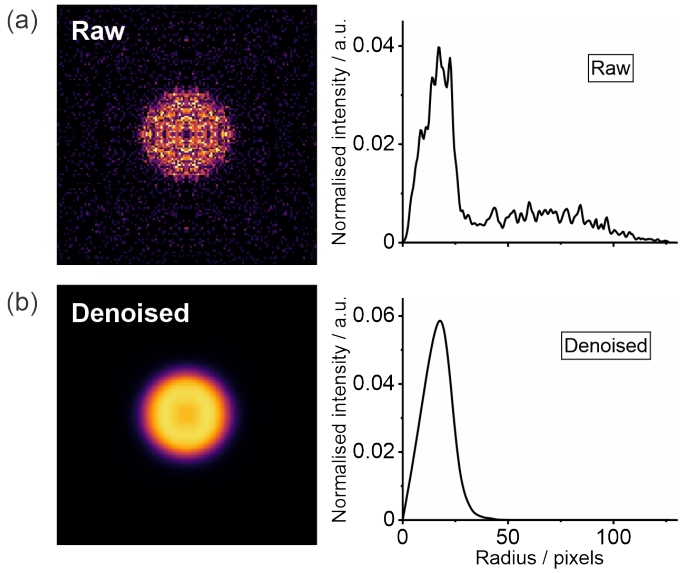


Figure 4.3: (a) Symmetrised raw image of CF_2I^+ formed by the electron ionisation of CF_3I at an electron energy of 16 eV, and its radial distribution. (b) The corresponding image and radial distribution after denoising by the artificial neural network.

radius, which manifests as a noisy baseline in the radial distribution, is excluded.

This baseline feature in the distribution can be attributed to noise rather than signal, based on comparison with previously reported VMI data for the electron ionisation of CF_3I at 100 eV.[32] The 100 eV data set benefits from a significantly higher signal-to-noise ratio than the present data, and no corresponding feature is observed in this range of radii in the CF_2I^+ image. Since all dissociation channels accessible at 16 eV remain open at 100 eV, any features arising from these channels would also be evident in the 100 eV velocity-map image. Therefore, it can be concluded that this baseline feature does not arise from the dissociation of CF_3I^+.

Once an image has been denoised, it can be inverted as normal by the methods described in Section 3.3 and analysed to obtain information on dissociation dynamics. All images presented and analysed in this chapter have been denoised. An error analysis (detailed in Appendix A) indicates a typical uncertainty in the kinetic energy distributions extracted from the denoised images of around 12 %. However, the percentage uncertainty increases markedly for the sections of radial distributions

in which the intensity is low.

4.2 Computational methods

In order to aid interpretation of the experimental data, potential energy curves (PESs) along the carbon-iodine bond coordinate in the CF_3I^+ cation were calculated. One-dimensional energy scans were performed by evaluating the system's potential energy at a series of carbon-iodine distances for the seven lowest-lying doublet electronic states of the CF_3I^+ parent cation. All PES calculations were carried out using the OpenMolcas (v22.10) software package.

The Complete Active Space Self-Consistent Field (CASSCF) method is a multiconfigurational quantum chemistry approach for situations in which a single electronic configuration is insufficient, such as during bond breaking, when considering systems in electronically excited states, or when describing transition metal complexes.[112] In CASSCF, molecular orbitals are partitioned into inactive orbitals, which remain doubly occupied; active orbitals, among which electrons can freely distributed; and virtual orbitals, which remain unoccupied. The user defines an active space of n electrons and m orbitals, denoted as CASSCF(n, m). All possible electronic configurations within this active space are considered, and both the configuration interaction coefficients and the molecular orbitals are optimised to minimise the total energy. Dynamic electron correlation can subsequently be included by applying second-order perturbation theory to the CASSCF wavefunction, a technique known as CASPT2.[113]

For the present study, a CASSCF(11,7) active space was employed for the carbon-iodine bond scans. This active space comprises the carbon-iodine σ bonding and anti-bonding orbitals, two iodine 5p lone-pair orbitals, and three fluorine 2p lone-pair orbitals. Figure 4.4 illustrates the energetic ordering of the active orbitals

in the Franck-Condon region. In the neutral CF_3I, the iodine 5p lone pair is the highest occupied molecular orbital (HOMO) and the carbon-iodine σ anti-bonding orbital is the lowest unoccupied molecular orbital (LUMO). Therefore,the chosen active space spans the six highest occupied orbitals and the lowest unoccupied orbital in the Franck–Condon region.

Two distinct carbon–iodine dissociation pathways were considered:

$$CF_3I^+ \longrightarrow {CF_3}^+ + I \tag{4.1}$$

$$CF_3I^+ \longrightarrow CF_3 + I^+ \tag{4.2}$$

These reaction channels result in different product geometries: CF_3 adopts a pyramidal structure, whereas ${CF_3}^+$ is planar. Accordingly, separate carbon-iodine bond scans were performed for each pathway. In both cases, the initial geometry of the parent cation was taken to be that of the neutral CF_3I molecule, consistent with the Franck–Condon principle.

The equilibrium geometry of neutral CF_3I was optimised at the CASSCF(12,7) level of theory, using the same set of active orbitals shown in Figure 4.4. Bond scans were conducted to a maximum carbon-iodine separation of 4.5 Å. Final product structures were optimised at the CASSCF(11,7) level in the C_1 point group, using the ANO-R1 basis set. During these optimisations, the carbon-iodine distance was held fixed while all other molecular coordinates were allowed to relax. An initial geometry in which the CF_3 moiety was planar converged to the ${CF_3}^+ + I$ products, whereas a pyramidal CF_3 starting geometry converged to the $CF_3 + I^+$ products. In this manner, two sets of final geometries were generated. Intermediate geometries along each dissociation coordinate were generated by linear interpolation of atomic coordinates between the initial and final structures,

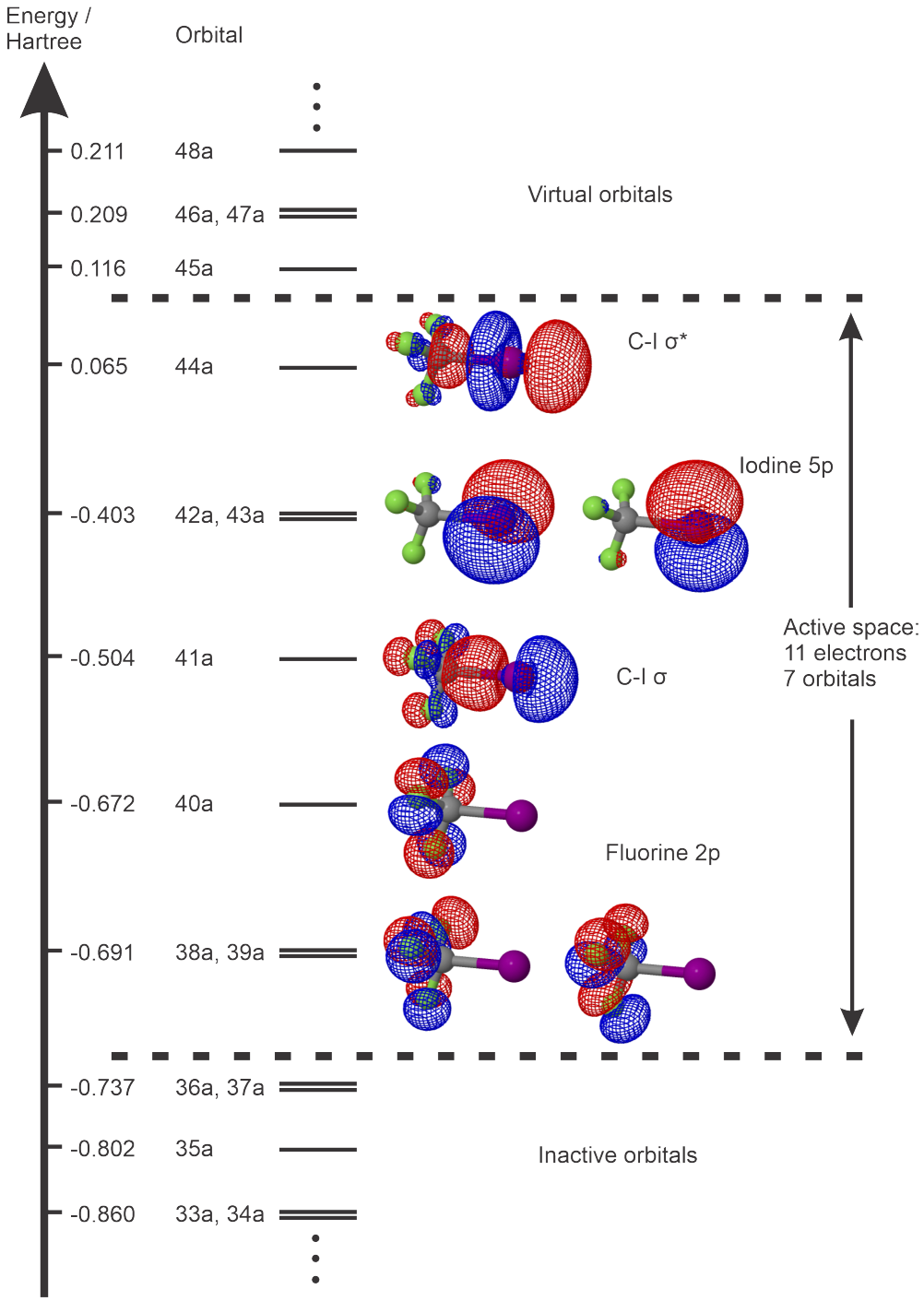


Figure 4.4: Schematic diagram of the CASSCF active space used to calculate potential energy curves along the carbon-iodine bond elongation coordinate in CF_3I^+.

resulting in 39 geometries per scan.

For each geometry, single-point energy calculations were performed for the seven lowest electronic states at the state-averaged CASSCF level (SA(7)-CASSCF(11,7)), using the ANO-R2 basis set. State averaging was performed over these seven electronic states. The optimised wavefunction from each geometry was used as the initial guess for the subsequent point along the scan. At each step, the converged CASSCF wavefunction served as the reference for an extended multi-state CASPT2 (XMS-CASPT2) calculation, using an imaginary shift of 0.2. Spin-orbit coupling was subsequently applied to the XMS-CASPT2 results, in order to obtain the final energies.

The resulting potential energy surfaces are shown in Figure 4.5. In order to validate the calculations, vertical ionisation energies of CF_3I were also calculated, using the ionisation potential variant of the equation-of-motion coupled cluster singles and doubles method (EOM-IP-CCSD) with an ANO-RCC-VDZP basis set. This method is well-suited for evaluating the ionisation potentials of cationic states.[114] Further details on this comparison can be found in Table A.1 in the Appendix A.

4.3 Time-of-flight mass spectra

Mass spectra recorded at electron energies of 13 eV, 16 eV and 20 eV are displayed in Figure 4.6. These reveal the identities and abundances of the ionic fragments at each electron energy. At the ionisation threshold (10.28 eV[115]), only the parent CF_3I^+ cation ($m/z = 196$) can be formed. As the electron energy increases, fragment ions appear in the mass spectrum as dissociation channels become energetically accessible.

In addition to the parent cation, the $CF_3{}^+$ ion ($m/z = 69$) is abundant at all electron energies measured. This is the dominant product ion, formed by carbon-

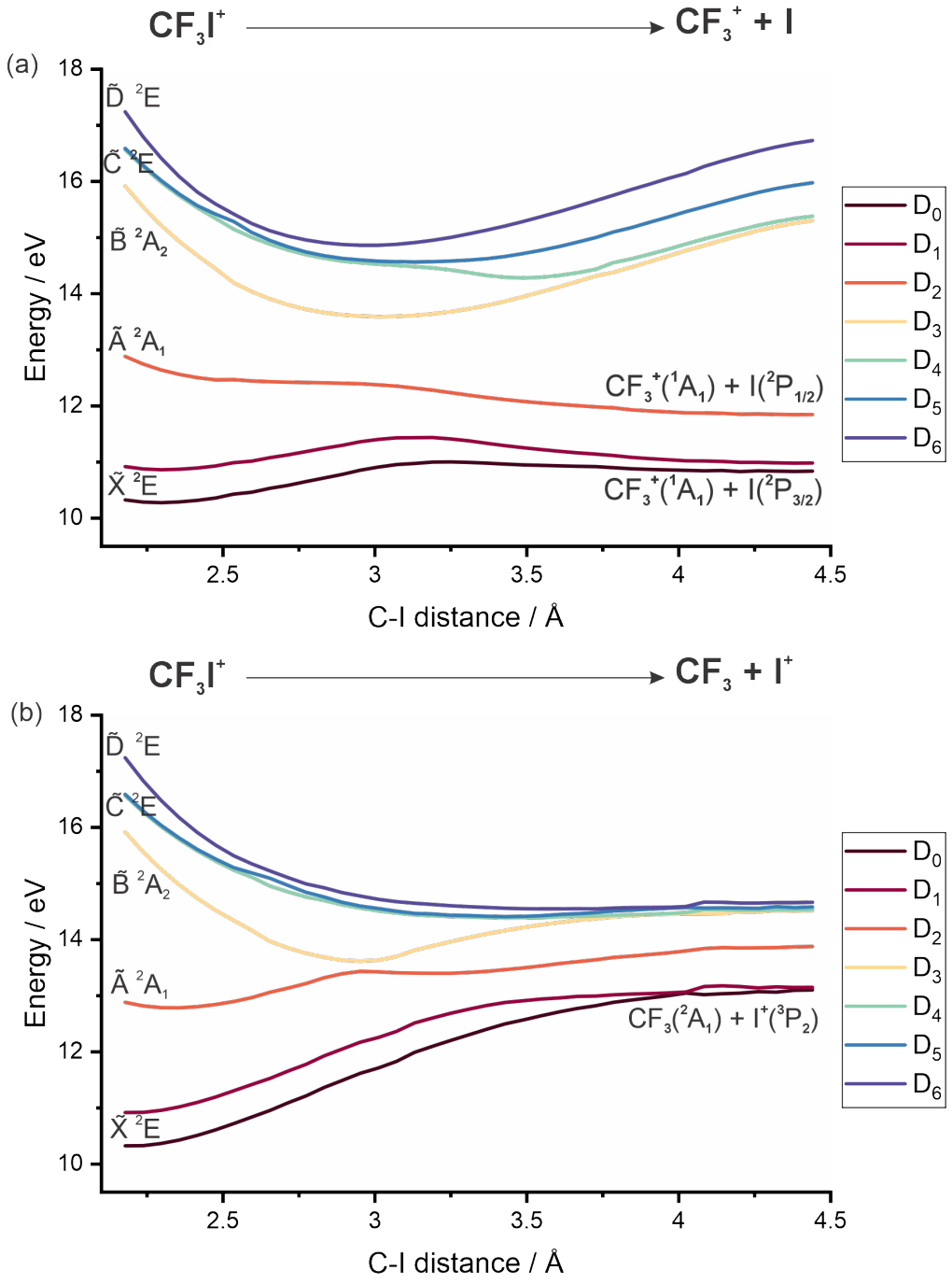


Figure 4.5: Potential energy curves for the seven lowest-lying doublet states of CF_3I^+ along the carbon-iodine bond coordinate to produce (a) $CF_3^+ + I$, and (b) $CF_3 + I^+$. The curves are calculated at the CASSCF(11,7)/CASPT2 level of theory, using an ANO-R2 basis set, as explained in the text.

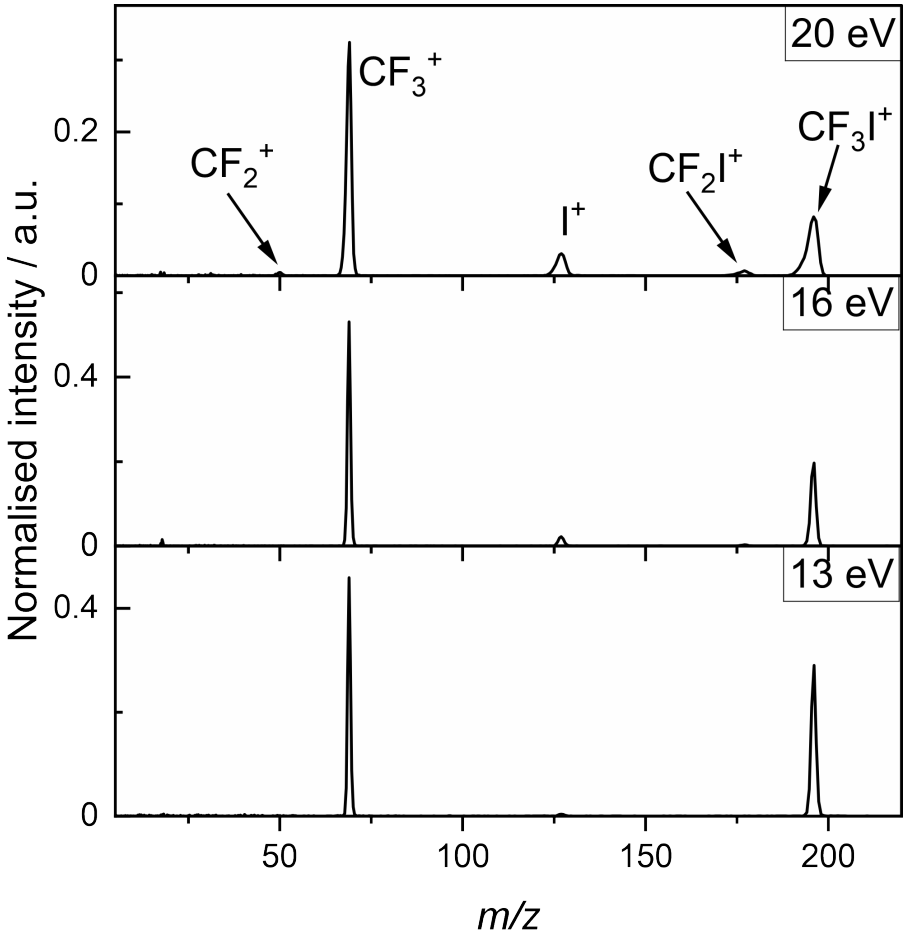


Figure 4.6: Background-subtracted mass spectra of CF_3I at electron energies of 13, 16 and 20 eV.

iodine bond cleavage. At 13 eV, the I^+ fragment ($m/z = 127$) appears in the spectrum and becomes more intense as the electron energy increases. The CF_2I^+ ion ($m/z = 177$), formed by breaking a C-F bond, is first observed at 16 eV. The branching ratio of this channel remains low at higher electron energies, reflecting the strength of the C-F bond compared to the C-I bond. A minor peak at $m/z = 50$, corresponding to $CF_2{}^+$, is also apparent at 20 eV. The carbon-iodine bond and one carbon-fluorine bond must be broken to form this ion, explaining its low abundance.

The dissociation channels observed in this electron energy range are summarised as follows:

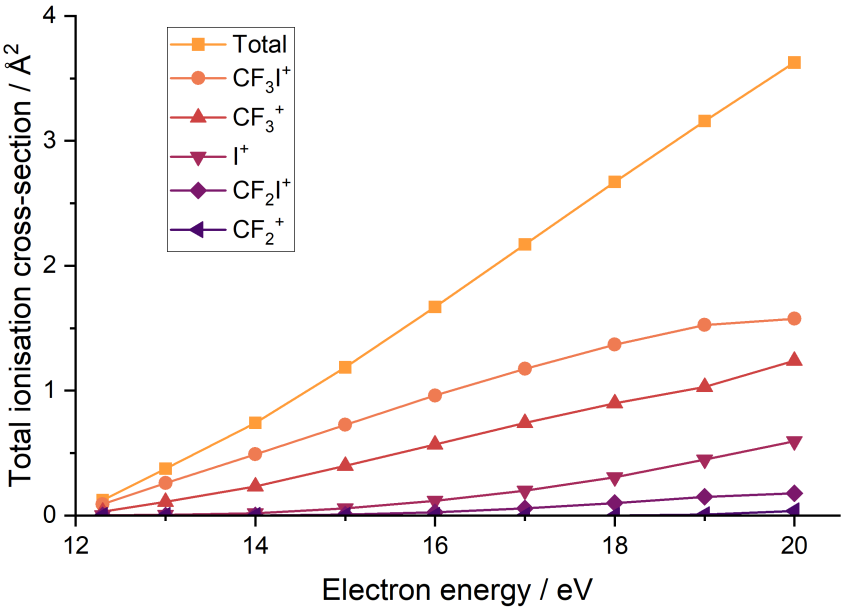


Figure 4.7: The partial cross-section for the formation of each fragment ion plotted as a function of electron energy. Total ionisation cross-sections have been measured by Verma *et al.*[116]

$$CF_3I^+ \longrightarrow CF_3^+ + I \tag{4.3}$$

$$CF_3I^+ \longrightarrow CF_3 + I^+ \tag{4.4}$$

$$CF_3I^+ \longrightarrow CF_2I^+ + F \tag{4.5}$$

$$CF_3I^+ \longrightarrow CF_2^+ + F + I \tag{4.6}$$

In order to determine the partial ionisation cross-sections for each ion in the mass spectrum at a particular electron energy, the area under the corresponding mass peak must first be calculated. From this, a relative branching ratio for each ion is obtained. Given that the partial cross-sections of all of the ions present in the mass spectrum sum to the total ionisation cross-section at that electron energy, the total ionisation cross-section can be used to scale the relative branching ratios to convert them into absolute partial ionisation cross-sections. This process

m/z	Ion	Appearance potential / eV
50	CF_2^+	18.5 ± 0.6[117,118]
69	CF_3^+	11.26 ± 0.05[119]
127	I^+	13.4 ± 0.1[118]
177	CF_2I^+	15.3 ± 0.3[117,118]
196	CF_3I^+	10.28 ± 0.07[115]

Table 4.1: Ions present in the mass spectra of CF_3I over the energy range under study, tabulated with their literature appearance potentials.

can be repeated over a range of electron energies to obtain a plot of the type displayed in Figure 4.7, which shows the partial ionisation cross-section of each fragment as a function of electron energy.

4.4 Velocity-Map Images

Having established which dissociation channels are accessible at electron energies up to 20 eV, velocity-mapping data are now discussed. Sufficient statistics were acquired to denoise and analyse images for the CF_3^+, I^+ and CF_2I^+ product ions. All of these ions are produced via two-body dissociation processes, in which cleavage of one bond yields two fragments. Although only one fragment is charged and detected directly, radial distributions extracted from inverted velocity-map images are converted to total kinetic energy release (TKER) distributions for both fragments by invoking the conservation of momentum, in a manner described in Section 1.3. In the discussion that follows, the dynamics of carbon-iodine and carbon-fluorine bond breaking are characterised through analysis of ion TKER distributions at different electron energies. Carbon-iodine bond dissociation is discussed first, beginning with the CF_3^+ fragment.

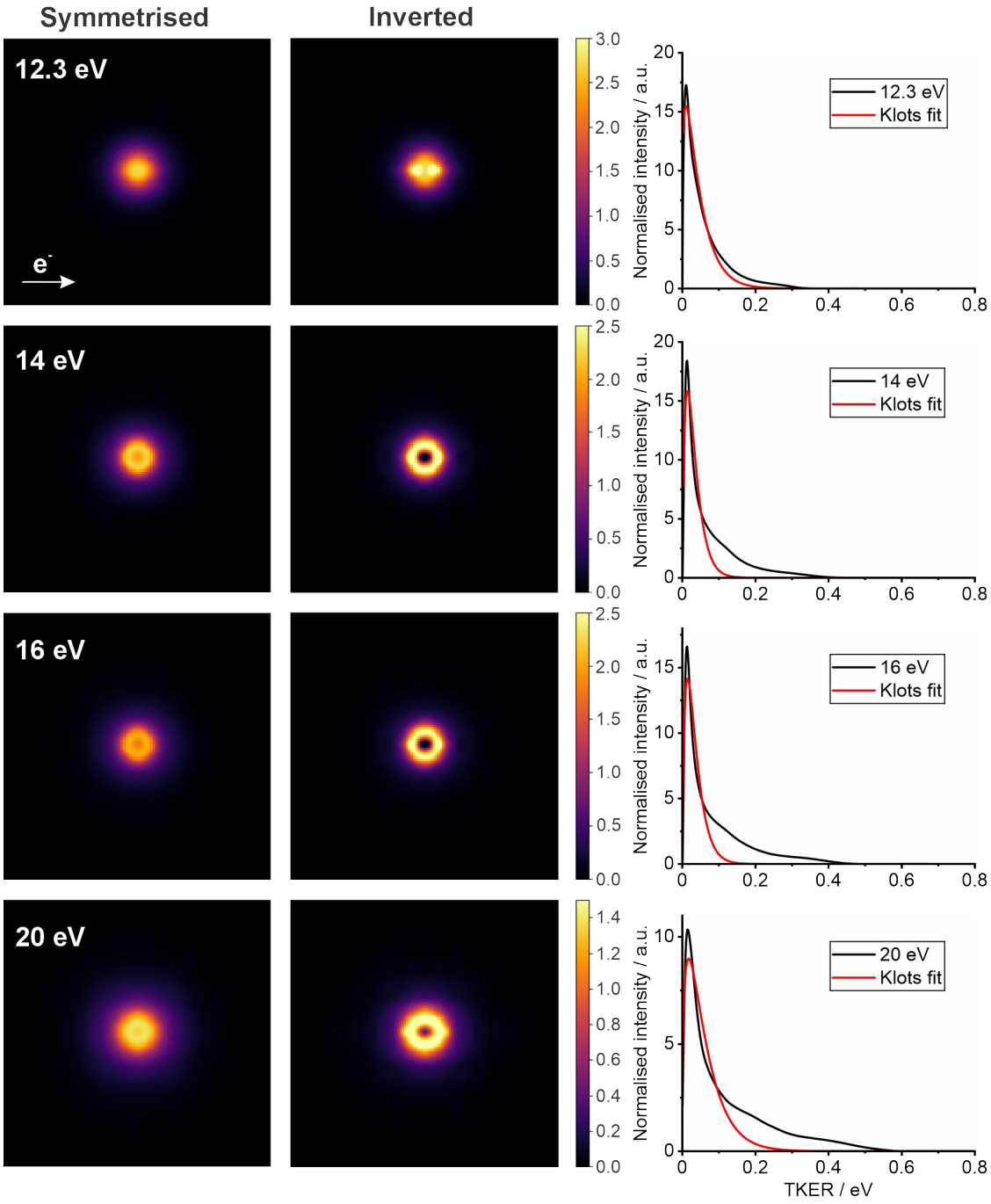


Figure 4.8: Symmetrised velocity-map images, Abel-inverted images and TKER distributions for the CF_3^+ fragment from the dissociative ionisation of CF_3I. The images are shown for electron energies of 12.3 and 20 eV. The TKER distributions have been fitted using Klots' approach.[120]

4.4.1 Carbon-iodine bond breaking

Intensity in the CF_3^+ images recorded between 12.3 eV and 20 eV is concentrated close to the image centre, indicating that CF_3^+ fragments are formed with very little kinetic energy release. The corresponding TKER distributions peak close to zero and are characteristic of a statistical dissociation process. In such a mechanism, the parent cation survives for a sufficiently long time to allow redistribution of energy among the internal vibrational modes of the molecule. Bond dissociation occurs only once enough energy has accumulated in the vibrational mode associated with breaking the carbon–iodine bond.

Statistical TKER distributions, $p(E_\mathrm{T})$, can be fitted by the Klots model free approach:[120,121]

$$p(E_\mathrm{T}) = E_\mathrm{T}^l \exp\left(-\frac{E_\mathrm{T}}{k_\mathrm{B}T^\ddagger}\right), \tag{4.7}$$

where E_T is the TKER of the fragments. The fitting parameter l ranges between 0 and 1; higher values are typical of processes with large centrifugal barriers, whereas smaller values indicate a lower centrifugal barrier. The transition state temperature, $T^\ddagger$, is defined by the average total kinetic energy of the fragments when passing through the transition state. The Boltzmann constant is denoted by k_B. A key advantage of this approach is that it does not require prior knowledge of the interaction potential between the dissociating fragments. However, the fact that this approach does not rely on potential energy surfaces means that it does not fully capture how the shape of the potential energy landscape affects the kinetic energy distribution, particularly after the barrier.

At an electron energy of 12.3 eV, the Klots model free approach fits the TKER distribution well, yielding a $T^\ddagger$ value of 407 K. At this electron energy, only the

$\tilde{X}$ (^2E) ground state of the parent cation is energetically accessible. The partial correlation diagram shown in Figure 4.1 indicates that the $CF_3^+(^1A_1)$ + $I(^2P_{3/2})$ dissociation limit lies above the $\tilde{X}$ state of CF_3I^+ in the Franck-Condon region. Furthermore, the $\tilde{X}$ state potential energy curve in Figure 4.5 (a) shows a barrier to dissociation. Both are consistent with a statistical dissociation mechanism proceeding via vibrationally excited levels of the ground $\tilde{X}$ electronic state of the cation.

At electron energies of 14 eV and above, a shoulder extending to higher TKER becomes evident in the distributions, reaching out to approximately 0.6 eV at an electron energy of 20 eV. The Klots model fails to fit this shoulder adequately, suggesting that the mechanism can no longer be described as entirely statistical. Downie and Powis found that the TKER distribution resulting from CF_3^+ formation on the $\tilde{A}$ ($^2A_1$) state of the CF_3I^+ cation, following ionisation by 13.3 eV photons, peaks at 0.2 eV and extends 0.6 eV.[104] In light of these reported findings, it is highly likely that a direct, impulsive dissociation mechanism on the $\tilde{A}$ state of the parent cation occurs at electron energies of 13 eV and above, in addition to the statistical mechanism on the $\tilde{X}$ state.

The calculated potential energy surface for the $\tilde{A}$ state of CF_3I^+ displayed in Figure 4.5 (a) is repulsive. The energy difference between the $\tilde{A}$ ($^2A_1$) electronic state at the Franck-Condon geometry and the $CF_3^+(^1A_1)$ + $I(^2P_{1/2})$ dissociation limit is approximately 1.0 eV. Comparing this to the observed $\tilde{A}$ state TKER suggests that a significant fraction of the available energy is partitioned into internal excitation of the fragments, most likely as vibrational excitation of the CF_3^+ fragment.

I^+ velocity-map images recorded at electron energies of 14, 15, 17 and 20 eV are displayed in Figure 4.9. In contrast to CF_3^+, all TKER distributions peak away from zero, indicating that a statistical fragmentation mechanism contributes little to I^+ formation. In order to assess how the kinetic energy release varies with

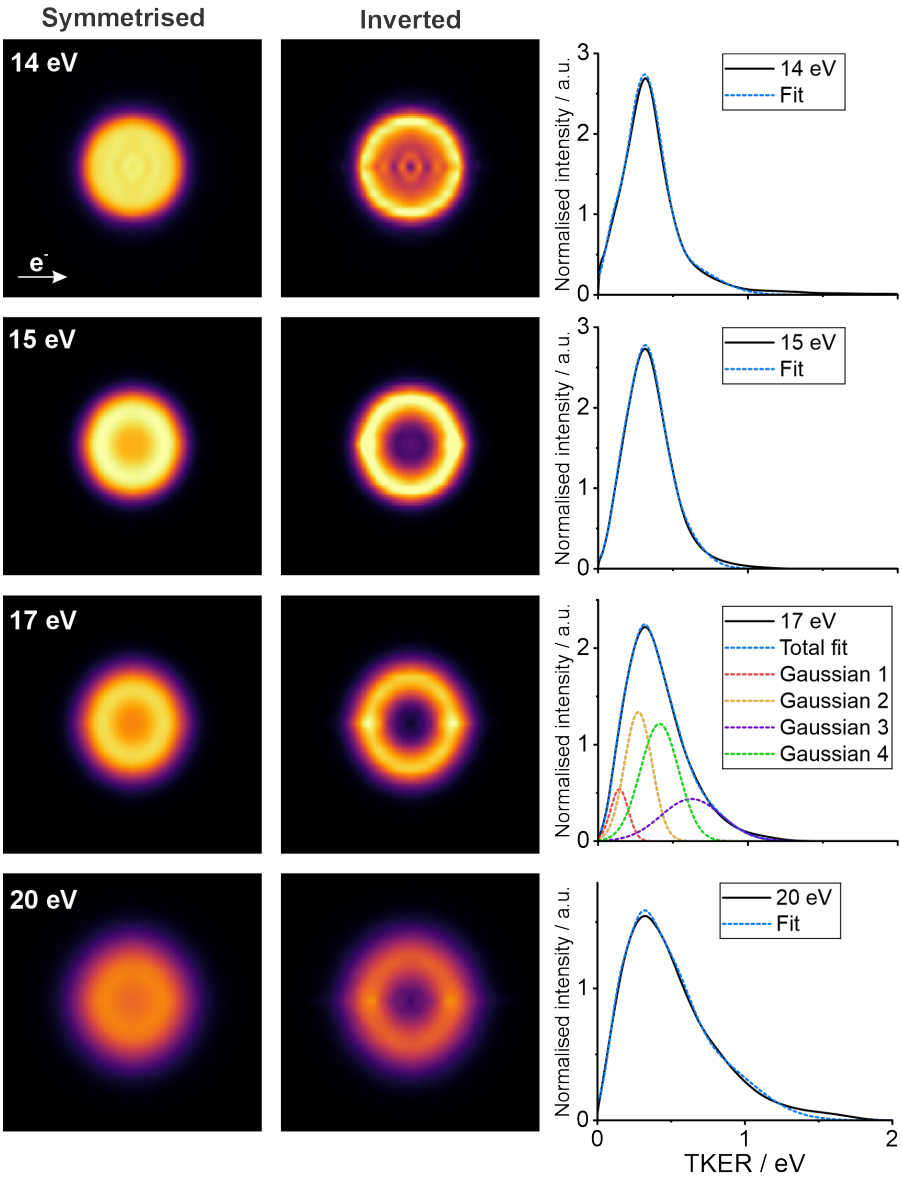


Figure 4.9: Symmetrised velocity-map images, Abel-inverted images and TKER distributions for the I^+ fragment from the dissociative ionisation of CF_3I. The images are shown for electron energies of 13, 15, 17 and 20 eV. The TKER distributions have been fitted using one or more Gaussian functions. See the text for details.

Electron energy / eV	Gaussian 1	Gaussian 2	Gaussian 3	Gaussian 4
14	$A = 0.06$ $\mu = 0.10$ $\sigma = 0.05$	$A = 0.73$ $\mu = 0.31$ $\sigma = 0.12$	$A = 0.21$ $\mu = 0.54$ $\sigma = 0.22$	-
15	$A = 0.06$ $\mu = 0.14$ $\sigma = 0.06$	$A = 0.66$ $\mu = 0.30$ $\sigma = 0.11$	$A = 0.28$ $\mu = 0.47$ $\sigma = 0.16$	-
17	$A = 0.08$ $\mu = 0.14$ $\sigma = 0.06$	$A = 0.31$ $\mu = 0.27$ $\sigma = 0.09$	$A = 0.39$ $\mu = 0.41$ $\sigma = 0.13$	$A = 0.22$ $\mu = 0.62$ $\sigma = 0.20$
20	$A = 0.06$ $\mu = 0.13$ $\sigma = 0.06$	$A = 0.22$ $\mu = 0.26$ $\sigma = 0.11$	$A = 0.39$ $\mu = 0.45$ $\sigma = 0.17$	$A = 0.34$ $\mu = 0.75$ $\sigma = 0.30$

Table 4.2: Parameters obtained from fitting the TKER distributions of the I^+ fragment at electron energies of 14, 15, 17 and 20 eV. The mean TKER, μ, standard deviation, σ and area under the curve, A, of each Gaussian component function are tabulated.

electron energy and to identify which electronic states of the parent contribute to dissociation, a linear combination of Gaussian functions has been fitted to the TKER distributions in Figure 4.9. An attempt was made to allow for a statistical dissociation mechanism by including Equation 4.7 in the linear combination of functions. However, the resulting coefficient associated with this function was found to be zero at all energies analysed, confirming that a statistical mechanism contributed negligibly to dissociation. Therefore, in this analysis it is assumed that each electronic state makes a Gaussian contribution to the overall TKER distribution, with a characteristic mean TKER and standard deviation, σ. The area under each Gaussian reflects the relative probability of I^+ formation from that electronic state of CF_3I^+.

In order to determine the number of Gaussian functions, n, required to properly fit each distribution without over-fitting, the sum of squared residuals between the experimental data and its fit was evaluated for different values of n. Although the residual generally decreases as additional Gaussians are included, cases in which

the improvement was marginal were taken to indicate that the extra component was unnecessary and potentially led to over fitting of the data. A plot of the sum of squared residuals against n for each electron energy is displayed in Figure A.2 in Appendix A.

At 14 and 15 eV, three Gaussian components were sufficient to describe the TKER distributions. In both cases, the dominant contribution arises from a Gaussian centred at approximately 0.3 eV. For comparison, photoionisation studies have reported mean TKER values of between 0.3 and 0.4 eV at ionisation energies close to the vertical ionisation energy of the CF_3I^+ $\tilde{A}$ electronic state (13.3 eV[104]). This strongly suggests that I^+ formation predominantly occurs from CF_3I^+ in its $\tilde{A}$ electronic state at electron energies up to 15 eV.

It has been argued in the literature that CF_3I^+ in the $\tilde{A}$ electronic state does not correlate adiabatically with CF_3 + I^+ in their ground electronic states.[104] Inspection of the potential energy surfaces in Figure 4.5 (b) suggests that the system crosses onto the $\tilde{X}^2$E surface during carbon-iodine bond dissociation, forming the CF_3 ($^2A_1$) + I^+ ($^3P_2$) products.

A barrier to this dissociation is present on the $\tilde{A}$ state potential energy surface at a carbon-iodine distance of approximately 3 Å. The energy difference between the top of this barrier and the CF_3 ($^2A_1$) + I^+ ($^3P_2$) dissociation limit is approximately 0.3 eV. This agrees qualitatively with the observed mean TKER, assuming that the energy released into translation is determined by the barrier height relative to the products. Downie and Powis also found that the TKER distribution is invariant for photon energies up to 13.7 eV,[104] further supporting the idea that kinetic energy release depends on the energy gap between the barrier and products, rather than the initial excitation on the $\tilde{A}$ electronic state.

In addition to the dominant low-energy component, a broader Gaussian centred

at approximately 0.5 eV makes a small contribution to the TKER distributions at both 14 and 15 eV, with a slightly larger relative contribution at 15 eV. This feature may arise as a result of dissociation of CF_3I^+ in the $\tilde{B}$ or $\tilde{C}$ electronic states, which have vertical ionisation energies of 15.38 eV and 16.06 eV, respectively.[122] Although 14 eV lies below both thresholds, the kinetic energy spread within the electron beam might have allowed the $\tilde{B}$ electronic state to be populated at this energy. At 15 eV, the energy spread may have allowed population of both the $\tilde{B}$ and $\tilde{C}$ electronic states. The larger mean TKER for these states is qualitatively consistent with the potential energy surfaces for the $\tilde{B}$ and $\tilde{C}$ states in Figure 4.5 (b), since these surfaces are more repulsive, with a larger energy difference between the Franck-Condon region and the asymptotic products that the $\tilde{A}$ state. Previous studies reported that dissociation of CF_3I^+ in the $\tilde{B}$ and $\tilde{C}$ electronic states predominantly yields CF_2I^+, and that I^+ is only a minor product.[104,105,108] This is consistent with the minor contribution of this feature to the TKER distributions.

At electron energies of 17 and 20 eV, four Gaussian functions were required to fit the TKER distributions. A Gaussian peaking just below 0.3 eV is still a significant component, suggesting that dissociation via the $\tilde{A}$ state of CF_3I^+ continues to play an important role at these energies. However, the distributions exhibit an increasingly pronounced high-energy tail, requiring additional Gaussian components centred at higher TKER values. I^+ has been reported as a major ionic product of dissociation via the $\tilde{D}$ and $\tilde{E}$ electronic states of $CF_3{}^+$, with associated TKER values of 0.4 eV and 0.6 eV, respectively. The mean values of the two higher-energy Gaussians (Gaussian 3 and Gaussian 4 in Table 4.2) agree qualitatively with these values, suggesting that these two electronic states are responsible for the high-energy tail in the TKER distributions.

Although the $\tilde{B}$ and $\tilde{C}$ states are energetically accessible at 17 and 20 eV

and may contribute to the high-energy tail, their contribution to I^+ production is reported to be minor compared to that of the $\tilde{D}$ and $\tilde{E}$ states, since I^+ is reported as a minor product of the $\tilde{B}$ and $\tilde{C}$ states.[104,105,108] Consequently, $\tilde{D}$ and $\tilde{E}$ electronic states are likely to be the dominant contributors to Gaussians 3 and 4. However, at 17 eV, a significant contribution from the $\tilde{E}$ state would not be expected, even when accounting for the kinetic energy spread of the electron beam, given its vertical ionisation threshold of 19.15 eV.[122] Therefore, it is possible that the TKER distribution for dissociation on the $\tilde{D}$ state deviated from a perfectly Gaussian form and extends to higher kinetic energies, artificially increasing the contribution of Gaussian 4.

At all electron energies, a narrow Gaussian fuction centred around 0.1 eV makes a minor contribution to the overall fit. Since it has been established that a statistical dissociation mechanism of vibrationally excited ground state CF_3I^+, which would be characterised by a low release of kinetic energy, appears not to contribute to I^+ production at any energy, it is more likely that this feature accounts for the fact that the kinetic energy release distributions from each electronic state may not be perfectly Gaussian in form.

As a cautionary note, the precise fitting parameters of more minor Gaussian functions should be treated as qualitative, rather than strictly quantitative. The denoising process has an error associated with it that becomes increasingly significant at higher TKER values, where the distributions approach zero intensity. This is evident in the analysis of denoising uncertainty shown in Figure A.1 in the Appendix.

4.4.2 Carbon-fluorine bond dissociation

The scattering distribution of CF_2I^+, the primary ionic product of carbon-fluorine bond dissociation, together with the corresponding TKER distribution shown in

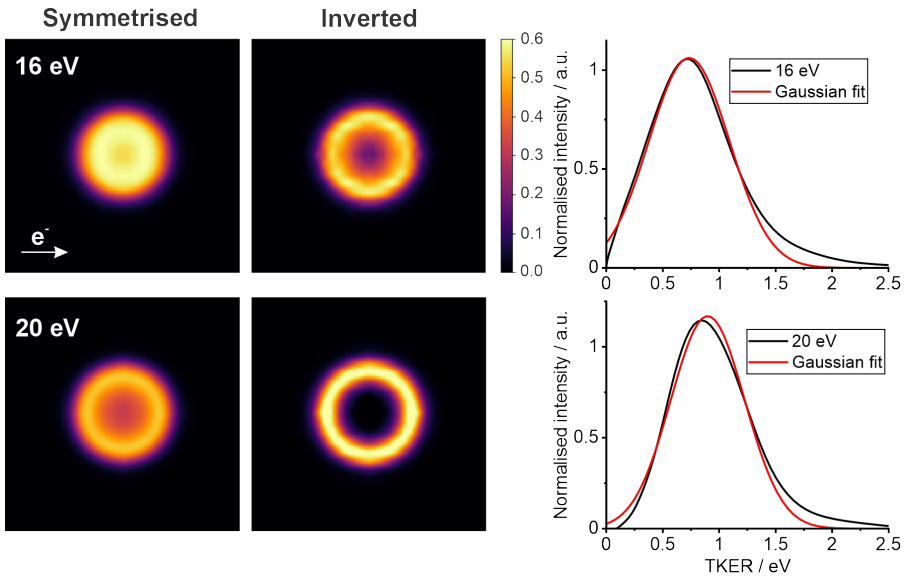


Figure 4.10: Symmetrised and inverted velocity-map images and corresponding TKER distributions for the CF_2I^+ fragment from the dissociative ionisation of CF_3I at electron energies of 16 eV and 20 eV. Gaussian functions have been fitted to the TKER distributions.

Electron energy / eV	Mean TKER / eV
16	0.73
17	0.81
18	0.88
19	0.94
20	0.90

Table 4.3: The mean TKER obtained from the CF_2I^+ ion, tabulated for a series of electron energies.

Figure 4.10, exhibits little variation with electron energy. At both 16 eV and 20 eV, the TKER distributions peak away from zero, indicating that carbon-fluorine bond cleavage occurs on a repulsive potential energy surface. Each of these distributions has been fitted with a Gaussian function. The mean TKER values, summarised in Table 4.3, range from 0.7 eV at 16 eV to 0.9 eV at 20 eV.

These values are in reasonable agreement with a photoionisation study by Low *et al.*,[108] which reported CF_2I^+ formation from the $\tilde{B}$, $\tilde{C}$ and $\tilde{D}$ states of the parent cation with associated TKERs ranging from 0.9 eV for the $\tilde{B}$ state to 1.2 eV for the $\tilde{D}$ state. The increase in mean TKER suggests that as the electron energy increases

from 16 eV to 20 eV, the contribution of the $\tilde{C}$ and $\tilde{D}$ states to the formation of CF_2I^+ grows relative to that of the $\tilde{B}$ state.

4.5 Summary

This chapter has explored the dissociative electron ionisation of CF_3I at low electron energies. Time-of-flight mass spectra were used to identify the dissociation pathways active at each electron energy, while velocity-map imaging data for the $CF_3{}^+$, I^+ and CF_2I^+ products provided insight into the dynamics of carbon-iodine and carbon-fluorine bond cleavage at electron energies up to 20 eV. Features in ion kinetic energy release distributions were assigned to electronic states of the parent cation, guided by calculated potential energy surfaces for carbon-iodine bond dissociation and by comparison with previous photoionisation studies.

5

Electron ionisation of methyl fluoride and methyl chloride at low electron energies

The two lightest methyl halides, methyl fluoride (CH_3F) and methyl chloride (CH_3Cl) are relevant in both natural and industrial contexts. CH_3F finds application as a plasma etching gas,[123] and as an alternative refrigerant with a relatively low global warming potential (GWP).[124,125] CH_3Cl, meanwhile, is the most abundant chlorine-containing gas present in the atmosphere.[126] Common emission sources include biomass combustion, vegetation and the oceans.[127] Industrially, it is also widely used as a reagent in industrial silicone synthesis.[128]

The gas-phase spectroscopy and dissociation dynamics of both compounds have been extensively studied,[129–135] in part because they serve as prototypical alkyl halides. Distinctive dissociative ionisation pathways have been reported, depending on the electronic state in which the parent cation is formed.[129,130] This chapter examines how dissociative electron ionisation varies with incident electron energy, with the aim of disentangling contributions from the low-lying electronic states.

Simple monohalides with large dipole moments, such as CH_3F and CH_3Cl, are also model systems for examining the influence of molecular orientation on

CH_3F			CH_3Cl		
m/z	Identity	Appearance potential / eV	m/z	Identity	Appearance potential / eV
14	CH_2^+	14.53[131]	14	CH_2^+	14.32[131]
15	CH_3^+	14.50[131]	15	CH_3^+	13.38[131]
32	CHF^+	13.91[137]	49	$CH_2{}^{35}Cl^+$	12.981 ± 0.04[138]
33	CH_2F^+	13.358 ± 0.005[138]	50	$CH_3{}^{35}Cl^+$	11.26 ± 0.03[115]
34	CH_3F^+	12.50 ± 0.04[115]	52	$CH_3{}^{37}Cl^+$	11.26 ± 0.03[115]

Table 5.1: The mass peaks arising from the electron ionisation of CH_3F and CH_3Cl at electron energies up to 25 eV and 20 eV, respectively, including their identity and appearance potential.

electron–molecule collisions. Until now, velocity-map images recorded using the electron-molecule crossed-beam apparatus described in this thesis have exhibited isotropic angular distributions. However, the ionisation cross-sections of CH_3F and CH_3Cl are known to depend on the molecule's orientation relative to the incoming electron.[136] As discussed in Section 1.3, one would expect such orientation dependence to give rise to product scattering distribution anisotropy, particularly because carbon-halogen bond cleavage in these systems occurs promptly after ionisation.[129,130]

Data collection took place on the electron-molecule crossed-beam apparatus, described in Chapter 2. Gas for the molecular beam was prepared by mixing CH_3F (Apollo Scientific, PC5080) or CH_3Cl (abcr, AB305612) (20 % partial pressure) with Helium (BOC, UN1046). Velocity-map images and time-of-flight spectra were recorded at a series of electron energies. In an identical manner to that described in Chapter 4, all time-of-flight spectra were recorded under spatial-map imaging conditions. For each data set, corresponding background data were obtained in the manner described in Chapter 4.

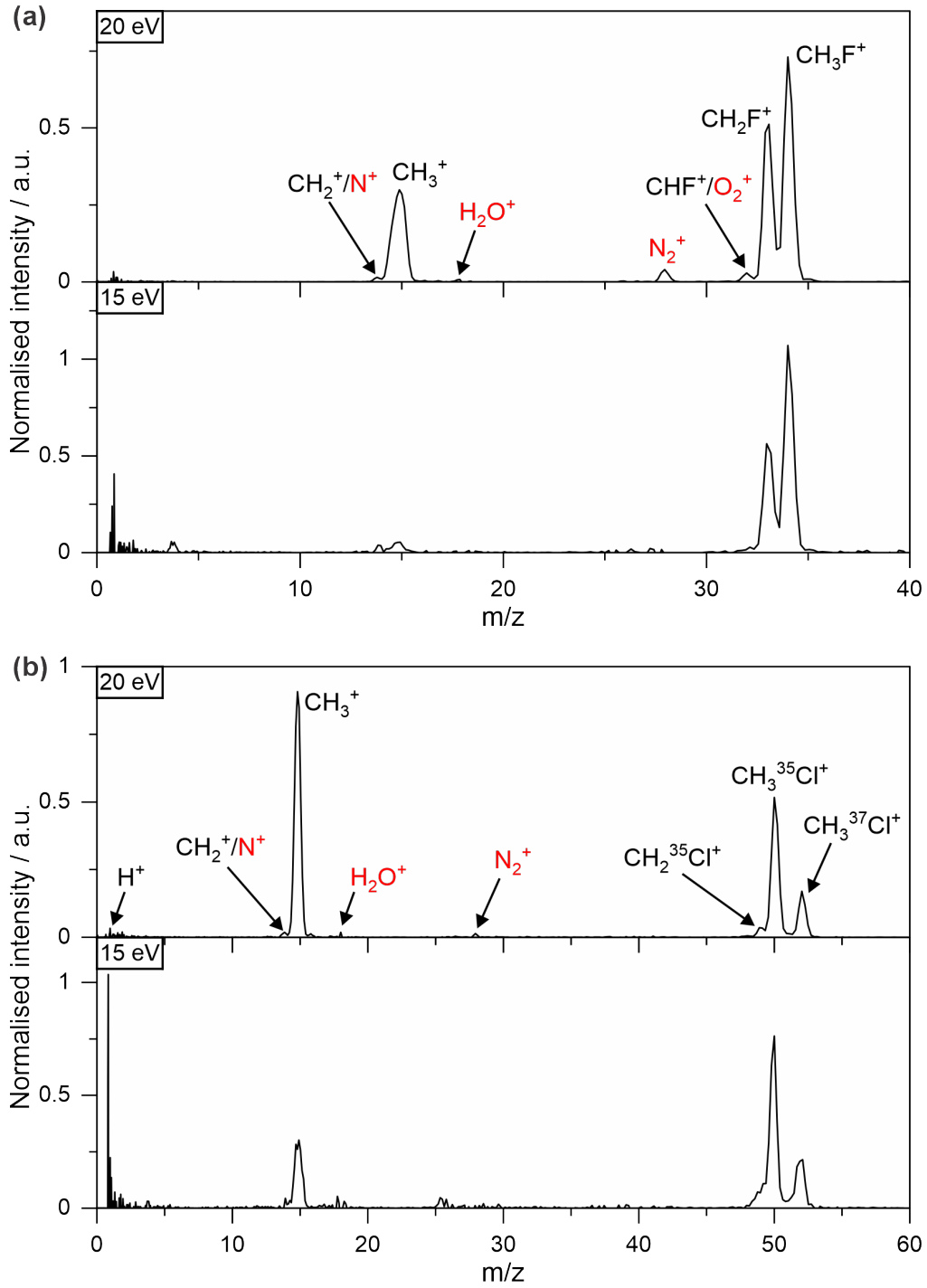


Figure 5.1: Background-subtracted mass spectra of (a) CH_3F and (b) CH_3Cl at electron energies of 15 eV and 20 eV. Peaks corresponding to fragment ions of the methyl halide under study are labelled in black. Peaks arising from residual background signal are labelled in red.

5.1 Mass Spectra

Background-subtracted mass spectra for the electron ionisation of CH_3F and CH_3Cl are displayed in Figure 5.1. Peaks corresponding to fragment ions originating from the molecule under study are labelled in black. Background subtraction often does not eliminate all signal arising from ionisation of background gas, as a result of fluctuations in the electron beam current between signal and background measurements. Peaks attributed to such residual background contributions are labelled in red.

Concentrating first on the mass spectra of CH_3F in Figure 5.1(a), the parent ion CH_3F^+ ($m/z = 34$) is the dominant product ion at both 15 eV and 20 eV. For reference, the ionisation threshold of CH_3F is 12.50 eV. At both energies the most abundant fragment ion is CH_2F^+ ($m/z = 33$), produced by cleavage of a carbon-hydrogen bond. CH_3^+ ($m/z = 15$), the primary ionic product of C-F bond rupture, is present at a lower intensity, indicating that C-H bond cleavage outcompetes C-F bond cleavage at low electron energies. This is consistent with the bond enthalpy of the C-F bond being larger than that of the C-H bond.[139]

The peak at $m/z = 14$ may arise from CH_2^+ or background N^+. Whilst the contribution of N^+ cannot be disregarded completely, the corresponding scattering distribution is centred and circular in form (please refer to Figure B.1(a) in the Appendix B), which is typical of a product formed predominantly at the intersection of the molecular beam and electron beam. If N^+ were a major contributor to this peak, ionisation of background gas along the length of the electron beam path would be evident. CH_2^+ has an appearance potential of 14.53 eV,[131] which accords with its presence in the mass spectra recorded at 15 eV and 20 eV. In this energy range, it is thought to be produced with HF as a neutral co-fragment.[140]

Possible identities for the peak at $m/z = 32$ include CHF^+ and background $O_2{}^+$. The corresponding spatial-map image (displayed in Figure B.1(b) in Appendix B) has the form expected for ions formed from the molecular beam, and both energies surpass the CHF^+ appearance energy of 13.91 eV.[137] Therefore, CHF^+ likely makes a significant contribution to this signal. In this energy range, this ion is believed to be formed with H_2 as a co-fragment.[141] Given the requirement to break two C-H bonds and form one H-H bond, it is perhaps not surprising that CHF^+ is only a minor fragment.

Partial ionisation cross-sections for each fragment ion of CH_3F were calculated in the manner described in Section 4.3, using the total ionisation cross-sections reported by Naghma and Antony.[142] Overlapping peaks were separated at the minimum between the adjacent maxima. The resulting partial cross-sections, which are plotted as a function of electron energy in Figure5.2, are consistent with the trends discussed above and the ion appearance potentials listed in Table 5.1. Notably, the $CH_3{}^+$ partial cross-section grows more rapidly than others beyond 16 eV to become the most abundant ion at 25 eV. This suggests that the $\tilde{A}$ state of the CH_3F^+ cation, which becomes accessible at around 16.25 eV,[143] strongly favours C-F bond cleavage to form $CH_3{}^+$.

Mass spectra of CH_3Cl in Figure 5.1(b) are complicated by the existence of two naturally abundant isotopes of Cl: ^{35}Cl and ^{37}Cl. Consequently, the parent ion signal is split between two peaks at $m/z = 50$, corresponding to $CH_3{}^{35}Cl^+$, and $m/z = 52$, corresponding to $CH_3{}^{37}Cl^+$, with an intensity ratio of 3:1 due to the relative abundance of the respective chlorine isotopes.

The presence of CH_2F^+, $CH_3{}^+$ and $CH_2{}^+$ fragment ions demonstrates that CH_3Cl also dissociates by carbon-hydrogen and carbon-halogen bond cleavage in a similar manner to CH_3F. However, $CH_3{}^+$ is significantly more abundant than

CH_2Cl^+ at both energies, indicating that carbon-halogen bond breaking outcompetes carbon-hydrogen bond breaking in this case. This observation is in accordance with the fact that the C-Cl bond enthalpy is lower than the C-H bond enthalpy.[139]

An H^+ peak is evident in all mass spectra; whilst it is likely that methyl halide dissociation is in part responsible for this signal, residual background H^+ signal is also thought to account for a significant portion. The spatial-map image for this ion shows scatter across the image and is not typical of an ion formed predominantly at the intersection of the electron beam and molecular beam (please refer to Figure B.2 in Appendix B). Given the difficulty in separating H^+ formed from the molecular beam and H^+ formed from background H_2O, the formation of this ion is not considered further in this chapter.

Partial cross-sections were not calculated for CH_3Cl, since the mass resolution was insufficient to distinguish reliably between peaks of higher mass, for example $CH_3{}^{35}Cl^+$ and $CH_2{}^{35}Cl^+$.

The fragmentation channels observed in the energy range under study are summarised by Equations 5.1 to 5.4:

$$CH_3X^+ \longrightarrow CH_2X^+ + H \tag{5.1}$$

$$CH_3X^+ \longrightarrow CH_3{}^+ + X \tag{5.2}$$

$$CH_3X^+ \longrightarrow CH_2{}^+ + HX \tag{5.3}$$

$$CH_3F^+ \longrightarrow CHF^+ + H_2 \tag{5.4}$$

where X = F or Cl.

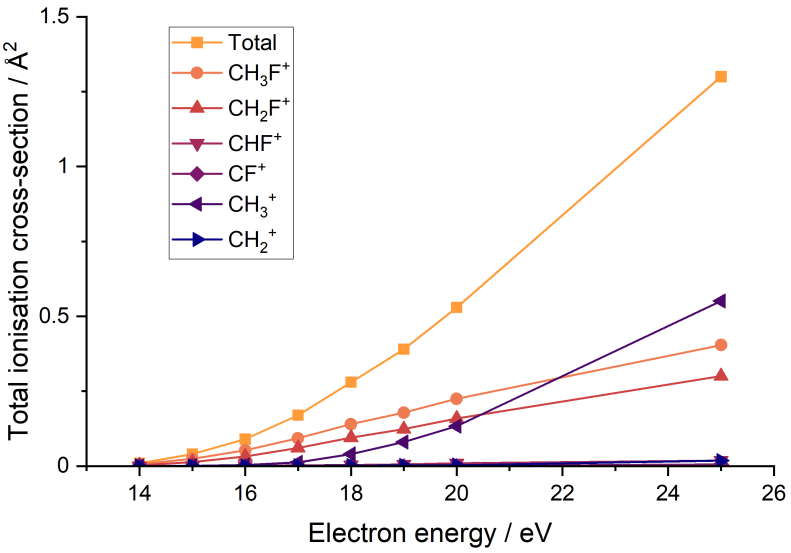


Figure 5.2: Partial ionisation cross-sections of the fragments produced by the electron ionisation of CF_3I, plotted as a function of electron energy. Total ionisation cross-section data measured by Verma *et al.*[116] have been used to to scale the relative abundances of each ion.

5.2 Velocity-Map Images

Discussion of the velocity-map imaging data for both CH_3F and CH_3Cl focuses on pathways involving cleavage of the carbon-halogen bond. In order to aid interpretation of the velocity-mapping data, potential energy curves for the low-lying electronic states of CH_3F^+ and CH_3Cl^+ along the carbon-halogen bond coordinate, calculated by Xi *et al.* using the CASSCF/CASPT2 level of theory, are plotted in Figure 5.3.[144,145] State labelling in the Franck-Condon region considers the Jahn-Teller distortion of CH_3F^+ and CH_3Cl^+, which has the effect of splitting the doubly-degenerate $\tilde{X}(^2E)$ state into the $1^2A'$ state and $1^2A''$ state. For CH_3F^+, the $\tilde{A}(2^2A')$ state is calculated to be repulsive; both this state and the $\tilde{X}(^2E)$ ground state correlate with the first dissociation limit of $CH_3^+(1^1A_1') + Cl$). In the case of CH_3Cl^+, although the $\tilde{A}^2A_1(2^2A')$ state is initially repulsive, a slight well in the potential exists along the C-Cl dissociation coordinate. In both cases, the bound

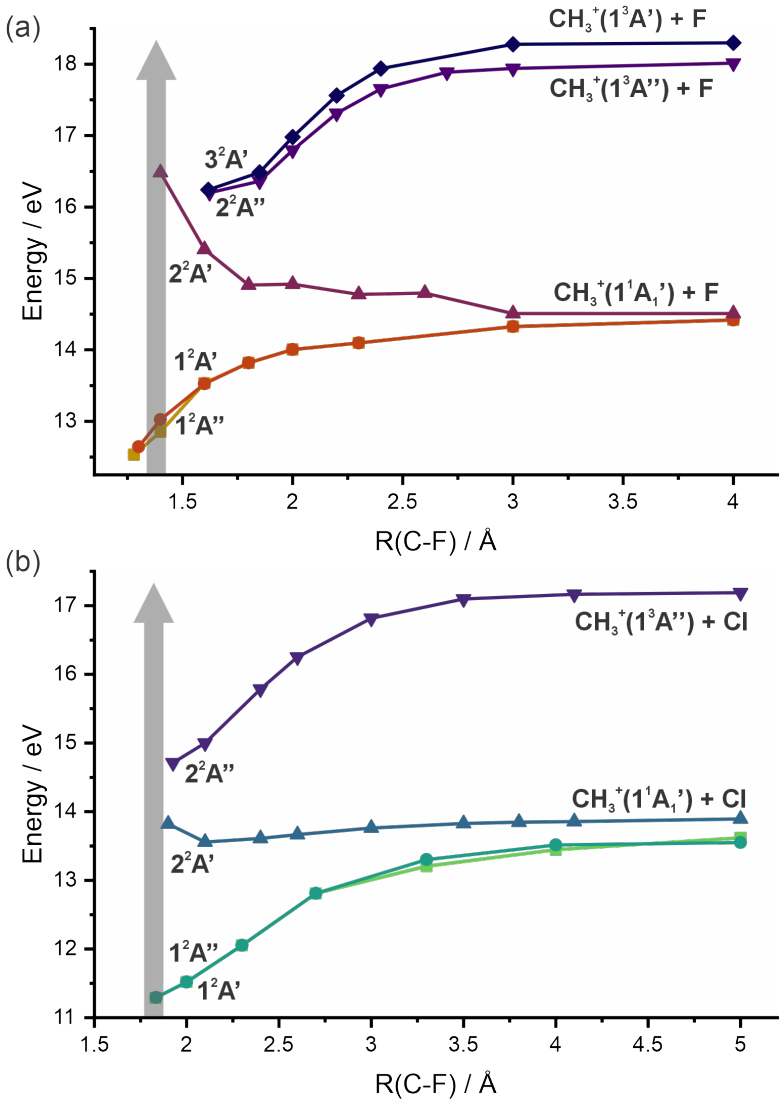


Figure 5.3: Potential energy curves for the low-lying electronic states of (a) CH_3F^+ along the C-F bond and (b) CH_3Cl^+ along the C-Cl bond. Calculations were conducted by Xi et al. using the CASSCF/CASPT2 levels of theory[144,145] State labelling in the Franck-Condon region accounts for the Jahn-Teller distortion of CH_3F^+ and CH_3Cl^+.

$\tilde{B}(^2E)$ state is split into the $2^2A''$ state and $3^2A'$ state (not shown for CH_3Cl^+), which correlate with the $1^3A''$ and $1^3A'$ states of the CH_3^+ fragment, respectively.

5.2.1 CH_3F dissociation: product kinetic energy distributions

Beginning with CH_3^+ ions produced from CH_3F, two distinct components are evident in the TKER distributions of Figure 5.4. A low energy feature, peaking

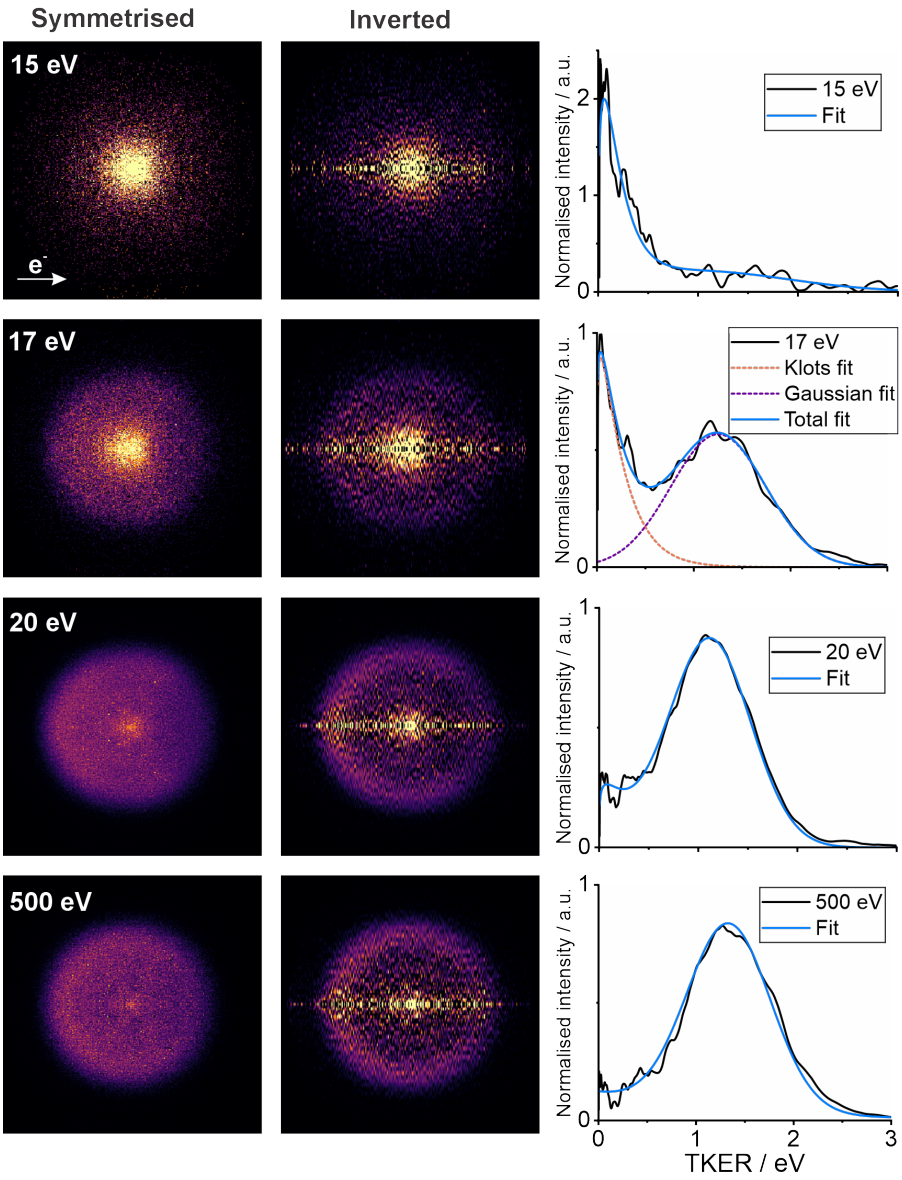


Figure 5.4: Symmetrised and Abel-inverted velocity-map images of CH_3^+ produced by the electron ionisation of CH_3F at electron energies of 15, 17, 20 and 500 eV. The electron beam propagation (horizontal) axis is taken as the axis of cylindrical symmetry. The corresponding TKER distributions are fitted using Equation 5.5, which is a sum of a Gaussian function and Klots' model.[120] The individual Gaussian and Klots' model components are displayed for 17 eV.

close to 0 eV, is likely to be the result of a 'statistical' dissociation pathway from vibrationally excited levels of the bound $\tilde{X}$ electronic ground state. A PEPICO study by Tang *et al.* reports similar findings; CH_3^+ TKER distributions had the form of a Boltzmann distribution at photon energies below 16 eV. This low-energy feature can be described by Klots' 'model free' approach,[120] which is described in more detail in Chapter 4. A second feature, peaking away from 0 eV, becomes evident as the electron energy increases. This is indicative of an impulsive, direct dissociation occurring along a repulsive potential energy surface and can be fitted with a Gaussian function, peaking at TKER values between 1.0 eV and 1.3 eV. Tang *et al.* reported similar results, in which a Gaussian component, peaking at approximately 1.3 eV, appeared in the TKER distribution at photon energies above 16 eV. Vertical ionisation to the CH_3F^+ $\tilde{A}$ state becomes accessible between 16 eV and 17 eV. Figure 5.3 shows this potential energy surface to be repulsive with respect to carbon-fluorine bond cleavage, so the impulsive dissociation pathway is most likely to occur from this state.

CH_3^+ TKER distributions, including those displayed in Figure 5.4, have been fitted with a function (Equation 5.5) consisting of a sum of the two model functions.

$$A\left(E_{\mathrm{T}}^{l}\exp\left(-\frac{E_{\mathrm{T}}}{k_{\mathrm{B}}T^{\ddagger}}\right)\right)+B\left(\exp\left(-\frac{\left(E_{\mathrm{T}}-E_{\mathrm{T},0}\right)^{2}}{2\sigma^{2}}\right)\right) \tag{5.5}$$

Here, E_T denotes the TKER, and $E_{\mathrm{T},0}$ and σ are the mean and standard deviation of the TKER associated with the Gaussian component, respectively. The parameter l is a fitting parameter constrained between 0 and 1. $T^{\ddagger}$ is defined as the transition state temperature, determined by the average kinetic energy when passing through the transition state.[121] A and B are coefficients for the Klots and Gaussian functions, respectively.

Electron energy / eV	$T^{\ddagger}$ / K	$E_{T,0}$	σ	Klots area	Gaussian area
15	1733 (66)	1.0 (0.3)	0.9 (0.3)	0.55	0.45
16	2118 (152)	1.0 (0.1)	0.7 (0.1)	0.44	0.56
17	1716 (36)	1.0 (0.01)	0.4 (0.01)	0.26	0.74
18	2151 (219)	1.2 (0.008)	0.4 (0.008)	0.13	0.87
19	2142 (270)	1.0 (0.006)	0.4 (0.006)	0.11	0.89
20	2838 (555)	1.1 (0.005)	0.4 (0.005)	0.10	0.90
500	16040 (3036)	1.3 (0.005)	0.4 (0.006)	0.15	0.85

Table 5.2: Parameters obtained from fitting TKER distributions of CH_3^+ produced from CH_3F at various electron energies with Equation 5.5. Uncertainties in parameters, given by their standard deviations from fitting, are displayed in brackets.

Parameters from the fitted distributions are listed in Table 5.2. The areas under the Klots and Gaussian components of the fitting function indicate the relative probability that CH_3^+ ions are formed in a statistical or direct dissociation at a particular electron energy, respectively. It should be noted that at higher electron energies, above 17 eV, where the Klots component is small, the uncertainty on the Klots coefficient, A, is larger than the value itself. In spite of this, the general trend of the Gaussian component dominating is still valid.

At 15 eV, just above the appearance energy of CH_3^+, the statistical pathway is the major contributor to CH_3^+ formation. Given that only the $\tilde{X}$ state is accessible by vertical ionisation at this energy, this is consistent with the potential energy surfaces in Figure 5.3 (a). However, the energy spread of the electron beam (1.3 eV FWHM) means that some ions were formed in the $\tilde{A}$ state, hence the Gaussian component still makes a notable contribution to the TKER distribution.

At electron energies of 16 eV and above, the Gaussian component of the TKER distribution grows rapidly, coinciding with the $\tilde{A}$ state of CH_3F^+ becoming energetically accessible. The dominance of this feature above 17 eV shows that once accessible, dissociation from the $\tilde{A}$ state, which is not subject to any barrier, outcompetes fragmentation from the $\tilde{X}$ state, for which there is a barrier and

the timescale of dissociation longer.

As the electron energy increases further above 18 eV, the $\tilde{B}$ state threshold is surpassed.[144] However, this state appears to have little effect on the observed dynamics. This observation is consistent with a study by Eland et al. in PEPICO experiments,[146] which found that $\tilde{B}$ state parent cations underwent internal conversion to the $\tilde{A}$ state prior to C-F cleavage. This is not surprising given the bound nature of the $\tilde{B}$ state and the small energy gap between the $\tilde{A}$ and $\tilde{B}$ states in the Franck-Condon region.

It should be noted that the significant increase in the value of $T^{\ddagger}$ at high electron energies should be treated with some caution. The statistical dissociation mechanism makes such a small contribution at higher electron energies that obtaining a reliable value of $T^{\ddagger}$ from the fit is difficult. However, it is still notable that the TKER distribution recorded at an electron energy of 500 eV shows little qualitative difference to that recorded at 20 eV, strongly suggesting that even at higher electron energies, low-lying electronic states of CH_3F^+ dominate the fragmentation dynamics.

Velocity-map images of CH_2^+ produced from CH_3F are displayed in Figure 5.5. At electron energies of 16 eV and 20 eV, the corresponding TKER distributions peak close to zero, indicating that dissociation predominantly proceeds via a statistical mechanism on the bound $\tilde{X}$ electronic state of the parent cation. On this state, CH_2^+ is thought to be formed in the $\tilde{X}$ and $\tilde{A}$ states, with HF[140] as a co-fragment. The values of $T^{\ddagger}$ obtained by fitting the Klots model to the 16 and 20 eV distributions are 1153 and 1132 K, respectively. These are lower than the values determined for the formation of CH_3^+ from the $\tilde{X}$ state of the parent cation, indicating a lower release of kinetic energy. This suggests that the CH_2^+ + HF channel encounters a larger barrier, consistent with the requirement to break both a C-F and C-H bond in a manner that facilitates the formation of an H-F bond. At 20 eV, the $\tilde{A}$ and $\tilde{B}$ states

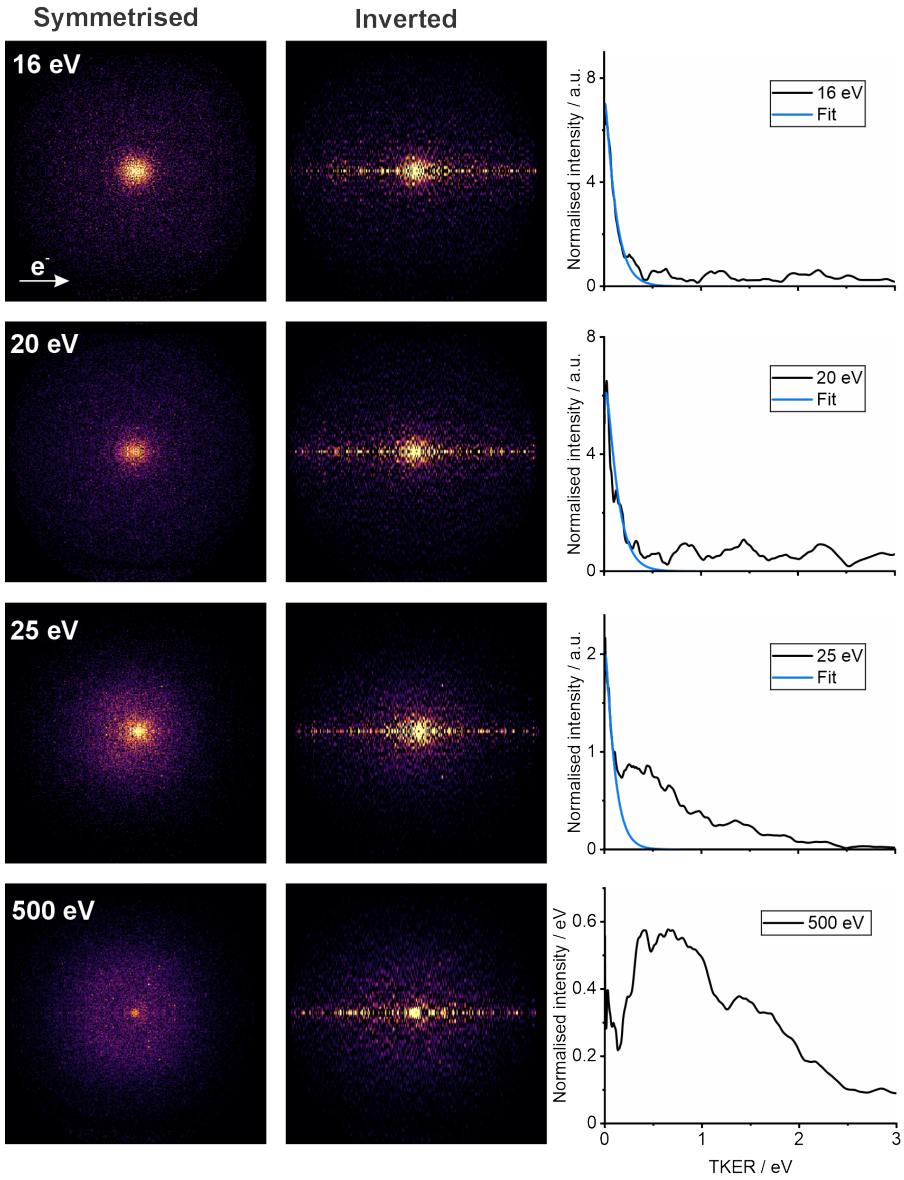


Figure 5.5: Symmetrised and Abel-inverted velocity-map images of CH_2^+ produced by the electron ionisation of CH_3F at electron energies of 16, 20, 25 and 500 eV, displayed with corresponding TKER distributions. TKER distributions for 16, 20 and 25 eV are fitted using the Klots model (Equation 4.7), considering the distributions only up to a TKER value of 0.14 eV. Given that this model assumes dissociation to be purely statistical, this allows any significant deviation from statistical behaviour in the TKER distributions to be visualised.

of CH_3F^+ are energetically eccessible, but do not appear to contribute significantly to CH_2^+ production, given the similarity of the TKER distributions at 16 eV and 20 eV.

At 25 eV, CH_2^+ formation still proceeds via a statistical dissociation mechanism, as evidenced by the significant peak close to zero in the TKER distribution. The Klots model has been fitted by considering the distribution up to a TKER value of 0.14 eV, in order to highlight this feature at low kinetic energy. However, a shoulder extending up to approximately 2.5 eV appears in the distribution, indicating that a channel forming CH_2^+ with a larger release of kinetic energy is energetically accessible. This observation shows good agreement with electron ionisation TKER data previously reported by Locht and co-workers, which found a maximum TKER value of 3.0 eV at an electron energy of 25 eV.[147] The $\tilde{C}$ state of CH_3F^+, which has an adiabatic ionisation energy of 22.5 eV, is likely to be responsible for this dissociation channel; its dissociative nature is evidenced by a lack of vibrational structure in the corresponding photoelectron band.[147,148] Locht *et al.* argued that this dissociation channel most likely produces CH_2^+, accompanied by atomic H and F as co-fragments.[147]

The shoulder is the most significant feature in the TKER distribution at 500 eV, indicating that direct dissociation is dominant at higher electron energies. This behaviour closely parallels CH_3^+ production: once a rapid, direct dissociation channel is energetically accessible, it grows to become dominant.

5.2.2 CH_3Cl dissociation: product kinetic energy distributions

Symmetrised and inverted velocity-map images for CH_3^+ produced from CH_3Cl are displayed in Figure 5.6. The corresponding TKER distributions are similar in form to those obtained for CH_3F: a feature at low kinetic energy indicates a

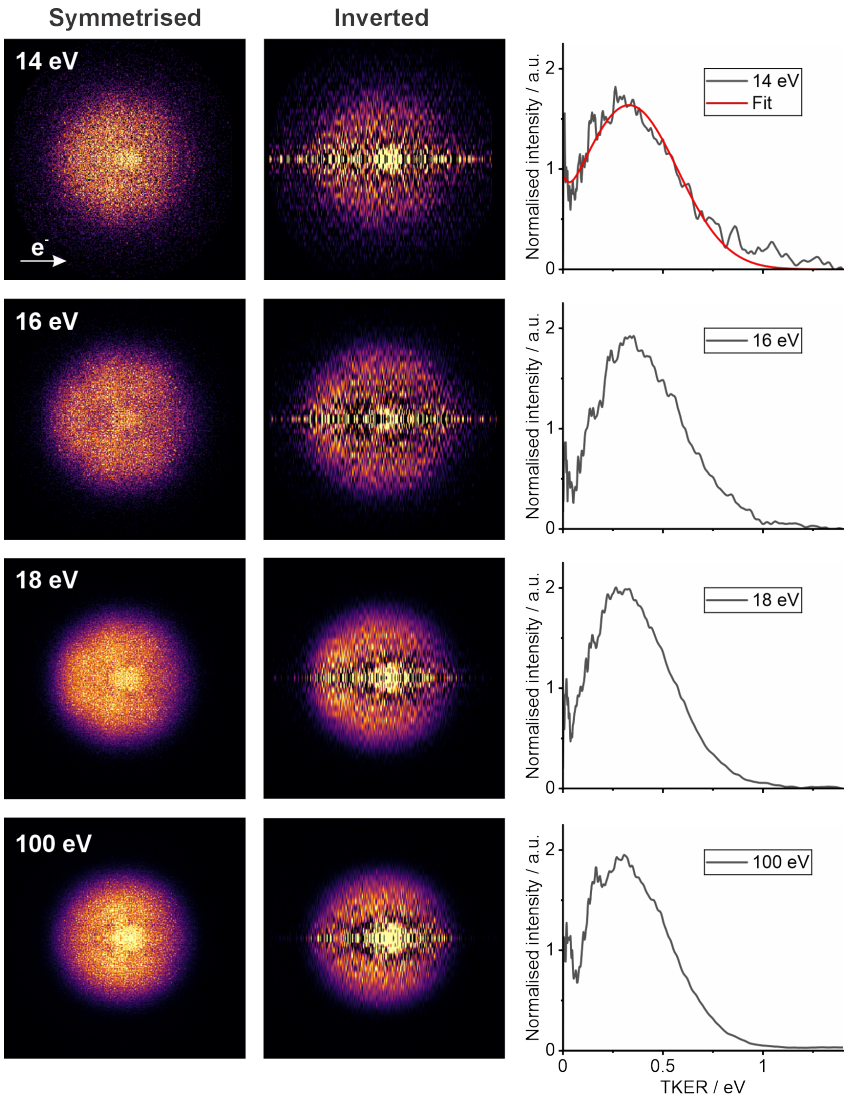


Figure 5.6: Symmetrised and inverted velocity-map images for CH_3^+ produced from CH_3Cl at 14, 16, 18 and 100 eV are displayed with associated TKER distributions. The TKER distribution for 14 eV has been fitted with Equation 5.5, which is a sum of a Gaussian function and Klots' model.[120]

statistical dissociation mechanism, whereas a feature peaking between 0.3 eV and 0.4 eV results from an impulsive dissociation pathway.

Photoionisation studies have found that impulsive dissociation occurs on the $\tilde{A}$ state of CH_3Cl^+, with reported kinetic energy releases of between 0.35 eV and 0.45 eV.[131,149] The calculated potential energy surfaces in Figure 5.3 (b), which find the $\tilde{A}$ state to be repulsive with respect to Cl loss, are qualitatively consistent with these findings. At each electron energy, a tail to higher kinetic energies is evident on

Electron energy / eV	$T^{\ddagger}$ / K	$E_{T,0}$	σ	Klots area	Gaussian area
14	222 (126)	0.33 (0.005)	0.24 (0.006)	0.008	0.992
16	181 (131)	0.37 (0.002)	0.21 (0.003)	0.003	0.997
18	245 (216)	0.33 (0.002)	0.21 (0.003)	0.004	0.996
20	250 (180)	0.29 (0.003)	0.19 (0.003)	0.007	0.993
100	282 (99)	0.32 (0.003)	0.21 (0.004)	0.016	0.984

Table 5.3: Parameters obtained from fitting TKER distributions of CH_3^+ produced from CH_3Cl at various electron energies with Equation 5.5. Uncertainties in parameters, given by their standard deviations from fitting, are displayed in brackets.

the Gaussian component. This slight deviation from Gaussian form is likely to be the result of the small well in the $\tilde{A}$ state that exists along the carbon-chlorine coordinate.

Each TKER distribution was fitted with Equation 5.5, with the resulting best-fit parameters listed in Table 5.2. An example fit is displayed in Figure 5.6 for an electron energy of 14 eV.

In contrast to CH_3F, the impulsive mechanism dominates the dissociation dynamics at all electron energies investigated. Although the $\tilde{A}$ state vertical ionisation energy of 14.4 eV[150] exceeds the lowest electron energy used in this study of 14 eV, it still lies well within the FWHM of the electron beam energy distribution. The dominance of the impulsive dissociation channel mirrors the behaviour of CH_3F dissociative electron ionisation: once a repulsive state becomes energetically accessible, it becomes the dominant dissociation pathway.

Both the $\tilde{X}$ state and the $\tilde{B}$ state are bound states, so are likely to give rise to statistical dissociation pathways. Whilst statistical chlorine loss has been observed from $\tilde{B}$-state CH_3Cl, it is not widely reported from the $\tilde{X}$ state. However, a statistical dissociation pathway is open at an electron energy of 14 eV, most likely from excited vibrational levels of the $\tilde{X}$ state. At this energy, the vertical ionisation energy of the $\tilde{B}$ state (15.4 eV[150]) lies well outside of the electron beam energy FWHM. Above the $\tilde{B}$ state threshold, it is likely that both the $\tilde{X}$ state and the

$\tilde{B}$ state contribute to the statistical dissociation component of the signal. In fact, it has been hypothesised that $\tilde{B}$ state CH_3Cl^+ may undergo internal conversion to the $\tilde{X}$ state before dissociating.[130,131]

5.3 Dependence on molecular orientation

A clear left-right anisotropy is visible in the velocity-map images of CH_3^+ formed from both CH_3F and CH_3Cl at electron energies of 17 eV and above. As a reminder, anisotropy in scattering distributions can be considered by expressing the product scattering distribution as a linear combination of Legendre polynomials in $\cos\theta$, where, in the case of electron-molecule crossed-beam experiments, θ is the angle between an ion's velocity vector and the axis of cylindrical symmetry. In the case of the electron-molecule crossed beam experiment, the electron beam propagation axis is considered the symmetry axis (please refer to Sections 1.3 and 3.3 for further details).

Left-right anisotropy is described by terms up to and including the first Legendre Polynomial. Therefore, Equation 1.9 can be simplified to:

$$I(r,\theta) = I(r)(1 + \beta_1(r)\cos\theta). \tag{5.6}$$

Here, $\beta_1(r)$ quantifies the extent of left-right anisotropy as a function of image radius, and can range between -1 and 1. If $\beta_1 > 0$, the CH_3^+ ion is more likely to recoil in the direction of electron beam propagation (i.e. to the right in all images); if $\beta_1 < 0$, CH_3^+ is more likely to recoil counter to the direction of electron beam propagation (i.e. to the left in all images).

Figure 5.7 shows the CH_3^+ β_1 distributions for CH_3F and CH_3Cl at an electron energy of 20 eV, plotted with the corresponding TKER distributions for comparison.

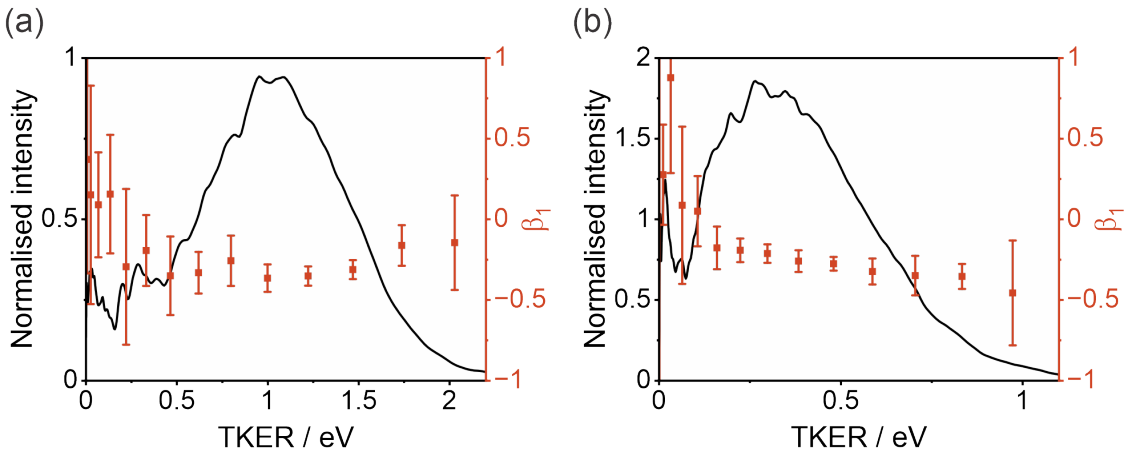


Figure 5.7: The β_1 anisotropy parameter of the CH_3^+ scattering distribution, plotted as a function of TKER for (a) CH_3F and (b) CH_3Cl at an electron energy of 20 eV. Values for β_1 have been obtained by applying a nine-point moving average, symmetric about a central point. The standard deviation of these nine points was calculated and plotted as an error bar. In both cases, the TKER distribution is plotted for reference.

In both cases, the β_1 distribution is generally negative, particularly at higher TKER values, which manifests as a higher intensity on the left hand side of the images. This is particularly the case in the range of the Gaussian peak in the TKER distribution, which corresponds to rapid carbon-halogen bond cleavage from the $\tilde{A}$ state of the parent cation.

The axial-recoil approximation states that fragments recoil along the axis of the bond being broken in the original molecular orientation if the timescale for bond dissociation is significantly shorter than the timescale of molecular rotation. By this approximation, these observations indicate that formation of CH_3^+ ions from the $\tilde{A}$ state of the parent cation is more likely if the CH_3 group of the parent molecule is oriented towards the incoming electron.

There are several possible explanations for this result. Firstly, CH_3F and CH_3Cl are both polar molecules, so the CH_3 group has a partial positive charge. Furthermore, lone electron pairs are localised at the halogen end of the molecule, which may serve to repel incoming electrons.

Aitken and co-workers found that the ionisation cross-sections of symmetric top methyl halides, including CH_3Cl, were dependent on the molecular orientation relative to the incoming electron, with a higher probability of ionisation at the CH_3 group than at the halogen.[52] In these experiments, a neat beam of methyl halide molecules was first quantum-state selected in a hexapole. Molecules were oriented in a homogeneous field, so that either end of the molecule could be presented to the 200 eV incident electron beam. The resulting ion signals were then measured to determine how the ionisation cross-section depends on molecular orientation.

Whilst parent ion formation showed a strong orientation dependence, the formation of CH_3^+ exhibited little dependence. Considering the experimental configuration of Aitken *et al.*, it is unlikely that their experiments would have been sensitive to an orientation dependence in CH_3^+ production. A supersonic beam of neat CH_3Cl is estimated to have a terminal velocity of 700 ms^{-1}. Based on a 25 mm distance between the electron-molecule interaction region and quadrupole mass spectrometer inlet,[51] an estimate for the time taken for ions produced to enter the mass spectrometer can be estimated. In order to compare the results of Aitken *et al.* with the present study, this time can be used to plot the data in Figure 5.7 (b) as a function of distance travelled in the direction perpendicular to the molecular beam axis, prior to enetering the quadrupole inlet. Assuming that the molecules are oriented orthogonally to the molecular beam axis, the resulting distribution is displayed in Figure 5.8.

CH_3^+ ions produced from the repulsive $\tilde{A}$ state, whose production is particularly associated with the observed anisotropy, travel a significant distance away from the molecular beam axis. Consequently, such ions would almost certainly not have entered the quadrupole mass spectrometer to be detected. In the experiments of Aitken and co-workers, the hexapole Stark-state selector dimensions were chosen

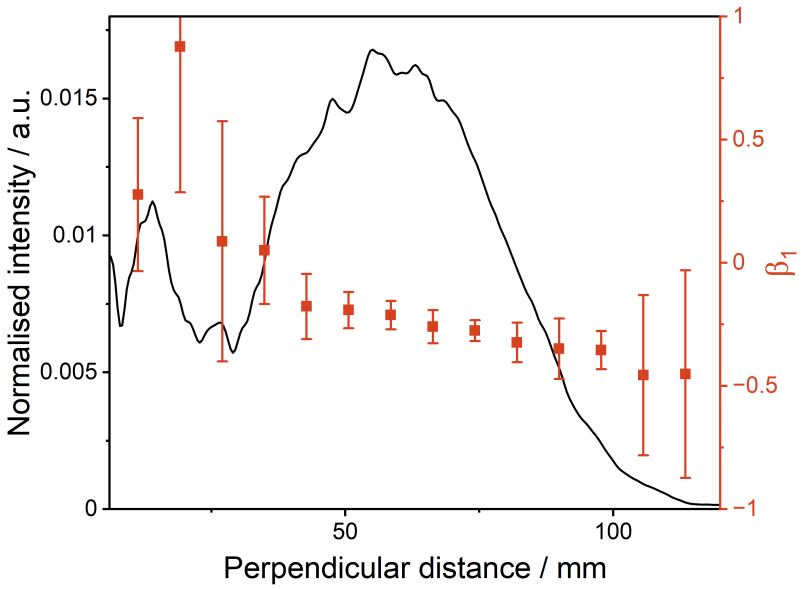


Figure 5.8: The radial distribution of CH_3^+ produced from CH_3Cl at an electron energy of 20 eV from the present study, plotted as a function of distance travelled perpendicular to the molecular beam axis in the experimental configuration of Aitken *et al.*[51,52] Further details can be found in the text.

to optimise transmission rather than state selectivity. As a consequance, not all molecules would have been oriented perpendicular to the molecular beam axis. However, the magnitude of CH_3^+ recoil in Figure 5.8 is sufficiently large that even those ions originating from molecules with an orientation that is not perfectly orthogonal to the molecular beam axis were highly unlikely to have entered the quadrupole inlet. Therefore, despite the fact that Aitken *et al.* did not report an orientation dependence for CH_3^+ production from CH_3Cl, further analysis indicates that their observations remain consistent with the findings of the present study.

Returning to the present study, given that the effect is most apparent for ions formed via direct dissociation from the $\tilde{A}$ state of the parent cation, it appears that the axial recoil approximation breaks down for ions formed with a lower kinetic energy. This is consistent with statistical dissociation of parent cations formed in

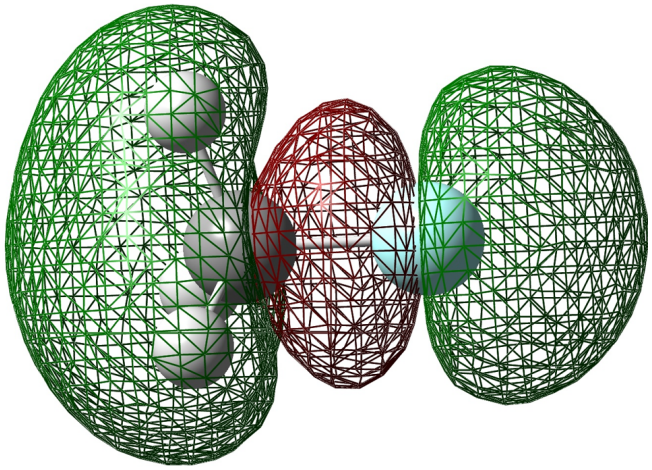


Figure 5.9: The highest-lying C-F sigma bonding orbital in CH_3F.

the bound $\tilde{X}$ state, which occurs over longer timescales. Ions formed in the $\tilde{X}$ state have time to rotate significantly before the carbon-halogen bond breaks, thus weakening the link between the orientation of the molecule when ionised and the recoil vector of the resulting fragment ion. Additionally, in the case of CH_3Cl, this can explain the increasing negativity of β_1 with increasing TKER. The axial recoil approximation holds best for those ions formed with the greatest kinetic energy.

Orbital effects may also be used to explain the observed anisotropy. In both molecules, the $\tilde{A}$ state of the parent cation is formed by the removal of an electron from the valence orbital associated with the carbon-halogen bond.[129,130] Focussing on CH_3F, this bonding orbital, which is displayed in Figure 5.9, has a larger lobe at the CH_3 group than at the fluorine. Therefore, this orbital presents a larger cross-section when the CH_3 group is oriented towards the incoming electron.

In order to compare the orientation dependence between images recorded at different electron energies for both CH_3F and CH_3Cl, the mean of the β_1 distribution has been calculated over the range of the FWHM of the Gaussian component of the TKER distribution. These results are displayed in Table 5.4.

Across a range of electron energies, the mean β_1 value for CH_3F is more negative

CH_3F		CH_3Cl	
Electron energy / eV	Mean β_1	Electron energy / eV	Mean β_1
17	-0.35	16	-0.24
20	-0.33	20	-0.19
25	-0.32	100	-0.12
500	-0.24		

Table 5.4: Mean β_1 values of CH_3^+ velocity-map images for CH_3F and CH_3Cl, calculated within the FWHM of the Gaussian component of the TKER distributions.

than that for CH_3Cl. This is not surprising, since CH_3F is a more polar molecule than CH_3Cl, so the CH_3 group has a larger partial positive charge. Furthermore, chlorine is a larger atom than fluorine, with 3p valence orbitals rather than 2p. Therefore, the chlorine atom of CH_3Cl presents a larger target to an incident electron than the fluorine atom of CH_3F. In some cases, dissociating CH_3Cl^+ may become temporarily trapped in the small well in the $\tilde{A}$ state potential energy surface. In this scenario, CH_{3+} would be produced with a lower kinetic energy release and the molecule would have time to rotate, thereby weakening the observed orientation effect.

As the electron energy increases, the mean β_1 value for both compounds becomes less negative. At higher electron energies, parent cations may be formed in a range of excited electronic states, which may relax rapidly to the dissociative $\tilde{A}$ state prior to fragmentation. However, the cross-sections for formation of ions in each initial state will almost certainly have a different dependence on the molecular orientation relative to the incoming electron, depending on the shape of the molecular orbitals concerned, with a corresponding effect on the observed anisotropy.

5.4 Summary

The electron-induced dissociation of CH_3F and CH_3Cl has been investigated at a range of electron energies. Velocity-mapping data reveal distinct statistical and direct dissociation mechanisms that become accessible at different electron energies,

associated with dissociation on the $\tilde{X}$ and $\tilde{A}$ states of the parent cation. Electronic states have been assigned to these dynamics based on comparison with published photoionisation experiments and theoretical studies. Experiments conducted at higher electron energies, when a multitude of electronic states are energetically accessible, reveal remarkably similar fragmentation dynamics, indicating that dissociation of monocations remains largely governed by low-lying electronic states of the parent cation. The scattering distributions of CH_3^+ exhibit anisotropic angular distributions, particularly for direct dissociation pathways, strongly suggesting that the ionisation cross-section is dependent on the orientation of the molecule relative to the incoming electron. This effect can be rationalised by considering the polarity and orbital shapes of the parent molecule.

6

Characterisation of a laser-induced desorption source

6.1 Introduction

In order to study the electron-induced fragmentation dynamics of larger, non-volatile molecules, a laser-induced desorption (LID) source was installed on the electron-molecule crossed-beam apparatus in place of the pulsed molecular beam valve. The design of the source follows that developed by Milesevic *et al.*, with some modifications to fit the geometry of the electron-molecule crossed beam instrument. The original source was extensively characterised on a photoionisation velocity-map imaging experiment.[77] The geometry of the molecular plume generated by the LID source affects the velocity-mapping process; therefore, the new source was characterised after installation on the electron rig, in order to optimise its performance on this particular experiment. The source's performance is judged by several criteria. Firstly, the source must generate mostly intact parent molecules in the gas phase, as the ionisation and detection of fragments formed by the desorption process would contaminate data sets and complicate interpretation.

Secondly, the size of the interaction volume of the electron beam and molecular plume produced by the LID source greatly affects the ability of the ion lens to velocity-map the ionic products; the larger the interaction volume, the harder it is to achieve velocity-mapping conditions. The molecular plume must therefore be sufficiently collimated to yield a well-defined and sufficiently small interaction volume. Finally, desorption must occur at a consistent rate that produces a high enough number density of molecules in the interaction region, to enable collection of data with sufficient signal-to-noise ratio within a reasonable time frame. Each of these criteria is addressed over the remainder of this chapter.

The LID source is configured as set out in Section 2.2. Throughout the characterisation, triphenylene (Merck, T82600, 98 %) was used as a sample molecule and the gas-phase molecules that were prepared were ionised by a 100 eV electron beam. The molecular samples are deposited onto the tantalum disc that forms the tip of the LID source. This was achieved by a recrystallisation technique; as follows:

1. Triphenylene is dissolved in the minimum volume of hot toluene;
2. A drop of the resulting solution is added with a pipette to the tantalum foil, which is heated on a hotplate;
3. The foil is allowed to dry before another drop is added;
4. Once a triphenylene layer of the desired thickness has built up, the sample is heated to 80 °C in an oven to remove residual toluene solvent.

6.2 Effect of sample thickness on ion signals

The effects of varying the triphenylene layer thickness on (i) the triphenylene ion signal levels (i.e. the number of triphenylene ions detected in each acquisition cycle)

Sample	Triphenylene mass / mg
Thin	23
Medium	61
Thick	112

Table 6.1: Details of samples characterised for use on the LID source.

observed in the electron-molecule collision experiments, and (ii) sample longevity were investigated by preparing three samples of different thickness. It was not possible to accurately measure the triphenylene layer thickness, which is unlikely to have been uniform across the foil surface. The three samples that are detailed in Table 6.1 are labelled under the assumption that depositing a larger mass of triphenylene on the foil surface resulted in a thicker sample.

In each case, the diode laser used to heat the sample was driven with a diode current of 500 mA (a power of approximately 0.3 W at the tip). Time-of-flight mass spectra of the ions formed by the interaction of the resulting molecular plume and the electron beam were recorded under spatial-mapping conditions for 40,000 acquisition cycles (approximately 26 minutes), before the diode laser was switched off. Data acquisition continued while the foil cooled. Triphenylene parent ion signal level, determined by monitoring the number of ions arriving in an arrival time window corresponding to this ion's m/z ratio, is plotted in Figure 6.1 as a function of acquisition time (i.e. the length of time after the diode laser was switched on) for each of the three samples. A number of trends are apparent. The thinner the sample, the faster the increase in parent ion signal when the diode laser is switched on. Heat is transferred to the triphenylene molecules that are exposed to vacuum more quickly, so the critical temperature for sample desorption to occur is reached sooner. Triphenylene signal increases rapidly in the 'thin' and 'medium' cases, before decreasing approximately exponentially as the sample depletes; desorption has almost completely ceased from the 'thin' sample before

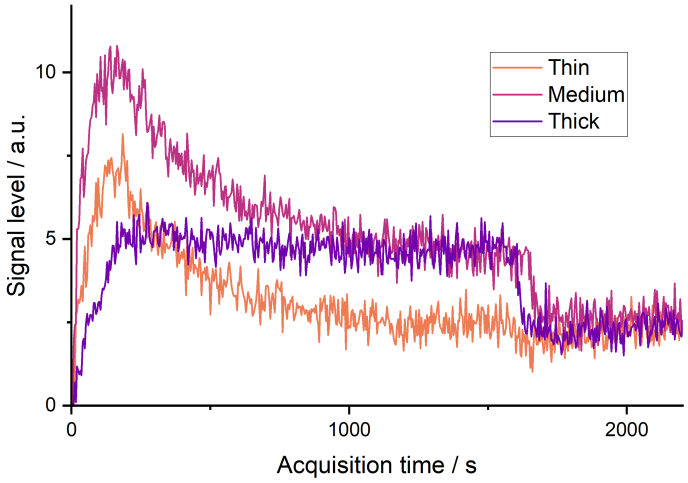


Figure 6.1: Variation of the parent ion signal with acquisition time for three sample thicknesses. Each plot was shifted to start from zero. A 101 point moving average has been applied.

the diode laser is switched off, as the sample is exhausted in the spot where the diode laser is focused on the rear side of the foil.

In contrast, triphenylene signal increases more slowly from the 'thick' sample and peaks at a lower level, most likely because the sample thickness limits the transmission of heat through the sample and therefore the equilibrium temperature of the triphenylene molecules exposed to vacuum. The signal level, and therefore the rate of desorption, decreases only slightly while the laser is on. The thicker layer of triphenylene is also observed to take longer to deplete than the thinner sample.

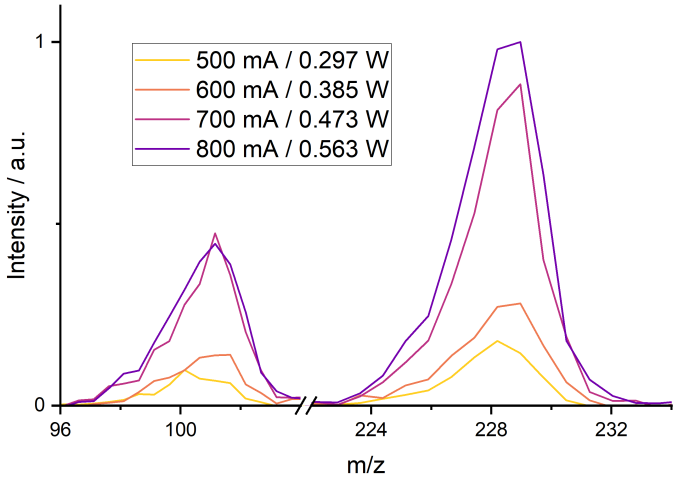
It can be concluded that there is a balance between a higher maximum signal level, which is achieved by thinner samples, and a longer-lasting signal, which is typical of thicker samples. For velocity-map imaging experiments, which often require long periods of data acquisition, thicker samples are more appropriate. These will be used for the remainder of source characterisation and velocity-mapping experiments presented in Chapter 7.

6.3 Generation of intact molecules in the gas phase

There is a risk that excessive heating of the sample will cause triphenylene molecules to dissociate prior to desorption. In order to determine whether this is in fact occuring, mass spectra were recorded at different diode laser powers under spatial-map imaging conditions. Fragment ions may be observed for two reasons. Firstly, the LID source may produce molecular fragments as a result of thermal decomposition, which are then ionised by the electron beam. Alternatively, intact parent molecules that are ionised by the electron beam may dissociate. If thermal decomposition of sample molecules were taking place, one would expect to observe a higher abundance of fragment ions relative to signal ions at higher diode laser powers; as the sample is heated to higher temperatures, decomposition should be more likely.

Figure 6.2 shows the triphenylene parent ion peak, centred at $m/z = 228$, and the $C_8H_x{}^+/C_{16}H_y{}^{2+}$ peak, centred at $m/z = 101$, which is the most abundant fragment signal at an electron energy of 100 eV. Note that the mass resolution of the time-of-flight spectra was insufficient to resolve the number of hydrogens contained by a particular ion. Therefore, the number of hydrogens is not specified in the chemical formulae of ions. By dividing the area under the parent ion peak by the area under the fragment peak, the relative abundances of the two ions at each laser power, which are recorded in Figure 6.2, can be determined.

No clear correlation between the parent:fragment ratio and diode laser power is evident, indicating that thermal decomposition of triphenylene sample molecules is not occuring in a way that will affect data acquisition.



Diode laser power at foil / W	Parent ion:fragment ion intensity ratio
0.297	2.32
0.385	2.23
0.473	2.40
0.563	2.69

Figure 6.2: The $C_8H_x^+/C_{16}H_y^{2+}$ and $C_{18}H_x^+$ peaks in the mass spectrum at different diode laser powers, labelled by the diode current and laser power at the foil. The ratios of the two peak intensities at each laser power are tabulated. Note that the number of hydrogens contained in each fragment is not specified, since the resolution of the mass spectra was insufficient to resolve the number of hydrogens.

6.4 Optimising velocity-mapping conditions

As noted earlier, effective velocity-mapping of product ions relies on there being a sufficiently small interaction region between the electron beam and molecular plume. Therefore, optimising the LID source setup for velocity-mapping focussed on reducing the size of this region. In order to obtain all velocity-map images presented in this section, the repeller and extractor potentials were tuned to achieve the smallest possible parent ion spot, with the optimum potentials determined to be approximately 7.00 kV and 5.06 kV, respectively.

Immediately after LID source installation, there was no physical barrier separat-

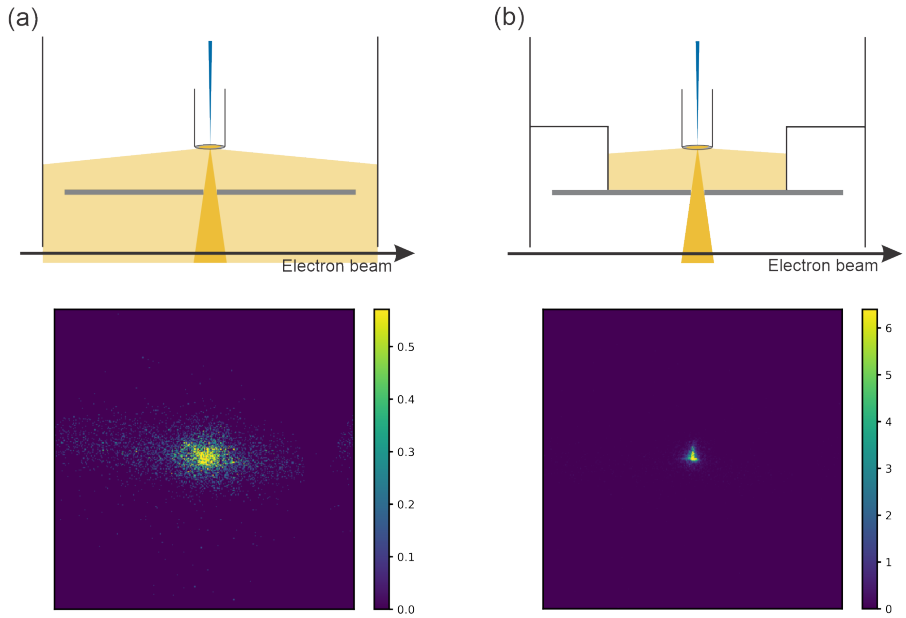


Figure 6.3: Schematic of sample desorption from the LID source tip and corresponding parent ion velocity-map images (a) without any barrier between the source and scattering chambers and (b) with a barrier.

ing the source chamber, within which the LID source is mounted, and the scattering chamber, where electron ionisation and ion extraction takes place. Consequently, molecules generated from the LID source could diffuse around the edge of the repeller plate to the scattering chamber. Figure 6.3(a) shows a parent ion image acquired under these conditions.

A horizontal 'stripe' of intensity is visible in the image, along the length of the electron beam path, resulting from the fact that triphenylene molecules were present at low levels throughout the scattering chamber, not just in the plume that has passed through the hole in the repeller plate. Under these conditions, The velocity focus was insufficent to acquire high-quality velocity-mapping data.

In order to rectify this, a PTFE barrier was installed to prevent molecules from diffusing around the repeller plate into the scattering chamber, with the effect on the parent ion image illustrated in Figure 6.3(b). The velocity focus of triphenylene parent ions is vastly improved, since ionisation is now largely restricted to a region

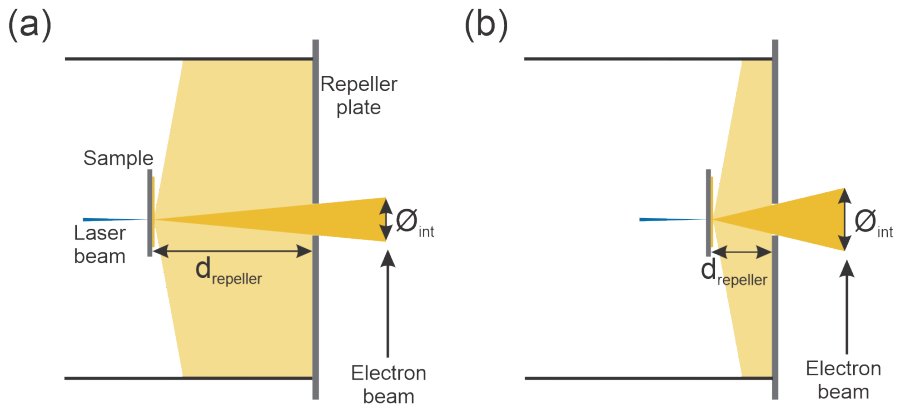


Figure 6.4: Schematic demonstrating the effect of varying the distance between the LID source foil and repeller plate, d_{repeller}, on the size of the electron-molecule interaction region, ϕ_{int}. The interaction region is larger in (b) than in (a) as d_{repeller} is smaller.

that can be effectively velocity-mapped.

Molecules desorbed from the tantalum foil form a diverging plume which is collimated by passing through the central hole in the repeller plate. Figure 6.4 illustrates how the diameter of the interaction region, ϕ_{int}, is affected by the distance between the tantalum foil and the repeller plate, d_{repeller}. At larger d_{repeller} values, the cone of acceptance for molecules that can pass through the repeller plate hole becomes narrower, so ϕ_{int} decreases. This scenario is outlined in figure 6.4(a). As the foil is brought closer to the repeller plate, the cone of acceptance becomes wider, so ϕ_{int} increases.

Velocity-map images of the parent ion and their projections onto the x and y axes are displayed in Figure 6.5 for four different values of d_{repeller}. At a foil-repeller distance of 5 mm, the parent ion image is rather diffuse and irregular in shape. As this distance decreases, the image and its projection onto the two cartesian axes contracts as the interaction region shrinks and the effectiveness of the velocity-mapping improves.

However, as the tantalum foil is withdrawn further from the repeller plate, the ion signal level decreases, since fewer molecules are desorbed with a trajectory that

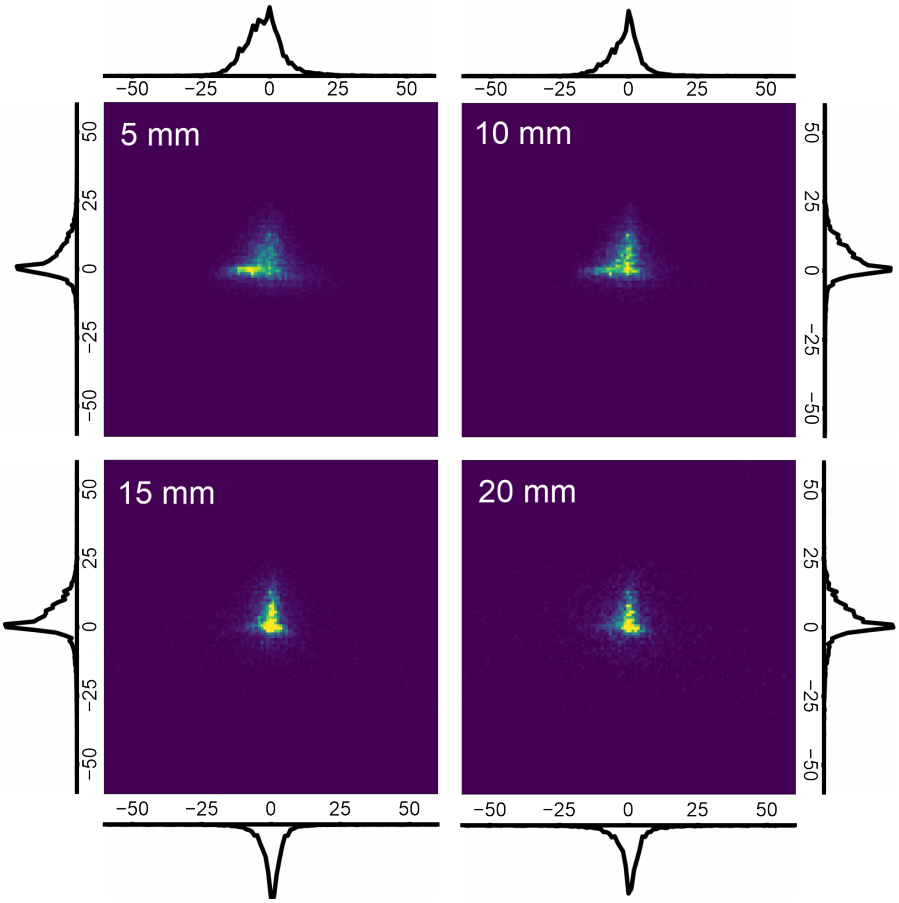


Figure 6.5: Triphenylene$^+$ velocity-map images at four different foil-repeller plate distances. In each case, the image intensity is projected onto the x and y axes in units of pixels.

allows them to enter the interaction region. Therefore, a balance must be struck between improving the quality of the velocity-mapping conditions and ensuring that the signal level is sufficient to gather data within a reasonable time frame and with an acceptable signal-to-noise ratio. For the remainder of the experiments employing the LID source, a foil-repeller distance of 6 mm was used.

6.5 Summary

In summary, this chapter has outlined the work carried out to characterise and optimise the LID source for use on the electron-molecule crossed-beam experiment. Having ensured its suitability, the dissociative electron ionisation of triphenylene

was studied in detail. The results of this work are presented in the next chapter.

7

Dissociative electron ionisation of triphenylene

7.1 Introduction

Polycyclic aromatic hydrocarbons (PAHs) are a class of organic hydrocarbons consisting of fused aromatic rings. They are important both on Earth, where they act as a harmful pollutant,[151,152] and in the interstellar medium, where PAHs are thought to account for approximately 10 - 20% of total galactic carbon.[153,154] Plasma environments exist in both of these setting, so examining the electron-induced fragmentation dynamics of PAHs is relevant in these fields. PAH dissociative ionisation dynamics have previously been studied by extreme ultraviolet (XUV) ionisation at 40.9 eV,[65,66] and strong-field ionisation at 800 nm with ponderomotive energies (i.e. the average kinetic energy of an electron as a result of the laser field)[155,156] in the range of 30 eV to 54 eV.[78] Comparison with this work should elucidate whether the ionisation mechanism affects the ensuing dynamics.

This work focuses on the electron ionisation of triphenylene ($C_{18}H_{12}$), which is a PAH consisting of four fused benzene rings, arranged symmetrically. Its

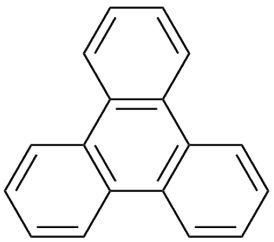


Figure 7.1: Structure of triphenylene.

structure is shown in Figure 7.1

7.2 Methods

A detailed description of the electron-molecule scattering VMI apparatus used to collect the data presented in this chapter can be found in Chapter 2. To summarise, triphenylene (Merck, T82600, 98%) is prepared in the gas phase by the laser-induced desorption (LID) source, which was characterised for use on the electron-molecule crossed-beam experiment in Chapter 6. A thick layer of triphenylene is deposited on 12.5 micrometer Tantalum foil (Goodfellow TA000300) by recrystallisation from hot toluene solvent. A diode laser (Thorlabs L450P1600MM) irradiates the rear of the foil to desorb triphenylene molecules intact. During the acquisition of the results presented in this chapter, the foil was mounted approximately 5 mm behind the repeller plate of the ion lens.

Time-of-flight mass spectra were obtained at various electron energies between 16 eV and 100 eV under spatial-mapping conditions. At each energy, a 'signal' ToF spectrum was recorded with the diode laser irradiating the sample foil, followed by a 'background' mass spectrum, collected with the diode laser switched off, but with all other conditions identical. As the electron gun filament heats up, the electron beam's spatial profile can change and the current can increase. Therefore, peaks in the background mass spectrum are often shifted slightly in temporal position

and are more intense compared to the signal mass spectrum, causing non-physical negative peaks to appear in the background-subtracted mass spectrum. In order to circumvent this problem, the background spectrum is shifted in time and intensity to minimise the negative intensity in the background-subtracted spectrum.

Signal and background velocity-map imaging data were acquired at an electron energy of 100 eV. Images of each product ion were first smoothed by a Gaussian filter with a width of 2 pixels in the x and y directions and then Abel inverted using the BASEX method.

Competing fragmentation mechanisms of multiply-charged parent triphenylene cations disentangled by covariance analysis (see Chapter 3 for a detailed description). Specifically, recoil-frame covariance analysis was used to elucidate the relative velocity distributions of correlated ion pairs. Radial distributions can also be extracted from recoil-frame covariance maps and converted to momentum and kinetic energy distributions for a particular ion pair, by means of a calibration determined in the SIMION package. Contingent covariance analysis was employed in order to minimise any false covariance arising from fluctuations in the electron beam or molecular plume density during the course of the experiment. The data set was also filtered to exclude any large spikes in the signal caused by sudden increases in the desorption rate from the sample foil. This was found to make the contingent covariance algorithm considerably more effective at eliminating false covariance.

7.3 Mass spectra

Background-subtracted mass spectra recorded for several electron energies between 20 eV and 100 eV are displayed in Figure 7.2. Peaks are labelled according to the number of carbon atoms in a fragment, since the mass resolution of the experiment is not sufficient to resolve the number of hydrogen atoms. Throughout this chapter,

fragments labelled as C_x^+ refer to cationic fragments consisting of x carbon atoms and an undefined number of hydrogen atoms. We note that the peak centred at $m/z = 92$ is identified as the toluene parent ion, a residue from the sample preparation process. Since it does not coincide with any fragments of triphenylene, this peak will not be considered further.

The branching ratios for each cationic product were determined by calculating the area under each peak in the mass spectrum at a given electron energy and dividing it by the total peak area. This quantifies the relative probability of forming a specific cationic product at that electron energy. Figure 7.3 presents the branching ratios of selected ions across the mass range, plotted as a function of electron energy between 20 eV and 100 eV.

At 20 eV the parent C_{18}^+ ion peak, centred at $m/z = 228$, dominates the mass spectrum and has a branching ratio close to unity, indicating that fragmentation of the carbon framework is minimal, even at approximately 12 eV above the ionisation energy. This observation confirms that the LID source is generating intact triphenylene molecules in the gas phase and that any fragmentation observed at higher electron energies is a consequence of ionisation. Following ionisation, PAH molecules are known to be robust to fragmentation, especially of the carbon backbone; studies employing XUV, femtosecond infrared and electron ionisation methods have observed dominant signals from parent cations and dications in mass spectra.[65,66,157,158] This stability has been explained in terms of ultrafast non-adiabatic electronic relaxation to form a stable parent cation tending to outcompete the fragmentation of the carbon backbone.

The branching ratio of the parent monocation decreases with increasing electron energy as fragmentation and the formation of multiply-charged ions become increasingly likely. The first fragment ion to appear in the mass spectrum at 25 eV

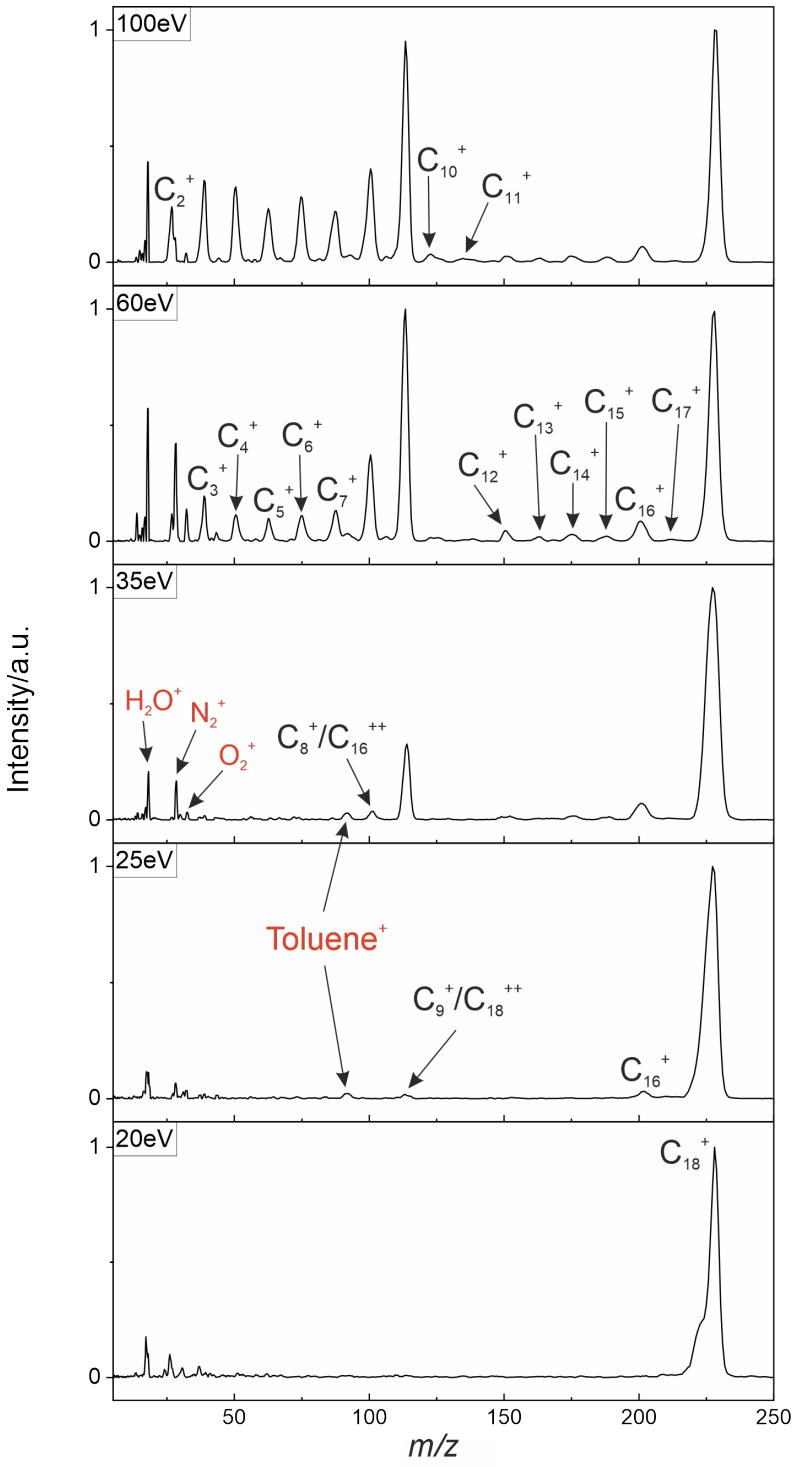


Figure 7.2: Triphenylene mass spectra at various electron energies. Peaks are labelled according to the fragment's number of carbon atoms. Fragment peaks that are not fragment products of triphenylene are labelled in red.

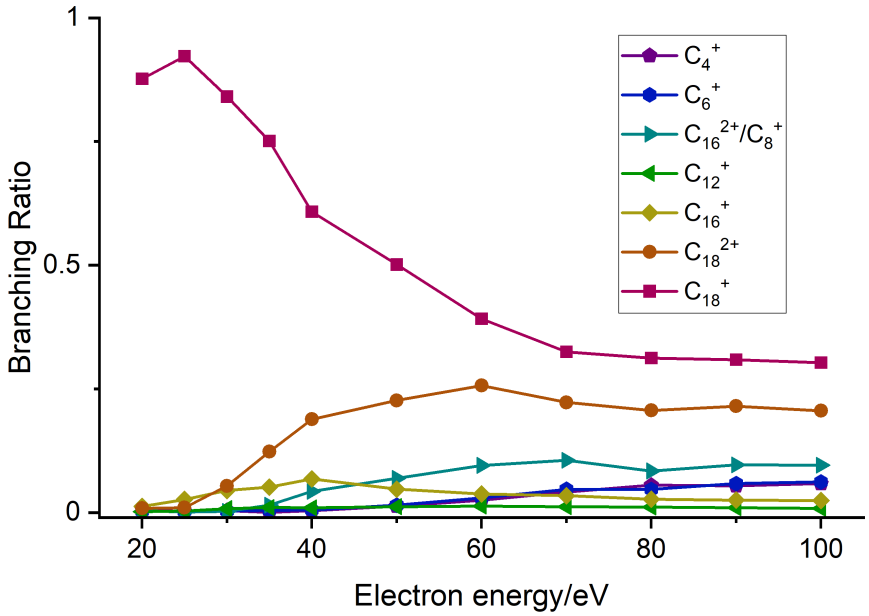


Figure 7.3: Branching ratios for selected product ions produced by triphenylene electron ionisation, plotted at electron energies between 20 eV and 100 eV.

is C_{16}^+ ($m/z = 200$), which is most likely to be formed by the loss of acetylene (C_2H_2) from the parent cation. C_2H_2 loss is a well-known fragmentation pathway of PAH cations, and has been studied both experimentally and computationally.[159–162] Acetylene loss is often preceded by expansion and contraction of the fused aromatic rings, as demonstrated in a computational study by West et al.[161] The reaction mechanisms calculated for anthracene, phenanthrene, tetracene and pyrene were found to proceed via isomerisation to form azulene-containing analogues, after which the seven-membered ring contracted into fused five- and four- membered rings, followed by cleavage of C_2H_2. The mechanism for phenanthrene is shown in Figure 7.4. A similar process occurs when acetylene is lost by the naphthalene cation to form the pentalene cation.[159] In the case of triphenylene, given the possibility for the central six-membered ring to contract to a five-membered ring and one of the outer rings to expand to a seven-membered ring, it is likely that

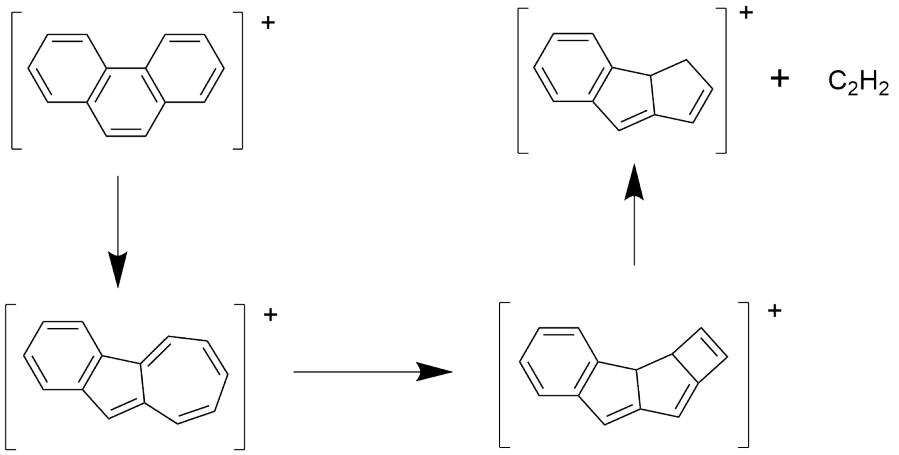


Figure 7.4: Mechanism for acetylene loss from phenanthrene, as proposed by West *et al.*[161]

acetylene loss occurs by an analogous mechanism.

At all electron energies, the C_{16}^+ ion is significantly more abundant than C_{14}^+ and C_{12}^+, indicating that the parent cation generally only has enough internal energy to undergo loss of a single acetlyene fragment, rather than undergoing a series of sequential losses.

The parent dication first appears in the mass spectrum at 25 eV, consistent with the double ionisation potential of 24.1 eV determined by electron ionisation.[157] As the electron energy increases, the branching ratio to form the dication increases. However, as the electron energy increases further it becomes more likely that the dication dissociates, causing the branching ratio to plateau. Possible identities for the peak at $m/z = 100$ are C_{16}^{2+}, the product of acetylene loss from the parent dication, and C_8^+. Figure 7.3 shows the branching ratio of this peak growing in tandem with the parent dication, strongly suggesting that C_{16}^{2+} makes a significant contribution to this signal. As the electron energy increases, the branching ratio of this ion remains noticeably larger than others with m/z values lower than the parent dication, suggesting that C_{18}^{2+} also does not have sufficient energy for sequential acetylene loss to occur. Product channels yielding fragment ions with

smaller mass-to-charge ratios, such as C_4^+, exhibit branching ratios that begin to rise gradually from around 50 eV. These smaller ions are most likely generated in conjunction with another charged fragment following dissociation of a multiply charged parent ion, as their limited ability to delocalise and stabilise charge makes it unlikely that they would emerge as the sole charged product of a dissociation event. The parent trication, C_{18}^{3+}, has the same m/z value as the C_6^+ fragment. Although the triple ionization threshold has not, to the author's knowledge, been reported in the literature, it is highly likely that C_{18}^{3+} is produced at the higher electron energies studied here and thus contributes to the peak labelled C_6^+. However, the intensity of this peak closely follows that of other fragments with similar m/z values, such as C_4^+. This suggests that the trication's contribution remains minor, even at higher energies. Accordingly, the discussion in the remainder of this chapter will focus on the fragmentation of the triphenylene monocation and dication.

7.4 Velocity-map images

Abel-inverted velocity-map images of the product ions formed from the electron ionisation of triphenylene at 100 eV are displayed in Figure 7.5, together with their corresponding kinetic energy distributions. The C^+, C_2^+ and C_{12}^+ fragments overlap with background ions in the mass spectrum, resulting in signal-to-noise ratios too low to yield usable images. Both C_{18}^+ and C_{18}^{2+} ions are born with very little kinetic energy. The only possible formation pathway in either case is the loss of neutral hydrogen atoms from the parent cation or dication, respectively. The large disparity in mass between the triphenylene cation and hydrogen atom means that most of the kinetic energy released in the fragmentation is carried away by hydrogen as a result of the conservation of momentum, yielding slow-moving partner ions that appear in the centre of the velocity-map images.

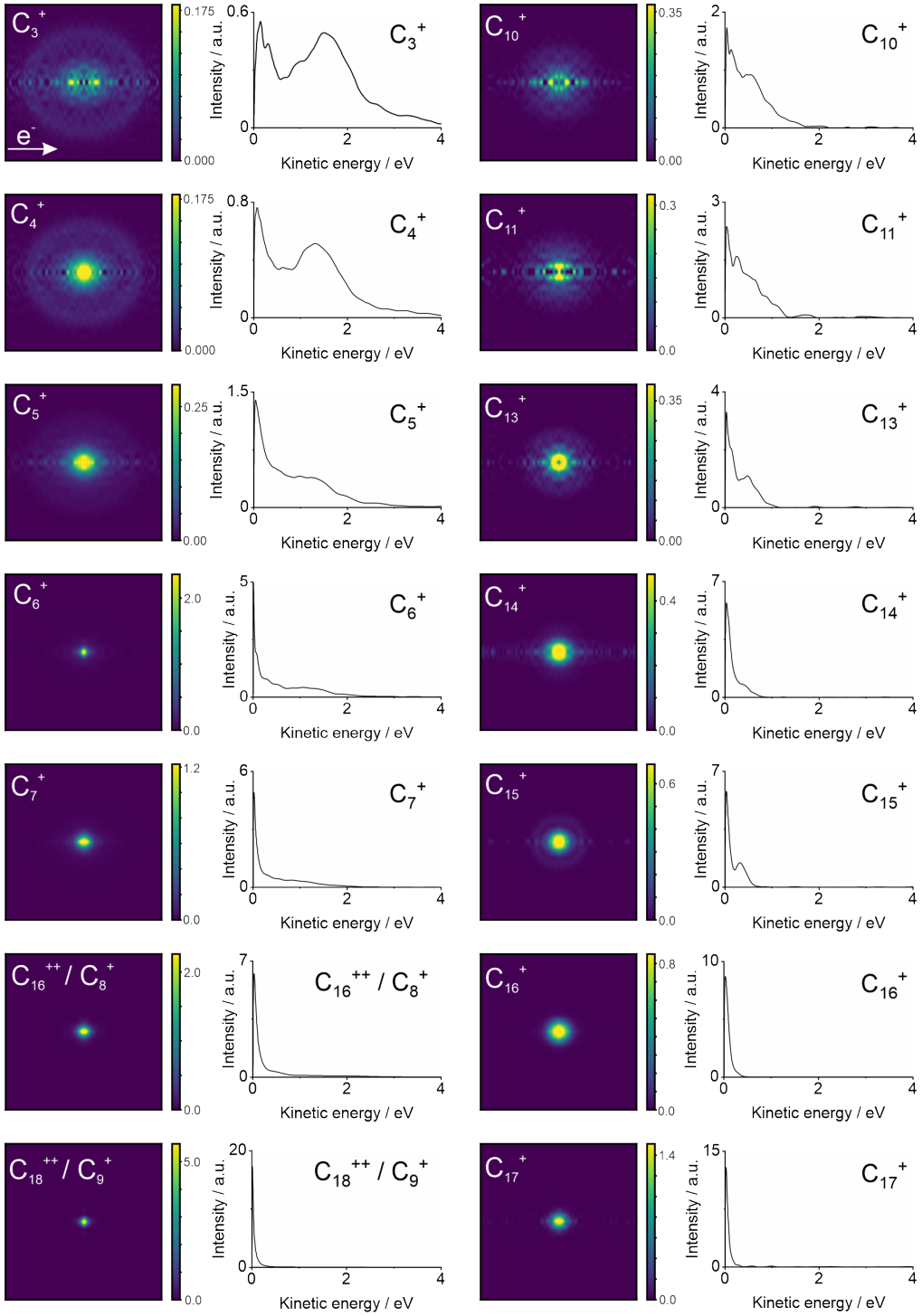


Figure 7.5: BASEX-inverted velocity-map images and corresponding kinetic energy distributions for fragment ions of triphenylene at 100 eV. In all images, the electron beam axis is from left to right.

In general, the remaining ions exhibit two distinct features in their kinetic energy distributions. A low-energy peak arises from daughter ions formed in the the dissociation of singly charged parent cations. This generally occurs via a statistical mechanism, in which the parent ion survives long enough after ionisation for energy to be redistributed among the internal modes of the molecular ion and the daughter ions therefore have a slow, thermal velocity distribution. In contrast, a higher-energy peak is characteristic of daughter ions formed via multiply charged parent ions dissociating in a Coulomb explosion-type process. Coulombic repulsion between charges is the dominant force, causing the two ions to recoil with higher kinetic energy.

Both C_{16}^{+} and C_{16}^{2+} are formed with little kinetic energy, consistent with their formation via loss of a neutral C_2H_2 fragment in a statistical mechanism. In both cases, only one fragment is charged. Together with the requirement that the fused ring system must rearrange prior to the ejection of C_2H_2, this observation is in line with expectations.

Following the dissociation of a singly charged parent ion, the larger fragment is most likely to retain the positive charge. Since larger ions can delocalise charge more effectively, there is likely to be a lower barrier for this process than one in which the smaller ion retains the charge. When a multiply charged ion dissociates in a Coulomb explosion, both fragments retain charge and are detected. Therefore, the low-energy peak corresponding to singly-charged parent ion fragmentation is dominant for larger fragment ions, whereas the high-energy feature from Coulomb-driven fragmentation is more pronounced for smaller ions.

As the fragment mass decreases, its kinetic energy generally increases. This effect is most apparent in the higher-energy peak and is a consequence of momentum conservation. Assuming the parent ion dissociates into two fragments, they recoil

with equal and opposite momenta and the velocity of the lighter fragment is therefore higher. Since kinetic energy scales with the square of velocity, the lighter fragment will recoil with a larger share of the available energy. Consequently, contributions from the dissociation of singly and multiply charged ions are spatially well separated in the case of lighter fragment ions, but not in the case of heavier fragments. To properly disentangle the dissociation mechanisms of multiply-charged ions, covariance analysis is employed.

7.5 Recoil-frame covariance analysis

Recoil-frame covariance maps for all possible pairs of fragment ions whose masses sum to that of the 18-carbon parent ion, are shown as a matrix in Figure 7.6. As outlined previously, ions are labelled according to the number of carbon atoms they contain, so the following discussion is limited to considering how the carbon framework of multiply charged triphenylene ions fragments.

Each square in the matrix shows the recoil-frame covariance map for the (C_x^+, C_y^+) ion pair, where C_x^+ is the signal ion and C_y^+ is the reference ion. The image displays the velocity distribution of the signal ion relative to the reference ion's velocity, which is constrained to lie along a reference direction; throughout this chapter, the reference direction is to the right. Further details on recoil-frame covariance analysis can be found in Section 3.5. All maps are plotted with identical contrast, such that the relative intensity of an image reflects the relative probability of a particular pair of ionic products being formed together.

All simple two-body fragmentation channels of C_{18}^{2+} appear along the top-left to bottom-right diagonal of the figure. As an example, Inset (a) of Figure 7.6 shows the image for the (C_{14}^+, C_4^+) channel, which corresponds to the fragmentation

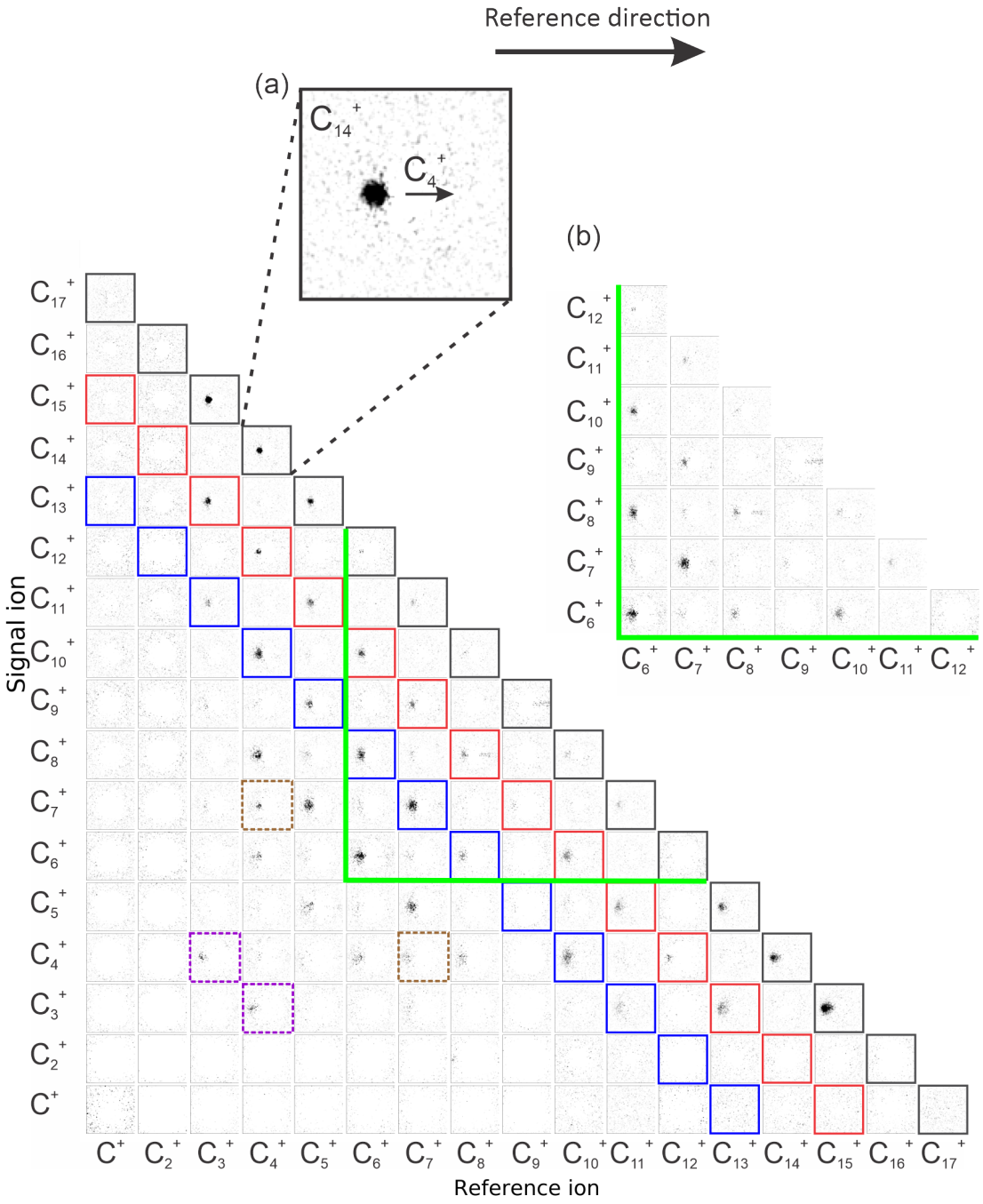


Figure 7.6: Matrix of recoil-frame covariance maps for all possible combinations of signal and reference ions following the electron ionisation of triphenylene at 100 eV. The reference direction is to the right. The images are labelled according to the number of carbon atom that fragment ions contain. All images have been plotted to the same contrast. Inset (a) displays the covariance map for the (C_{14}^+, C_4^+) channel. Inset (b) and all coloured sqaures show features of the matrix for further discussion.

$$C_{18}^{+} \longrightarrow C_{14}^{+} + C_{4}^{+} \tag{7.1}$$

The recoil-frame covariance map exhibits a sharp signal in the direction opposite to the reference direction, consistent with the two fragments recoiling in opposite directions in accordance with momentum conservation.

Closer inspection of the diagonal reveals that the central covariance-map images, corresponding to channels for which both fragments have similar masses, are markedly less intense than those towards the edges, where the fragment masses differ significantly. One possible explanation is that whilst all two-body dissociations occur with similar probability, the likelihood of subsequent fragmentation depends on fragment mass. Heavier fragments, such as C_{15}^{+}, are less likely to undergo secondary fragmentation than lighter fragments, such as C_{9}^{+}, owing to greater charge delocalisation and stabilisation. This interpretation is supported by the section of the matrix displayed in inset (b) of Figure 7.6 (outlined in green). Whilst the images along the diagonal are faint, the other off-diagonal images in this section, which may result from the two fragments undergoing further dissociation, are more intense.

Covariance images for the (C_{16}^{+}, C_{2}^{+}) and (C_{17}^{+}, C^{+}) product pairs show minimal intensity, indicating that these are very minor two-body fragmentation channels. Although C_{16}^{+} and C_{17}^{+} are large fragments, their co-fragments, C_{2}^{+} and C^{+}, are small. Therefore, the barrier to this fragmentation channel may be prohibitive. Indeed, all covariance maps involving C_{2}^{+} or C^{+} show minimal intensity, supporting this interpretation. As a consequence, C_{16}^{+} and C_{17}^{+} are formed predominantly through dissociation of the parent monocation. For C_{16}^{+}, this occurs via the loss of neutral acetylene, as discussed earlier. The velocity-map images for these products support this, yielding kinetic energy distributions

Signal ion, reference ion	Mean projected momentum / 10^{-22} kg ms^{-1}	FWHM / 10^{-23} kg ms^{-1}
C_3^+, C_{15}^+	2.18	6.05
C_4^+, C_{14}^+	2.46	7.47
C_5^+, C_{13}^+	2.72	7.78
C_7^+, C_{11}^+	2.87	10.7

Table 7.1: Parameters obtained from fitting the projected momentum distributions of various two-body recoil-frame covariance maps with a Gaussian function. The (C_6^+, C_{12}^+) product pair is excluded due to the inadequate signal-to-noise of this covariance image.

dominated by a low energy feature characteristic of monocation fragmentation.

The dynamics of two-body fragmentation can be considered further by extracting momentum distributions from the covariance maps. These distributions correspond to the momentum of the designated signal ion of the two-body fragmentation in question, which, by conservation of momentum, will be equal in magnitude to the momentum of the reference ion. It is important to note that since covariance maps are calculated from velocity-map images that are 2D projections of the full 3D product scattering distribution, momentum or velocity distributions extracted from recoil-frame covariance maps are not 'true' distributions. Instead, they can be considered as 'projected' distributions. Although methods have been developed to invert these covariance maps, the signal-to-noise ratios of many of the images presented in this chapter were insufficient to obtain inverted images.[26] Despite this, analysis of these distributions still allows for a qualitative comparison between fragmentation channels. A Gaussian fit was applied to various two-body projected momentum distributions, with the resulting parameters listed in Table 7.1.

To a first approximation, the energetics of these two-body dissociations can be considered as a Coulomb explosion, driven only by Coulomb repulsion between the two positively charged fragments, which are considered as point charges. The potential energy, E, of this interaction is given by Coulomb's Law:

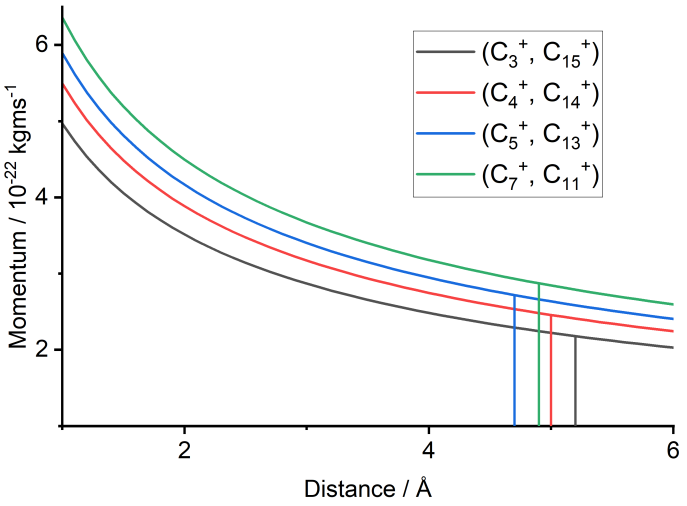


Figure 7.7: The final projected momenta of different product ion pairs, plotted as a function of the initial separation between the two point charges.

$$E = \frac{q_1 q_2}{4\pi\epsilon_0 r} \tag{7.2}$$

where q_1 and q_2 are the charges on the two fragments, ϵ_0 is the permittivity of free space and r is the distance between the charges. By conservation of momentum and assuming all potential energy is transferred to kinetic energy of the fragments, it can be shown that the momentum, p, of each fragment is given by

$$p = \sqrt{\frac{\mu q_1 q_2}{2\pi\epsilon_0 r}} \tag{7.3}$$

where μ is the reduced mass of the two fragments. The final momenta of the two fragments can be plotted as a function of the initial separation between the two point charges, as shown in Figure 7.7 for each of the product pairs listed in Table 7.1.

Using the mean projected momenta obtained from the covariance maps, the separation between the two point charges in each product pair can be read off the plot in Figure 7.7, or found by rearranging Equation 7.3. The calculated distances, which are marked by vertical lines in Figure 7.7, range from 4.7 Å in the case

of (C_5^+, C_{13}^+) to 5.2 Å in the case of (C_3^+, C_{15}^+) and cluster around 5 Å. For comparison, the maximum separation between two carbon atoms in triphenylene is 7.13 Å. The fact that the calculated charge separations are a good match with the molecular size supports the use of a Coulomb explosion model as a reasonable first-order approximation for describing two-body fragmentation dynamics. Indeed, the experimentally determined charge separations can be expected to be somewhat smaller than the maximum carbon separation, since in reality charge is widely delocalised across the structure of the ion, rather than localised at the edges. Similar charge separations have been reported in experiments studying the strong-field ionisation of triphenylene,[78] suggesting that the Coulomb model is applicable regardless of the ionisation mechanism under study.

More complex, multi-step fragmentation mechanisms play a significant role in the fragmentation of triphenylene dications, as evidenced by the signals observed in the off-diagonal covariance maps in Figure 7.6. In addition to producing two charged fragments, these pathways also generate at least one neutral fragment that is not detected. An understanding of the overall mechanism can be constructed by close inspection of the covariance maps corresponding to the two charged fragments.

Inspecting the relative intensities of covariance maps uncovers a clear pattern. Covariance maps for ion pairs with masses that sum to that of 16 carbons, highlighted by black squares, show pronounced intensity. This strongly suggests the production of a neutral C_2 acetylene fragment. Similarly intense covariance images are observed for ion pairs with total masses that differ from the parent ion mass by multiples of two carbons. For example, channels for which the fragment ion masses sum to 16 carbon atoms (highlighted by red squares) show strong intensity, as do those summing to 14 carbon masses (highlighted by blue squares).

In general, covariance maps corresponding to pairs of fragments with an even

Signal ion, reference ion	Mean projected velocity / ms^{-1}	FWHM / ms^{-1}
C_{14}^+, C_4^+	2.18	6.05
C_{12}^+, C_4^+	2.46	7.47
C_{10}^+, C_4^+	2.72	7.78

Table 7.2: Parameters obtained from fitting the projected velocity distributions of several two-body recoil-frame covariance maps in which C_4^+ is the reference ion with a Gaussian functions.

total number of carbons show well-defined covariance signals, whereas those with an odd total display minimal covariance intensity. The propensity for PAH cations to undergo acetylene loss has already been established, so it is not surprising that the C_2 fragment is a common neutral fragment in the many-body dissociation of dications.

The HACA (hydrogen abstraction C_2H_2 addition) mechanism is proposed as a key pathway for PAH growth in the interstellar medium: hydrogen abstraction generates reactive sites on aromatic molecules, which then undergo acetylene addition to expand the carbon framework and enable new ring formation. Here, acetylene fragments are lost from, rather than added to, the structure in a 'reverse-HACA' process. These observations suggest that acetylene addition is a reversible process, consistent with the reported low activation barrier.[163] Similar fragmentation patterns have been observed following strong-field and XUV ionisation, strongly suggesting that this process is independent of the ionisation mechanism.

In order to understand the dynamics of these many-body dissociations in more detail, the covariance maps for a series of signal ions correlated with reference ion C_4^+, will now be considered in greater depth as an illustrative example.

The left-hand side of Figure 7.8 presents these covariance maps alongside the corresponding projected velocity distributions. These have been fitted with Gaussians to extract quantitative information, presented in Table 7.2.

As noted previously, the two charged fragments in the (C_{14}^+, C_4^+) ion pair recoil in opposite directions due to momentum conservation; accordingly the C_{14}^+

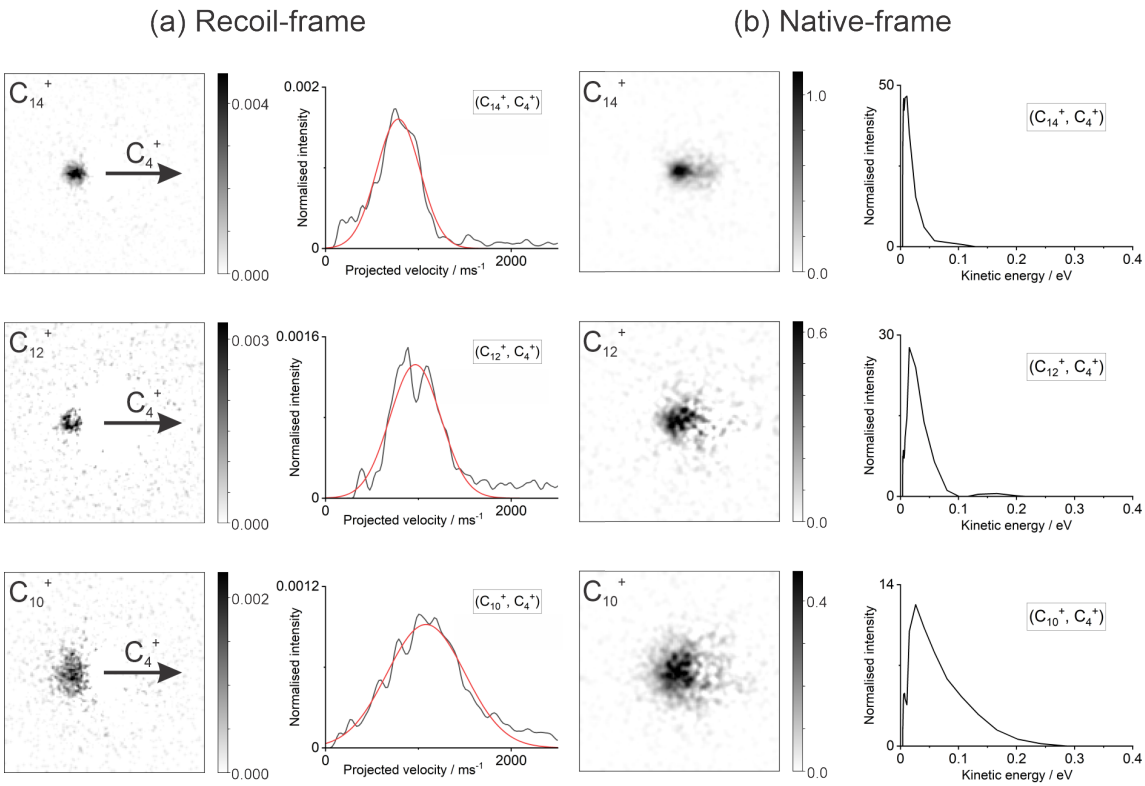


Figure 7.8: (a) Recoil-frame covariance maps for a series of signal ions correlated with reference ion C_4^+, displayed with the associated projected velocity distribution. The corresponding native-frame images are shown in (b). Associated kinetic energy distributions are found by inverting the native frame image using the BASEX method.

signal appears opposite to the reference direction in the covariance-map image. Loss of hydrogen atoms from either fragment does little to blur the image as most of the kinetic energy released in such processes is carried away by the light hydrogen atoms. The covariance signal for the (C_{12}^+, C_4^+) ion pair appears somewhat blurred relative to that for (C_{14}^+, C_4^+), with a broader velocity distribution. This broadening reflects the small velocity 'kick' imparted as C_2 is lost in a random direction from the C_{14}^+ primary dissociation product. The (C_{10}^+, C_4^+) channel exhibits an even broader velocity distribution, consistent with the additional random impulse arising from the loss of a second C_2 fragment.

The multi-step mechanism is therefore proposed to begin with an initial charge separation of the parent dication into two charged fragments, C_{14}^+ and C_4^+. C_{14}^+

then loses one or more neutral C_2 fragments. These steps are summarised in Equations 7.4 to 7.6.

$$C_{18}{}^{2+} \longrightarrow C_{14}{}^{+} + C_4{}^{+} \tag{7.4}$$

$$C_{14}{}^{+} \longrightarrow C_{12}{}^{+} + C_2 \tag{7.5}$$

$$C_{12}{}^{+} \longrightarrow C_{10}{}^{+} + C_2 \tag{7.6}$$

Native-frame analysis allows the acetylene-loss steps to be considered in the centre-of-mass (native) frame of the $C_{14}{}^{+}$ intermediate by subtracting its momentum from the recoil-frame covariance image. Although $C_{14}{}^{+}$ itself is not detected directly, its momentum can be determined from the C_4^+ co-fragment, which must have a momentum equal in magnitude and opposite in direction. The resulting images and corresponding kinetic energy distributions, shown on the right-hand side of figure 7.8, are found to be centred on the origin. This confirms that $C_{14}{}^{+}$ is the product of the initial charge separation in each case and the precursor ion for the subsequent C_2 loss steps. The isotropic angular distributions indicate that $C_{14}{}^{+}$ on average survives for longer than one rotational period, so the C_2 fragments are ejected in a random direction.

Intensity in the ($C_{14}{}^{+}$, $C_4{}^{+}$) image is concentrated close to the centre, since no further dissociation of the carbon framework occurs after the initial step. In contrast, the ($C_{12}{}^{+}$, $C_4{}^{+}$) and ($C_{10}{}^{+}$, $C_4{}^{+}$) images appear increasingly diffuse, and their kinetic energy distributions extend to higher values as each successive C_2 loss imparts an additional "kick" to the surviving fragment.

The mean of the projected velocity distribution increases slightly as more C_2 fragments are lost. One possible interpretation is that those $C_{14}{}^{+}$ ions formed with greater velocity from the initial step are more likely to lose C_2 fragments.

At first, this may seem surprising, since one would expect those ions with lower velocity to have more internal energy. However, the observed trend can be justified as follows. At least two bonds in the carbon skeleton of the parent ion must be broken before the initial charge separation step can take place. These bonds may not break simultaneously; instead, one bond may rupture first, leading to structural unfolding before the final bond breaks and the two charged fragments recoil in a Coulomb explosion. Under this model, the kinetic energy release of the Coulomb explosion would depend on the separation of the charges and therefore the extent of unfolding after the first bond breaks. Ions that receive a larger velocity 'kick' from this first step are likely to be more internally vibrationally excited; more energy would be available to overcome the barrier to C_2 loss and the structure may undergo less unfolding prior to dissociation.

7.6 Summary

The fragmentation dynamics of triphenylene following electron ionisation have been investigated by mass spectrometry, velocity-map imaging, and recoil-frame covariance analysis. Several key results have emerged. Dissociation of the parent monocation proceeds predominantly via statistical loss of a single acetylene fragment. In contrast, fragmentation of dications is often driven by charge separation through a Coulomb explosion. Subsequent acetylene loss, typically from the larger charged fragment, follows a pathway reminiscent of a 'reverse HACA' mechanism. These findings closely resemble the dissociative ionisation dynamics observed after XUV ionisation at 40.9 eV and strong-field ionisation at ponderomotive energies between 30 eV and 54 eV, suggesting that fragmentation pathways are largely independent of the ionisation method. Thus, it is likely that dissociation of the carbon skeleton occurs on potential energy surfaces with a similar characteristic topography, resulting

in analogous fragmentation dynamics in each case. Non-adiabatic coupling means that relaxation of electronically excited PAH cations is efficient and rapid.[65,164,165] As a consequence, it may be that dissociation occurs primarily from a small number of low-lying electronic states of the parent cation or dication.

8 Conclusion and outlook

8.1 Conclusion

Chapters 4 and 5 of this thesis reported data on the dissociative electron ionisation of gaseous halocarbon compounds at low electron energies. The dissociation pathways active at each electron energy were identified by time-of-flight mass spectrometry, and bond dissociation dynamics were characterised by velocity-map imaging measurements. By restricting the electron beam energy to values close to the ionisation threshold of the molecule under study, the number of electronic states in which the nascent parent cation could be formed was significantly limited. Incremental increases in electron energy allowed changes in dissociation dynamics to be correlated with the population of specific electronic states of the parent cation.

Chapter 4 examines the dissociative electron ionisation of trifluoroiodomethane (CF_3I), which exhibits distinct carbon–iodine and carbon–fluorine bond dissociation dynamics that depend on the initial electronic state of the parent cation. Formation of CF_3^+ via carbon-iodine bond fragmentation is characterised by a low kinetic energy release, indicating that this channel proceeds predominantly via a statistical

mechanism from vibrationally excited levels of the electronic ground state of CF_3I^+. A minor contribution from dissociation on the repulsive $\tilde{A}$ state of CF_3I^+ becomes apparent at electron energies above 14 eV. In contrast, carbon-iodine bond dissociation yielding I^+ is dominated by the impulsive dissociation of CF_3I^+ cations in the $\tilde{A}$ electronic state. As the electron energy increases, contributions from higher-lying electronic states of CF_3I^+ manifest as an increasingly pronounced high-energy tail in the I^+ TKER distributions. Fitting of these TKER distributions to a linear combination of Gaussian functions, in conjunction with comparisons to previous photoionisation studies, suggests that this high-energy component arises from dissociation of CF_3I^+ via the $\tilde{D}$ and $\tilde{E}$ electronic states. CF_2I^+ production via carbon-fluorine bond fragmentation was found to occur impulsively impulsive, with an associated release of kinetic energy of between 0.7 and 0.9 eV. This observation is consistent with the dissociation of CF_3I^+ cations in the $\tilde{B}$, $\tilde{C}$ and $\tilde{D}$ electronic states.

Chapter 5 explores the dissociative electron ionisation dynamics of methyl fluoride (CH_3F) and methyl chloride (CH_3Cl) at low electron energies. For CH_3F, carbon-fluorine bond fragmentation yielding the $CH_3{}^+$ product ion occurs via two distinctive mechanisms, depending on the electron energy. At electron energies up to 15 eV, dissociation is dominated by a statistical mechanism involving vibrationally excited CH_3F^+ in the electronic ground state. This is characterised by a low release of kinetic energy. Although this statistical mechanism remains evident at higher electron energies, above 17 eV the $CH_3{}^+$ TKER distributions are dominated by a peak at higher kinetic energy corresponding to dissociation on the repulsive CH_3F^+ $\tilde{A}$ state. Carbon-chlorine bond dissociation in CH_3Cl yielding $CH_3{}^+$ also proceeds via statistical and impulsive pathways. However, in this case the impulsive mechanism from the CH_3Cl^+ $\tilde{A}$ state dominates across the full range of electron energies studied.

Notably, for both CH_3F and CH_3Cl, the $CH_3{}^+$ TKER distributions differ very

little between electron energies of 20 eV and hundreds of eV. This observation strongly suggests that any parent ions initially formed in highly excited electronic states undergo rapid relaxation to low-lying electronic states prior to dissociation.

Both CH_3F and CH_3Cl exhibit anisotropic CH_3^+ scattering distributions. To date, these are the only data sets acquired on the electron-molecule crossed beam apparatus that show such anisotropy. This behaviour can be rationalised in terms of the molecular dipole moment and the asymmetric spatial distribution of molecular orbitals, which result in a larger ionisation cross-section at the methyl group than at the fluorine atom. Consequently, an incident electron is more likely to ionise the molecule if it approaches the methyl end. Since carbon–halogen bond fragmentation proceeds via a rapid impulsive mechanism in both systems, this dependence on molecular orientation is preserved in ion scattering distributions at higher radii, as the molecule dissociates before significant rotation can take place.

In order to extend dissociative electron ionisation studies to larger molecules that are solid at room temperature, a laser-induced desorption (LID) source was installed on the electron-molecule crossed beam instrument. Chapter 6 details the characterisation and optimisation of this source for use on this apparatus. Whilst the LID source design has been characterised previously by Milešević *et al.* for use on a photoionisation velocity-map imaging experiment,[77] this work identified that the presence of desorbed sample molecules throughout the chamber hindered velocity-map imaging conditions. In order to address this, a physical barrier was installed so that sample molecules could only enter the interaction region through an aperture in the repeller plate.

Finally, the LID source was employed to study the dissociative electron ionisation of triphenylene, a polycyclic aromatic hydrocarbon (PAH), with results reported in Chapter 7. Relative branching ratios of fragmentation pathways were determined

from time-of-flight mass spectra over a broad range of electron energies up to 100 eV. These data reveal a propensity of the parent cation and dication to lose neutral acetylene (C_2H_2) fragments. Singly-charged parent ions dissociate predominantly via a statistical mechanism, producing larger daughter ions with small associated kinetic energy releases. In contrast, smaller fragment ions are primarily formed through the impulsive fragmentation of multiply-charged parent ions, driven by Coulomb repulsion between positive charges.

Recoil-frame covariance analysis was used to disentangle the competing fragmentation pathways of multiply-charged triphenylene ions at an electron energy of 100 eV. These results reveal a general dissociation mechanism in which the triphenylene dication undergoes an initial dissociation forming two charged fragments, after which the larger of the two ions loses one or more neutral acetylene fragments. This mechanism resembles the reverse of the HACA (hydrogen abstraction C_2H_2 addition) process, which is proposed as a key PAH growth mechanism in the interstellar medium. The observation of this "reverse-HACA" process following electron impact ionisation is consistent with previous studies using X-ray and strong-field ionisation, suggesting that the underlying dissociation dynamics of PAHs are largely independent of the ionisation method.

8.2 Outlook

8.2.1 New electron source

As discussed in Chapter 2, the commercial electron source used throughout this thesis is limited by the spread of electron kinetic energies in the beam it generates. This complicates data analysis, particularly when attempting to disentangle the contributions of individual electronic states of a parent ion to the observed dissociation. In practice, electronic states can be populated even when their ionisation

thresholds lie above the electron beam's nominal kinetic energy, hindering the assignment of state-specific fragmentation pathways.

One approach to mitigating this issue would be the installation of a custom-built electron source capable of generating a beam with a narrower energy distribution. A well-established example of such a source is the *trochoidal electron monochromator* (TEM). First introduced by Stamatovic and Schulz[166,167] the TEM exploits electron motion in crossed electric and magnetic fields to produce a highly monochromatic electron beam. In this device, a beam of electrons confined by a collinear magnetic field enters a region between two parallel planar electrodes that generate a homogeneous electric field perpendicular to the magnetic field. The combined effect of these fields causes electrons to follow trochoidal trajectories with a deflection perpendicular to both the electric and magnetic fields. Only those electrons with velocities in the propagation axis within a narrow range are able to exit the crossed field region through an aperture.[168,169] As a result, TEMs are capable of producing electron beams with energy resolutions as fine as 20 meV.[167]

The incorporation of a TEM into the electron–molecule crossed-beam apparatus would enable ion appearance potentials to be measured with greater precision. Furthermore, TEMs are able to generate collimated electron beams with kinetic energies below 10 eV. Such a capability would allow dissociative electron attachment to be investigated on the electron-molecule crossed beam experiment.

8.2.2 Measuring the kinetic energy of outgoing electrons

One of the primary motivations for investigating the dissociative electron ionisation of simple halocarbons at low electron energies in Chapters 4 and 5 was to resolve the contributions from low-lying electronic states of the parent cation to the ensuing dissociation dynamics. Although the electronic states involved could

be identified in most cases, these assignments often relied on comparisons with previous photoionisation studies. In the current configuration of the electron-molecule crossed beam apparatus, the kinetic energy of outgoing electrons from ionisation cannot be measured, preventing the energy transferred to the molecule during ionisation from being determined directly.

Electron momentum spectroscopy (EMS) is a technique that measures the momentum and thus kinetic energy of the scattered and ionised electron from an electron ionisation event in coincidence.[170,171] Developing a way to record product ions in coincidence with outgoing electrons would allow the initial state of the parent cation to be assigned definitively.

8.2.3 Orienting molecules in the molecular beam

The velocity-map imaging results presented in Chapter 5 reveal a dependence of electron ionisation on the molecule's orientation relative to the incoming electron. At present, molecules in the molecular beam are randomly oriented in the laboratory frame. Orienting molecules prior to interaction with the electron beam would allow the effect of molecular orientation relative to the incident electron to be studied in greater detail for a large range of molecules with a dipole moment. Such an approach may be capable of observing orientation effects in cases where the effect is too subtle to be resolved in the scattering distributions obtained from randomly oriented parent molecules.

One method of implementing this capability is to use a hexapole state selector to select molecules according to their rotational state, followed by orientation in a homogeneous field between two planar electrodes.[172] This approach has previously been employed by Aitken *et al.* to study the electron ionisation of oriented molecules; however, those experiments used a quadrupole mass spectrometer to detect ions.[51,52]

Adopting this approach on the present instrument would allow this work to be extended to ion imaging detection.

Bibliography

[1] H. Voss *et al.*, Nature **312**, 740 (1984).

[2] M. Sinnhuber and B. Funke, Energetic electron precipitation into the atmosphere, in *The dynamic loss of Earth's radiation belts*, pp. 279–321, Elsevier, 2020.

[3] I. Mironova, G. Kovaltsov, A. Mishev, and A. Artamonov, Remote Sensing **13**, 4161 (2021).

[4] L. Campbell and M. Brunger, International Reviews in Physical Chemistry **35**, 297 (2016).

[5] M. Padovani, D. Galli, and A. E. Glassgold, Astronomy & Astrophysics **501**, 619 (2009).

[6] N. J. Mason, B. Nair, S. Jheeta, and E. Szymańska, Faraday Discussions **168**, 235 (2014).

[7] L. Sanche, The European Physical Journal D-Atomic, Molecular, Optical and Plasma Physics **35**, 367 (2005).

[8] B. Boudaıffa, P. Cloutier, D. Hunting, M. A. Huels, and L. Sanche, Science **287**, 1658 (2000).

[9] M. A. Huels, B. Boudaïffa, P. Cloutier, D. Hunting, and L. Sanche, Journal of the American Chemical Society **125**, 4467 (2003).

[10] A. J. Dempster, Physical Review **11**, 316 (1918).

[11] J. Hajšlová and T. Čajka, Chapter 12 - gas chromatography–mass spectrometry (gc–ms), in *Food Toxicants Analysis*, edited by Y. Picó, pp. 419–473, Elsevier, Amsterdam, 2007.

[12] L. G. Christophorou and J. K. Olthoff, *Fundamental Electron-Molecule Interactions and Their Technological Significance* (Springer US, Boston, MA, 2004), pp. 1–59.

[13] S. Motlagh and J. H. Moore, The Journal of chemical physics **109**, 432 (1998).

[14] D. L. Flamm, V. M. Donnelly, and D. E. Ibbotson, Journal of Vacuum Science & Technology B: Microelectronics Processing and Phenomena **1**, 23 (1983).

[15] P. Harland and C. Vallance, Advances in Gas Phase Ion Chemistry **3** (1998).

[16] S. Ptasinska, M. T. d. N. Varella, M. A. Khakoo, D. S. Slaughter, and S. Denifl, The European Physical Journal D **76**, 179 (2022).

[17] V. Laporta, J. Tennyson, and R. Celiberto, Plasma Sources Science and Technology **25**, 06LT02 (2016).

[18] D. C. Cartwright and A. Kuppermann, Physical Review **163**, 86 (1967).

[19] C. Beenakker, F. De Heer, H. Krop, and G. Möhlmann, Chemical Physics **6**, 445 (1974).

[20] L. Campbell and M. Brunger, International Reviews in Physical Chemistry **35**, 297 (2016).

[21] X.-f. Gao, H. Li, X. Meng, and S.-x. Tian, Chinese Journal of Chemical Physics **32**, 89 (2019).

[22] S. Harper, P. Calandra, and S. D. Price, Physical Chemistry Chemical Physics **3**, 741 (2001).

[23] B. P. Marinković *et al.*, Physica Scripta (2025).

[24] L. G. Christophorou and J. K. Olthoff, (2012).

[25] K. Tanzer *et al.*, The Journal of Physical Chemistry A **119**, 6668 (2015).

[26] D. Heathcote, *Electron-induced Dynamics of Small Molecules of Atmospheric and Astrochemical Relevance*, PhD thesis, University of Oxford, 2020.

[27] M. Dantus, R. M. Bowman, and A. H. Zewail, Nature **343**, 737 (1990).

[28] P. Atkins and J. de Paula, *Atkins' Physical Chemistry*, 8 ed. (Oxford University Press, Oxford, 2006).

[29] J. N. Bull, J. W. Lee, and C. Vallance, Physical Review A **91**, 022704 (2015).

[30] R. Signorell and F. Merkt, Molecular Physics **92**, 793 (1997).

[31] J. Xie and R. N. Zare, The Journal of chemical physics **93**, 3033 (1990).

[32] H. Köckert *et al.*, Physical Chemistry Chemical Physics **21**, 14296 (2019).

[33] P. Persson, S. Lunell, A. Szöke, B. Ziaja, and J. Hajdu, Protein Science **10**, 2480 (2001).

[34] F. Read, Radiation Research **64**, 23 (1975).

[35] G. H. Field and J. L. Franklin, *Electron impact phenomena: And the properties of gaseous ions* (Academic Press, 1970).

[36] H. D. Hagstrum, Mass spectroscopy in physics research, in *National Bureau of Standards Circular No. 522*, p. 193, National Bureau of Standards, Washington, D.C., 1953.

[37] P. T. Smith, Physical Review **36**, 1293 (1930).

[38] D. Rapp and P. Englander-Golden, The Journal of Chemical Physics **43**, 1464 (1965).

[39] W. Zhou, L. Wilkinson, J. W. Lee, D. Heathcote, and C. Vallance, Molecular Physics **117**, 3066 (2019).

[40] H. Deutsch and T. Märk, International journal of mass spectrometry and ion processes **79**, R1 (1987).

[41] D. Margreiter, H. Deutsch, M. Schmidt, and T. Märk, International journal of mass spectrometry and ion processes **100**, 157 (1990).

[42] H. Deutsch, K. Becker, S. Matt, and T. Märk, International Journal of Mass Spectrometry **197**, 37 (2000).

[43] W. Hwang, Y.-K. Kim, and M. E. Rudd, The Journal of chemical physics **104**, 2956 (1996).

[44] T. Märk, Beiträge aus der Plasmaphysik **22**, 257 (1982).

[45] M. Bruoard and C. Vallance, *Tutorials in Molecular Reaction Dynamics* (Cambridge: RSC Publishing, 2010).

[46] F. Jensen, *Introduction to Computational Chemistry* (John wiley & sons, 2017).

[47] D. H. Parker and A. T. J. B. Eppink, (Cambridge University Press, 2003), p. 20–64.

[48] P. C. Samartzis, I. Sakellariou, T. Gougousi, and T. N. Kitsopoulos, The Journal of chemical physics **107**, 43 (1997).

[49] E. Szymańska, V. S. Prabhudesai, N. J. Mason, and E. Krishnakumar, Physical Chemistry Chemical Physics **15**, 998 (2013).

[50] J. N. Bull, J. W. Lee, and C. Vallance, Physical Review A **96**, 042704 (2017).

[51] C. G. Aitken, D. A. Blunt, and P. W. Harland, The Journal of chemical physics **101**, 11074 (1994).

[52] C. G. Aitken, D. A. Blunt, and P. W. Harland, International journal of mass spectrometry and ion processes **149**, 279 (1995).

[53] D. W. Chandler and P. L. Houston, The Journal of chemical physics **87**, 1445 (1987).

[54] D. W. Chandler and P. L. Houston, The Journal of chemical physics **87**, 1445 (1987).

[55] A. T. Eppink and D. H. Parker, Review of Scientific Instruments **68**, 3477 (1997).

[56] C. Vallance, Chemical communications **55**, 6336 (2019).

[57] A. T. J. B. Eppink, S.-M. Wu, and B. J. Whitaker, (Cambridge University Press, 2003), p. 65–112.

[58] C. R. Gebhardt, T. P. Rakitzis, P. C. Samartzis, V. Ladopoulos, and T. N. Kitsopoulos, Review of Scientific Instruments **72**, 3848 (2001).

[59] D. Townsend, M. P. Minitti, and A. G. Suits, Review of scientific instruments **74**, 2530 (2003).

[60] J. W. Lee *et al.*, Communications Chemistry **3**, 72 (2020).

[61] C. Vallance, Molecular Reaction Dynamics lecture course, University of Oxford, Department of Chemistry, 2023.

[62] M. D. Morse, Experimental methods in the physical sciences **29**, 21 (1996).

[63] U. Even, EPJ Techniques and Instrumentation **2**, 1 (2015).

[64] D. Garg *et al.*, Physical Chemistry Chemical Physics **26**, 20261 (2024).

[65] J. W. L. Lee *et al.*, Nature Communications **12**, 6107 (2021).

[66] J. W. Lee *et al.*, Physical Chemistry Chemical Physics **24**, 23096 (2022).

[67] H. Steen and M. Mann, Nature reviews Molecular cell biology **5**, 699 (2004).

[68] S. Rauschenbach, M. Ternes, L. Harnau, and K. Kern, Annual Review of Analytical Chemistry **9**, 473 (2016).

[69] T. K. Esser *et al.*, Science advances **10**, eadl4628 (2024).

[70] A. V. Zinovev, I. V. Veryovkin, J. F. Moore, and M. J. Pellin, Analytical chemistry **79**, 8232 (2007).

[71] C. Calvert *et al.*, Physical Chemistry Chemical Physics **14**, 6289 (2012).

[72] Z. Huang *et al.*, Analytical chemistry **90**, 3920 (2018).

[73] W.-P. Peng *et al.*, Angew. Chem. Int. Ed (2006).

[74] J.-C. Poully, J. Miles, S. De Camillis, A. Cassimi, and J. B. Greenwood, Physical Chemistry Chemical Physics **17**, 7172 (2015).

[75] O. Ghafur *et al.*, The Journal of chemical physics **149** (2018).

[76] C. Sparling *et al.*, Physical Chemistry Chemical Physics **25**, 6009 (2023).

[77] D. Milešević *et al.*, Review of Scientific Instruments **94** (2023).

[78] D. Milesevic, *Photoinduced Chemistry of Biomolecular Building Blocks and Molecules in Space*, PhD thesis, University of Oxford, 2023.

[79] Kramida, A., Ralchenko, Yu., Reader, J., and NIST ASD Team, Nist atomic spectra database (version 5.11): Helium ionization energies, `https://physics.nist.gov/asd`, 2024, National Institute of Standards and Technology, Gaithersburg, MD. Accessed: 2026-03-26.

[80] E. Lumsdon, *Electron-Induced Fragmentation Mechanisms of Polycyclic Aromatic Hydrocarbons*, PhD thesis, University of Oxford, 2025.

[81] J. L. Wiza *et al.*, Nucl. Instrum. Methods **162**, 587 (1979).

[82] A. Nomerotski *et al.*, Journal of Instrumentation **5**, C07007 (2010).

[83] J. John *et al.*, Journal of Instrumentation **7** (2012).

[84] A. T. Clark *et al.*, The Journal of Physical Chemistry A **116**, 10897 (2012).

[85] B. Y. Chang, R. C. Hoetzlein, J. A. Mueller, J. D. Geiser, and P. L. Houston, Review of Scientific Instruments **69**, 1665 (1998).

[86] C. S. Slater, *Studies of Photoinduced Molecular Dynamics Using a Fast Imaging Sensor*, PhD thesis, University of Oxford, 2013.

[87] N. H. Abel, Journal für die reine und angewandte Mathematik **1826**, 153 (1826).

[88] E. W. Hansen and P.-L. Law, Journal of the Optical Society of America A **2**, 510 (1985).

[89] A. N. Tikhonov, Soviet Mathematics Doklady **4**, 1035 (1963).

[90] V. Dribinski, A. Ossadtchi, V. A. Mandelshtam, and H. Reisler, Review of Scientific Instruments **73**, 2634 (2002).

[91] G. A. Garcia, L. Nahon, and I. Powis, Review of Scientific Instruments **75**, 4989 (2004).

[92] L. Frasinski, K. Codling, and P. Hatherly, Science **246**, 1029 (1989).

[93] T. Arion and U. Hergenhahn, Journal of Electron Spectroscopy and Related Phenomena **200**, 222 (2015).

[94] T. Baer, International Journal of Mass Spectrometry **200**, 443 (2000).

[95] J. Eland, F. Wort, and R. Royds, Journal of electron spectroscopy and related phenomena **41**, 297 (1986).

[96] G. Dujardin, S. Leach, O. Dutuit, P.-M. Guyon, and M. Richard-Viard, Chemical physics **88**, 339 (1984).

[97] C. Vallance, D. Heathcote, and J. W. Lee, The Journal of Physical Chemistry A **125**, 1117 (2021).

[98] H. Köckert, D. Heathcote, J. W. Lee, and C. Vallance, Molecular Physics **119**, e1811909 (2021).

[99] B. Metherall, D. Heathcote, C. P. Please, and C. Vallance, Covariance inversion (in preparation) .

[100] D. Heathcote and C. Vallance, The Journal of Physical Chemistry A **125**, 7092 (2021).

[101] L. J. Frasinski, Journal of Physics B: Atomic, Molecular and Optical Physics **49**, 152004 (2016).

[102] V. Zhaunerchyk *et al.*, Journal of Physics B: Atomic, Molecular and Optical Physics **46**, 164034 (2013).

[103] V. Zhaunerchyk, L. Frasinski, J. H. Eland, and R. Feifel, Physical Review A **89**, 053418 (2014).

[104] P. Downie and I. Powis, Faraday discussions **115**, 103 (2000).

[105] F. Aguirre and S. Pratt, The Journal of chemical physics **118**, 6318 (2003).

[106] A. Misra *et al.*, Materials Letters **34**, 415 (1998).

[107] R. Levy *et al.*, Journal of materials research **13**, 2643 (1998).

[108] K. G. Low, P. D. Hampton, and I. Powis, Chemical physics **100**, 401 (1985).

[109] I. Powis, O. Dutuit, M. Richard-Viard, and P. M. Guyon, The Journal of chemical physics **92**, 1643 (1990).

[110] F. Aguirre and S. Pratt, The Journal of chemical physics **119**, 9476 (2003).

[111] C. Sparling, A. Ruget, N. Kotsina, J. Leach, and D. Townsend, ChemPhysChem **22**, 76 (2021).

[112] F. Jensen, *Introduction to computational chemistry*, 2nd ed. (Wiley, 2007).

[113] K. Andersson, P. A. Malmqvist, B. O. Roos, A. J. Sadlej, and K. Wolinski, Journal of Physical Chemistry **94**, 5483 (1990).

[114] A. I. Krylov, Annu. Rev. Phys. Chem. **59**, 433 (2008).

[115] S. G. Lias, Ionization energy evaluation, in *NIST Chemistry WebBook, NIST Standard Reference Database No. 69*, Gaithersburg MD.

[116] P. Verma, R. Naghma, and B. Antony, Molecular Physics **114**, 1778 (2016).

[117] V. H. Dibeler, R. M. Reese, and F. L. Mohler, Journal of Research of the National Bureau of Standards **57** (1956).

[118] F. Dorman, The Journal of Chemical Physics **41**, 2857 (1964).

[119] R. Bombach *et al.*, Chemical Physics **66**, 403 (1982).

[120] C. Klots, Zeitschrift für Physik D Atoms, Molecules and Clusters **21**, 335 (1991).

[121] J. Laskin and C. Lifshitz, Journal of mass spectrometry **36**, 459 (2001).

[122] T. Cvitaš, H. Güsten, L. Klasinc, I. Novadj, and H. Vančik, Zeitschrift für Naturforschung A **32**, 1528 (1977).

[123] S. S. Kaler, Q. Lou, V. M. Donnelly, and D. J. Economou, Journal of Vacuum Science & Technology A **34** (2016).

[124] N. Cox, V. Mazur, and D. Colbourne, (2008).

[125] A. K. Sum and S. I. Sandler, Molecular Physics **100**, 2433 (2002).

[126] R. C. E. Inventory, JOURNAL OF GEOPHYSICAL RESEARCH **104**, 8333 (1999).

[127] F. Keppler *et al.*, Atmospheric Chemistry and Physics **18**, 6625 (2018).

[128] T. Köhler, A. Gutacker, and E. Mejía, Organic Chemistry Frontiers **7**, 4108 (2020).

[129] X. Tang, G. A. Garcia, and L. Nahon, The Journal of Physical Chemistry A **119**, 5942 (2015).

[130] X. Tang *et al.*, The Journal of Chemical Physics **136** (2012).

[131] J. Eland, R. Frey, A. Kuestler, H. Schulte, and B. Brehm, International Journal of Mass Spectrometry and Ion Physics **22**, 155 (1976).

[132] T. N. Olney *et al.*, Chemical physics **189**, 733 (1994).

[133] T. Masuoka and I. Koyano, The Journal of chemical physics **95**, 1619 (1991).

[134] Y. Wu *et al.*, The Journal of Chemical Physics **163** (2025).

[135] M. Ahmed, D. S. Peterka, P. Regan, X. Liu, and A. G. Suits, Chemical physics letters **339**, 203 (2001).

[136] C. Vallance, S. A. Harris, J. E. Hudson, and P. W. Harland, Journal of Physics. B, Atomic, Molecular and Optical Physics **30** (1997).

[137] K.-M. Weitzel, F. Güthe, J. Mähnert, R. Locht, and H. Baumgärtel, Chemical physics **201**, 287 (1995).

[138] J. Harvey, R. P. Tuckett, and A. Bodi, The Journal of Physical Chemistry A **116**, 9696 (2012).

[139] S. J. Blanksby and G. B. Ellison, Accounts of chemical research **36**, 255 (2003).

[140] R. Locht, J. Momigny, E. Rühl, and H. Baumgartel, Chemical physics **117**, 305 (1987).

[141] M. Tsuji, T. Funatsu, H. Kouno, and Y. Nishimura, The Journal of chemical physics **97**, 8216 (1992).

[142] R. Naghma and B. Antony, Journal of Electron Spectroscopy and Related Phenomena **189**, 17 (2013).

[143] J. Momigny, R. Locht, and G. Caprace, International journal of mass spectrometry and ion processes **71**, 159 (1986).

[144] H.-W. Xi, M.-B. Huang, B.-Z. Chen, and W.-Z. Li, The Journal of Physical Chemistry A **109**, 9149 (2005).

[145] H.-W. Xi, M.-B. Huang, B.-Z. Chen, and W.-Z. Li, The Journal of Physical Chemistry A **109**, 4381 (2005).

[146] J. Eland, R. Frey, A. Kuestler, H. Schulte, and B. Brehm, International Journal of Mass Spectrometry and Ion Physics **22**, 155 (1976).

[147] R. Locht and J. Momigny, International journal of mass spectrometry and ion processes **71**, 141 (1986).

[148] G. Bieri, L. Åsbrink, and W. Von Niessen, Journal of Electron spectroscopy and related Phenomena **23**, 281 (1981).

[149] D. S. Won, M. S. Kim, J. C. Choe, and T.-K. Ha, The Journal of Chemical Physics **115**, 5454 (2001).

[150] L. Karlsson, R. Jadrny, L. Mattsson, F. T. Chau, and K. Siegbahn, Physica Scripta **16**, 225 (1977).

[151] H. Zhang *et al.*, International journal of environmental research and public health **19**, 3944 (2022).

[152] K. Hayakawa, Chemical and Pharmaceutical Bulletin **64**, 83 (2016).

[153] G. Lagache *et al.*, The Astrophysical Journal Supplement Series **154**, 112 (2004).

[154] A. Tielens, EAS Publications Series **46**, 3 (2011).

[155] T. Shaaran *et al.*, Physical Review A **99**, 023421 (2019).

[156] B. Feuerstein *et al.*, Physical review letters **87**, 043003 (2001).

[157] M. E. Wacks, The Journal of Chemical Physics **41**, 1661 (1964).

[158] K. Ledingham *et al.*, The Journal of Physical Chemistry A **103**, 2952 (1999).

[159] J. Bouwman, A. J. de Haas, and J. Oomens, Chemical Communications **52**, 2636 (2016).

[160] S. Banhatti *et al.*, Physical Chemistry Chemical Physics **24**, 27343 (2022).

[161] B. J. West, L. Lesniak, and P. M. Mayer, The Journal of Physical Chemistry A **123**, 3569 (2019).

[162] H. R. Hrodmarsson *et al.*, Space Science Reviews **221**, 42 (2025).

[163] V. Kislov, A. Sadovnikov, and A. Mebel, The Journal of Physical Chemistry A **117**, 4794 (2013).

[164] A. Marciniak *et al.*, Nature Communications **6**, 7909 (2015).

[165] A. Marciniak *et al.*, Nature communications **10**, 337 (2019).

[166] A. Stamatovic and G. Schulz, Review of Scientific Instruments **39**, 1752 (1968).

[167] A. Stamatovic and G. Schulz, Review of Scientific Instruments **41**, 423 (1970).

[168] J. Matúška, D. Kubala, and Š. Matejčík, Measurement Science and Technology **20**, 015901 (2008).

[169] V. Grill, H. Drexel, W. Sailer, M. Lezius, and T. Märk, International Journal of Mass Spectrometry **205**, 209 (2001).

[170] M. Takahashi, Bulletin of the Chemical Society of Japan **82**, 751 (2009).

[171] D. G. Matalon, K. L. Nixon, and D. B. Jones, International Journal of Molecular Sciences **26**, 11729 (2025).

[172] C. Vallance, Physical Chemistry Chemical Physics **13**, 14427 (2011).

Appendices

A

Appendix: Electron ionisation of trifluoroiodomethane at low electron energies

Work was conducted by the group of Prof. Dave Townsend (Heriot-Watt University) to evaluate the error associated with denoising the velocity-map images presented in Chapter 4. Error analysis was conducted for the images of CF_3^+, I_+ and CF_2I^+ at electron energies of 12.3 eV, 14 eV and 16 eV, respectively. These energies are the lowest energies for which sufficient statistics were acquired to denoise the respective images. In order to determine the denoising error as a function of radius for a particular image, the image was first denoised. The reconstructed image was then sampled to generate 50 noisy versions of the image, each of which were then denoised. The plots in Figure A.1 show the mean denoised radial distribution from the fifty denoised images for each ion, with the 2σ error band indicated by the red shaded areas.

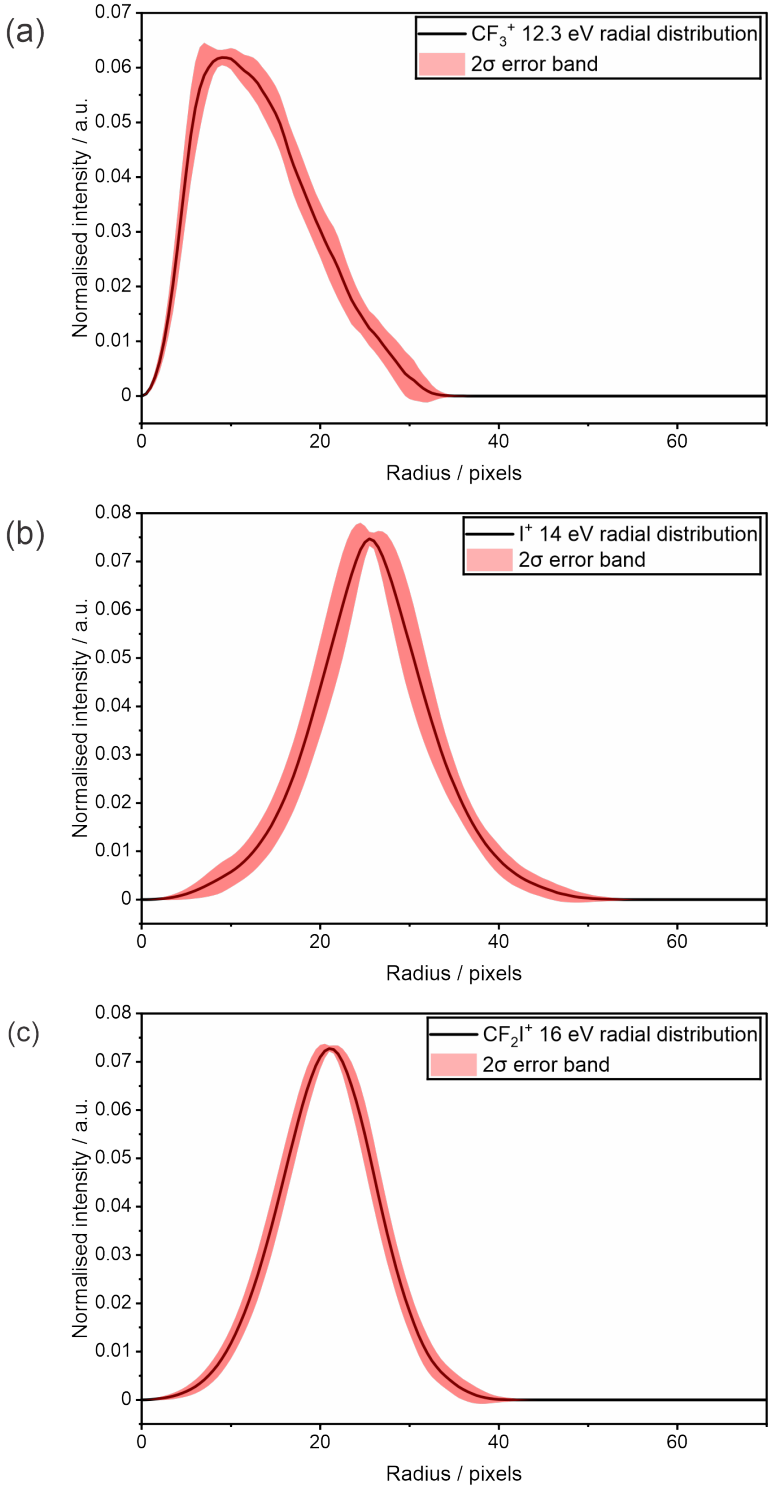


Figure A.1: The mean denoised radial distributions for the (a) CF_3^+, (b) I^+ and (c) CF_2I^+ products at electron energies of 12.3, 14 and 16 eV, respectively. The 2σ error bands have been determined in the manner described in the text.

Electronic state	CASSCF/CASPT2 energy / eV	EOM-IP-CCSD energy / eV	Photoelectron band maxima / eV[122]
D_0 ($^2E_{3/2}$)	10.327	10.801	10.45
D_1 ($^2E_{1/2}$)	10.920	10.801	11.18
D_2 ($^2A_1$)	12.885	13.258	13.25
D_3 ($^2A_2$)	15.919	15.380	15.56
D_4 (^2E)	16.567	16.057	16.32
D_5 (^2E)	16.590	16.059	16.32
D_6 (^2E)	17.243	17.142	17.28

Table A.1: Vertical ionisation energies of the seven lowest electronic states of the CF_3I^+ cation computed at the neutral Franck-Condon geometry. Values in the left-hand column were obtained from CASSCF/CASPT2 (ANO-R2 basis set) using the first point of the PES scans reported in Chapter 4. For comparison, the results from EOM-IP-CCSD results (using an ANO-RCC-VDZP basis set) computed at the optimised neutral ground state geometry are tabulated, alongside photoelectron band maxima reported by Cvitaš and co-workers.[122] The EOM-IP-CCSD method is well-suited for calculating the ionisation potentials of cationic states.[114] However, note that the EOM-IP-CCSD results do not account for spin-orbit splitting. All EOM-IP-CCSD calculations were carried out by James Merrick using the ORCA (v5.0.3) software package.

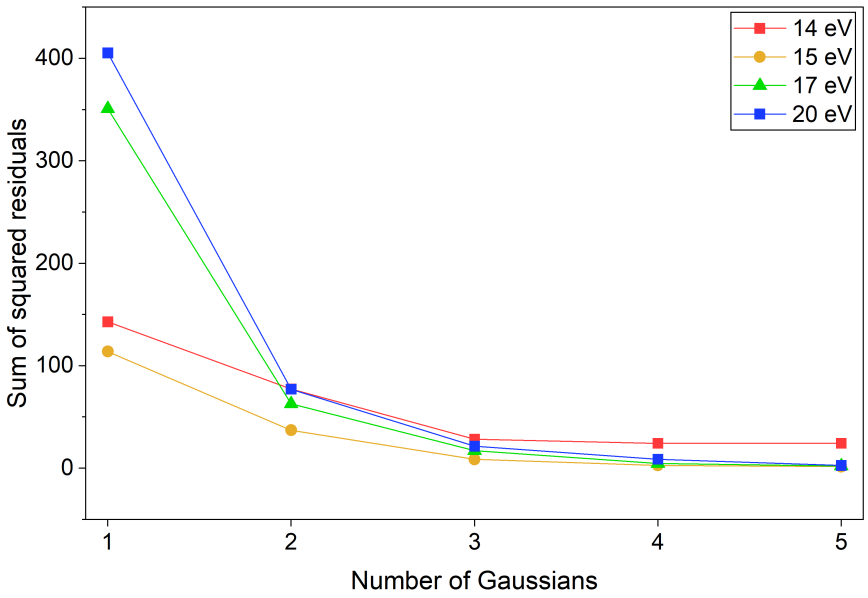


Figure A.2: The sum of squared residuals associated with fitting the I^+ TKER distribution at electron energies of 14, 15, 17 and 20 eV, plotted as a function of the number of Gaussian functions included in the fitting function.

B

Appendix: Electron ionisation of methyl fluoride and methyl chloride at low electron energies

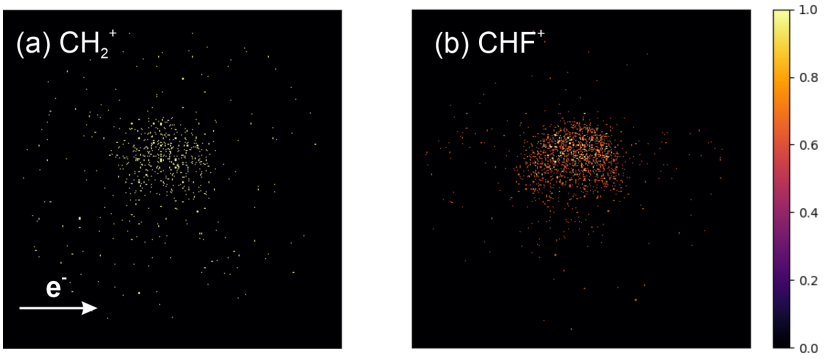


Figure B.1: Spatial map images for (a) CH_2^+ and (b) CHF^+ produced from CH_3F at an electron energy of 20 eV. Both images are centred and circular in form, indicating that the respective ions are formed predominantly at the intersection of the electron and molecular beams. Note that the electron beam propagation direction is from left to right in the images.

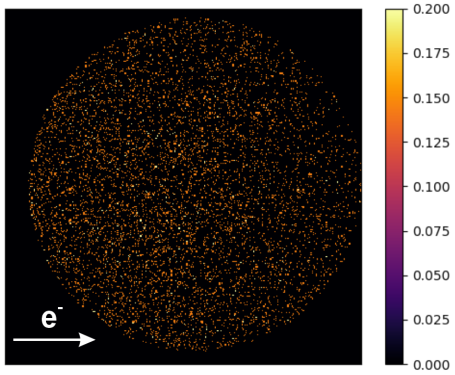


Figure B.2: Spatial map image for H^+ produced from CH_3Cl at an electron energy of 15 eV. Intensity is scattered across the image and is not typical of an ion formed predominantly at the intersection of the electron and molecular beams.